# DETERMINING TEXTURE IN MATERIALS USING LASER ULTRASONIC METHODS

by

Lindsey R. Lindamood

A dissertation submitted to Johns Hopkins University in conformity with the
requirements for the degree of Doctor of Philosophy

Baltimore, Maryland
October 2013

# Abstract

When the microstructure of a material has directional variation in elastic stiffness, such as a transversely isotropic material, ultrasonic waves propagate at different speeds when traveling along different directions through the material. Much of the research using ultrasound to measure the texture of materials relies not only on the polarization of the traveling wave but also on the direction of propagation relative to the preferred orientation of the material. The research in this thesis focuses on changing the polarization direction of the ultrasonic pulse, specifically the shear wave, and maintaining the wave's propagation direction. The key experimental arrangement uses a laser line source to generate longitudinal and shear waves simultaneously in the through-thickness direction of a plate-like sample. The line source enables us to give directionality to the ultrasonic pulse and change the polarization by rotating the line. We show how the texture of the material influences the propagation of the ultrasound. We also have experimental evidence that early fatigue damage can cause shear birefringence. Finding the exact locations of microcracking in fatigued materials with the traditional ultrasonic methods is difficult. Understanding how texture may alter results will help to better identify the microscopic changes that are occurring within these fatigued materials. The experimental results show that changes in wavespeed relative to the rolling direction provide information on preferred orientation and stiffness. This dissertation shows how the derivation of velocities in a single cubic crystal can be used in the orientation distribution function to generate the velocities in a material with cubic crystallites and orthorhombic symmetry. Comparing experimental velocity results to theory allows for the generation of texture coefficients using those velocity measurements.

## Acknowledgements

I have many people to thank for helping me reach this achievement, but first and foremost my advisor Professor Jim Spicer. Your support on this subject and encouragement made the work possible. Although you have taught me a great deal, it is only a small fraction of your expertise on the subject, a level of knowledge which I hope to reach some day. I also want to thank my committee members Professor Cammarata, Professor Ghosh, Professor Graham-Brady and Professor El-Awady for your guidance through the final version of this thesis. In particular, thank you Professor Cammarata for your continued support through courses and departmental hurdles such as the qualifying exam which was vital to my success.

Outside of JHU I would like to thank Professor Peralta at Arizona State University for your help with EBSD analysis and mechanical design consulting. I learned a great deal despite the distance and these things contributed to a significant portion of my work. For EBSD imaging and metallographic technical advice, thanks to Ryan Deacon at the Applied Physics Lab and thanks to Mike Rooney and Andrew Lennon at APL for supporting my efforts on fatigue testing.

I would not have stayed sane without the help of the departmental staff. Special thanks to Walt Krug, Mike Franckowiak and Frank Cook, for keeping a revolving door in the machine shop, cutting samples (especially the dreaded graphite!) and for always having a good story to share; to Mark Koontz, for helping me out with lab equipment and for company while I polished the endless supply of aluminum; and to Jeanine Majewski, Marge Weaver, Paula Davis and Dot Reagle for being mom when I needed her close by.

In the lab I was privileged to rely on undergraduate students Max Borchard, Jon Vandermark, and Karen Han to churn out samples and data, and on lab mates Travis DeJournett and Caroline McEnnis for constant help and friendship. To you and all the wonderful friends I made at my time at Hopkins, especially Laura Darnell, Janice Lin, Felicitee Kertis and Su Kim, we celebrated the great achievements and cried when things went sour, but we all moved on - I am grateful for the experience and am blessed to have you part of my life.

To my dear friends and family back home, thank you for your encouragement and excitement about what I have accomplished especially when it seemed like this day would never come. A special thank you to Julie Mason for the endless editing you provided for me.

I have great appreciation for my husband, MJ, for believing in me and always being by my side giving me the strength to power through the obstacles. And thank you to my sweet little girl Olivia for being the motivation to wrap things up. No matter how discouraged I felt about progress, coming home to you made me forget all about it.

Most importantly thank you to my parents for always supporting my decisions and being there through all the ups and downs of life, because I would not be who or where I am today without you.

For Grandma, I still want to be an astrophysicist when I grow up. Or open a bakery. Whichever comes first.

## Table of Contents

## List of Tables

## List of Figures

# 1 INTRODUCTION AND BACKGROUND

Ultrasonic techniques can be used to measure properties such as attenuation, wavespeed, and changes in the transmitted frequencies affected by microstructural changes that initiate material failure. The subject of this research is motivated by the need to identify damage in aircraft materials and nuclear grade graphite before catastrophic failure. Specifically, we aim to detect fatigue damage prior to microcrack formation by monitoring changes in material elasticity, thus contributing a way to localize material damage for the structural health monitoring community. Ultrasonic characterization of the microstructure allows for rapid, nondestructive assessment of material integrity.

In ultrasonics, we can measure the bulk elastic properties of a material, such as the elastic stiffness tensor matrix components, and monitor changes in these components due to localized plastic deformation in the material from material processing and fatigue damage. Detecting these deformation mechanisms early will give insight to a specimen being prone to failure, even if it is in a location normally unlikely to fail, or failing unexpectedly early due to some pre-existing defect. This is often the case as stated in aircraft failure reports and goes undetected until a large crack is observed propagating through a section of the plane.

Structural health monitoring and prognosis rely on diagnostic systems assessing damage accumulation in a material. Permanent ultrasonic contacting sensors are often used as one of these diagnostic systems and can provide some useful information about the state of the material for an estimation of the structure’s remaining lifetime. This type of system generally does not isolate local damage, but it can alert the user to significant damage accumulation somewhere in the material. Early detection of material damage is critical when monitoring aircraft, bridges, and other infrastructure, and it is often very desirable that the detection be nondestructive, such that the incipient damage can be detected while keeping these structures intact and protected from further damage. The Federal Aviation Administration (DOT 2010) reports on the inability to detect widespread fatigue damage (WFD) and the fortuitous discoveries of WFD in numerous in-commission aircraft often by routine cosmetic maintenance or by mechanics. Some of the cracks discovered prior to flight have been on the order of two feet long, and if these aircraft were to take flight the result could be as severe as the Southwest Airlines' Boeing 737 stripping of the fuselage in 2011. Although quick thinking of the crew saved everyone on board that flight, in some instances these undiscovered material malfunctions have led to the unnecessary loss of life.

Failure of nuclear reactor graphitic cores is also difficult to measure and monitor and can be devastating if significant damage goes undetected. Neutron radiation and thermal cycling affect the grain and pore structure of the graphite as well as induce microcracks and cracks. This indicates that the service environment provided by the reactor can cause material failure. Current proposals and research by the Department of Energy state that graphite has the ability to relax the stresses accumulated after neutron bombardment, avoiding failure and extending the life of the core material. If this problem could be better understood and reactor life extended, then the amount of nuclear waste will be reduced as will the need to develop new graphite for replacement cores (DOE 2010).

To improve the statistics of early crack detection we propose looking at the preferred orientation of a material and monitoring the changes in elastic stiffness while defect/damage accumulates in the material. We will use the orientation distribution function (ODF) to quantitatively describe the materials' state. The orientation distribution function will allow us to find an average of the preferred orientation of individual crystallites in our polycrystalline samples. When the elastic stiffness tensor for a single crystal is known, the orientation distribution coefficients can be calculated. In order to determine the velocities for any given direction in our material we will need to perform a tensor transformation from crystal space to sample space. Finally, using the calculated coefficients and the new stiffness tensor, we can find the velocities. These ultrasonic results can be compared to electron backscatter detection (EBSD) data taken on the same materials. We believe ultrasound will provide useful texture analysis because it will represent the bulk rather than the surface, it is non-destructive, and it does not require stripping layers to give a full representation of overall texture. This introduction will provide a literature review and background information focusing on ultrasonic methods to detect fatigue damage prior to visible crack formation and growth because the aim of the research presented in later chapters is to monitor material behavior in the initial state and early stages of fatigue. We will also discuss properties of anisotropic materials, and how wave propagation is affected by various scattering mechanisms. Finally, the birefringence effect is covered in several material systems (metals, geological materials and graphite) demonstrating the importance of this effect as a potential tool for fatigue damage detection. These systems are all necessary for interpreting our experimental results that will include as-received metals, graphites, and fatigue damaged aluminum.

## 1.1 Monitoring microstructural behavior in the early stages of fatigue damage by ultrasonic techniques

Much of the literature on monitoring fatigue damage using ultrasonic techniques tracks changes in wave attenuation since this has been a standard method for locating larger cracks (Joshi & Green 1972; Kenderian *et al*. 2003; Ogi *et al*. 1997; Tanaka and Izawa 2002). Meanwhile there is a very narrow window for observing properties (such as velocity) as they evolve prior to crack initiation and microcracking. Hikata *et al*. (1962) described glide systems interacting due to increases in dislocation movement and pileup. They show that increases in velocity and attenuation are associated with dislocation loop length in single crystals at the early stages of fatigue. For single crystals, easy glide occurs in the first stage of work hardening where only the primary slip system is activated and as long as a secondary slip system is not activated the wave will not experience changes in velocity or attenuation. In aluminum single crystals, an increase in dislocation loop length leads to an increase in dislocation density. After easy glide, dislocation multiplication in secondary slip systems begins and interacts, cutting into dislocations of other systems. From Figure 1, velocity increases during this easy glide and then decreases later on in deformation because dislocation loop lengths can no longer increase thus interactions with different glide systems cause the loop lengths to shorten while the shear wave detects additional vibrational displacement due to the secondary slip activation and dislocation pileup which therefore cause velocity to decrease (Truell *et al*. 1969). Kenderian *et al*. (2003) have represented the attenuation and velocity of fatigued damaged steel as a function of dislocation density and loop length using the Granato and Lücke theory on dislocation damping (Granato & Lücke 1956a; 1956b).

Attenuation:

$$\alpha = K_1 \Lambda L^4 \tag{1}$$

Normalized velocity:

$$\delta V = \frac{V_0 - V}{V_0} = K_2 \Lambda L^2 \tag{2}$$

Dislocation loop length:

$$L = K_3 \left( \frac{\alpha}{\delta V} \right)^{1/2} \tag{3}$$

Dislocation density:

$$\Lambda = K_4 \left( \frac{\delta V^2}{\alpha} \right) \tag{4}$$

*K* values represent material constants associated with frequency, $\alpha$ is attenuation, $\Lambda$ is dislocation density, *L* is dislocation loop length, $V_o$ is initial condition velocity and *V* is velocity after some number of fatigue cycles.

In the experiments performed by Kenderian *et al.*, notched specimens for cyclic fatigue were made from rail steel with one 5 MHz shear wave piezoelectric transducer, for pulse-echo measurements, mounted in the notched region. Attenuation and velocity were recorded after interrupting the fatigue testing at designated cycle increments. Based on the theory to describe what may be the evolution of dislocations in steel, rapid changes in attenuation or velocity were not observed after initial fatigue, which would be during the time when microcracks form. Their experimental technique was not sensitive enough to detect scattering from parallel microcracks (relative to the direction of ultrasonic propagation). Even if the experiment had been sensitive enough to detect this scattering, microcracks formed after initial fatigue never permeated into the detection region of the transducer. Min *et al*. (2005) also use Granato and Lücke theory to find dislocation density and related parameters. Min *et al*. ran ex-situ and in-situ experiments using a transducer mounted to aluminum 2024 while undergoing fatigue. This alloy was the T3 temper and therefore already contained a high dislocation density from cold rolling, unlike Kenderian *et al.* who uses material with a lower dislocation density. They observed a gradual increase in velocity as fatigue increased as well as determined dislocation density to decrease at initial fatigue and then gradually increase while cyclic fatigue continued. Unlike previous authors, dislocation density was also measured using x-ray diffraction analysis in addition to the theoretical calculation and their experimental results support previous results from Hikata *et al.* (1965) and Truell (1969). On the contrary, analysis on a small sample set presented by Mujica *et al*. (2012) show only longitudinal velocity increasing with dislocation density, while shear velocity decreases.

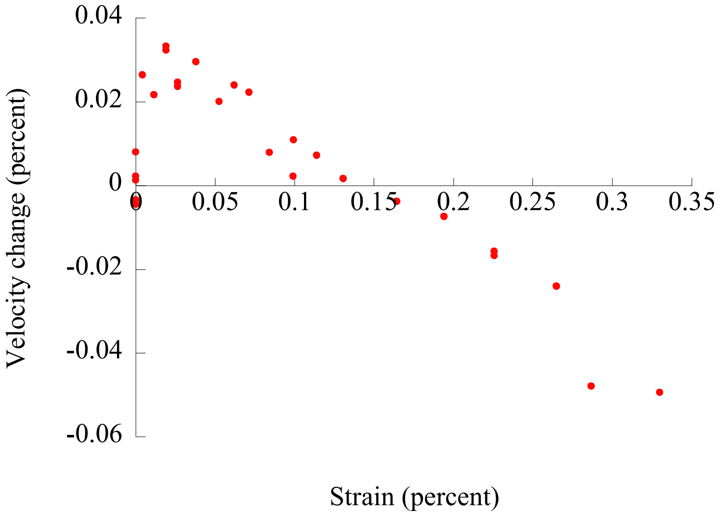

**Figure 1**: Data recreated from Hikata *et al.* (1965) showing a change in velocity as an aluminum single crystal undergoes compression

Nonlinear ultrasonic methods have also been developed as a way to monitor fatigue damage (Cantrell & Yost 2001; Pruell *et al*. 2009; Hikata *et al*. 1965; Oruganti *et al*. 2007). Pruell *et al.* describe theory and experiments using guided Lamb waves to detect plastic deformation by measuring the amplitudes of the fundamental and second harmonic frequencies. They used narrow-banded contacting transducers, each mounted with lubricating oil to a Plexiglas wedge, to send and receive ultrasound through thin aluminum plates. Identifying wave characteristics in the time domain with this technique is difficult, so by looking at the Fourier domain, they measured the second harmonics generated by the single frequency waves. These harmonics are generated from the distortion of the input wave caused by dislocation movements that form an asymmetric dipole. The acoustic nonlinearity parameter is calculated from the amplitudes, $A_2/A_1^2$, and increases linearly with fatigue damage. An increase in the nonlinearity parameter is associated with the growth of persistent slip bands and, according to Cantrell *et al.*, dominated by dislocation dipoles rather than intrinsic nonlinear elasticity effects. This technique, while efficient in monitoring material overall, cannot locally identify where fatigue is occurring. If the specimen is small enough, the Lamb wave measurement can provide greater spatial resolution, but longitudinal, shear and Rayleigh waves are much more sensitive to localized regions of plastic deformation and microstructural changes regardless of the size of the specimen.

Using longitudinal transducers, Nagy (1998) demonstrated an increase in nonlinearity in polymers and metals when subjected to cyclic fatigue damage. Monitoring early fatigue damage using linear and nonlinear ultrasonic parameters, he showed that nonlinearity increased continuously, and more than doubled in value, from the initial onset of fatigue damage, but linear parameters such as velocity and attenuation decreased and increased respectively by only fractions to a couple percent from initial values. These results demonstrate that nonlinearity is sensitive early on to aligned, random, microcracking, and then level off when these microcracks merge and linear behavior dominates.

For polycrystals, specifically aluminum 2024-T3, an initial increase in velocity of the shear waves due to fatigue has been shown experimentally by Yamagishi *et al*. (2009) using contacting transducers; shear polarized vertically (SV) and horizontally (SH). These were used to measure the viscoelastic and acoustoelastic effects respectively, and have detected the dislocation mobility associated with the progression of fatigue damage leading to changes in velocity, and its dependence on dislocation pileup. Measuring these waves independently of one-another, Yamagishi *et al*. observe an increase in SV velocity just prior to failure and, in terms of time-of-flight, observe a decrease initially in time-of-flight followed by a gradual decrease until failure. This result corresponds to an increase in velocity as fatigue progresses. For both the SV and SH waves, the group shows that there is a considerable change in the rate of velocity increase around 50% lifetime and evidence that residual stress from the initial material state after cold working is released by fatigue.

Based on these studies, it can be interpreted that measuring an increase in velocity might indicate that there is an increase in dislocation density while measuring a decrease in velocity could indicate a high concentration of microcracks. Although both of these effects could be present during fatigue, this conclusion can be used to guide the interpretation of the results presented later in this thesis.

## 1.2 Derivation of the elastic wave equation for anisotropic materials

To show how ultrasound is affected by fatigue damage and how ultrasonics can determine the state of a material we must start with background on texture and wave propagation. For face centered cubic materials, there are four slip planes in the {111} family and each plane has three <110> possible slip directions. We will begin by setting the [100] direction of sample to be in the rolling direction. As the material is pulled in tension, or rolled, the crystallite's (111) slip plane rotates around the [100] axis of the sample to align itself in the [112] direction, midway between the two slip directions, with equal probability of slipping on the (111) or its conjugate. The critical resolved shear stress occurs when the slip direction $S_D$ reaches a critical value, which is some given angle $\lambda$ from the direction of tension, P. In the diagrams in Figure 2 below, as the slip direction and angle $\lambda$ align with angle $\chi$, the direction of tension P will move to the P' location (Clarebrough 1959; Hertzberg 1996).

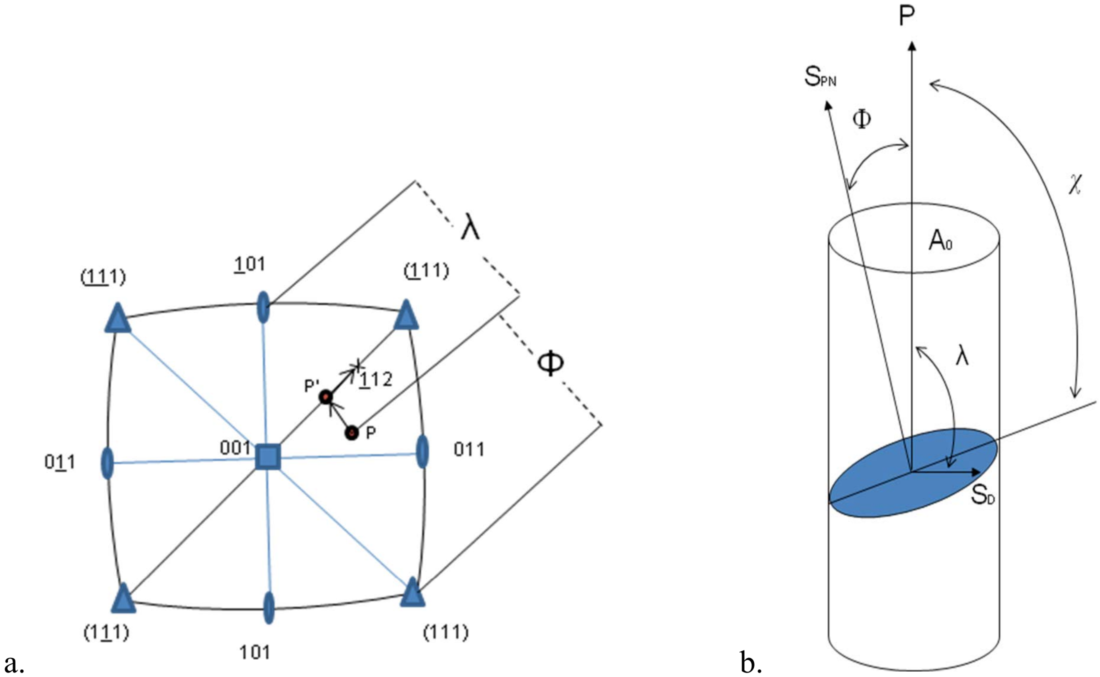

**Figure 2**: Face-centered cubic crystal slip planes and movement during loading, diagrams after Clarebrough (1959) and Hertzberg (1996).

If all crystallite orientations are equally probable, then the material is considered macroscopically isotropic and no preferred orientation exists. The orientation distribution function will allow us to find an average of the preferred orientation of individual crystallites in our polycrystalline samples. When the elastic stiffness tensor for a single crystal is known, the orientation distribution coefficients can be calculated. In order to determine the velocities for any given direction in our material we will need to perform a tensor transformation from crystal space to sample space (Appendix A). Finally, using the calculated coefficients and the new stiffness tensor, we can find the velocities (Bunge 1982; Roe 1965; Sayers 1982).

### 1.2.1 Wave propagation in a single crystal

The main material properties that will cause a change in velocity are scattering by defects and dislocation damping. For a perfect linearly elastic solid there will be no damping or losses and the stress and strain are always in phase. Nonlinearity arises when waves in the material interact and exchange or transfer energy. Lattice defects and dislocations are going to directly affect the crystalline lattice and have an impact on the stress wave propagation (Truell 1969). We assume the effects of nonlinearity to be small so that equations for linear elastic solids can still be used and dispersion to be negligible. Nonlinearity will be due to stress waves interacting with one another, interactions with dislocations and microcracks; all of these causing attenuation of waves. We will use the second order elastic constant terms although third order or higher coefficients ($c_{ijklmn}$) would represent physical nonlinear effects in the crystal lattice.

For a single crystal, (Musgrave 1970) the linear form of Hooke's law is

$$\sigma_{ij} = c_{ijkl} e_{kl} \tag{5}$$

where $\sigma$ is stress, $c$ is stiffness, $e$ is strain and related to displacement $u$ by equation (6):

$$e_{kl} = u_{k,l} \tag{6}$$

so that,

$$\sigma_{ij} = c_{ijkl} u_{k,l} \quad . \tag{7}$$

Taking $\partial x_j$ on both sides,

$$\sigma_{ij,j} = c_{ijkl} u_{k,lj} \tag{8}$$

and now with the equation of motion where $\rho$ is density,

$$\sigma_{ij,j} = \rho \ddot{u}_i \tag{9}$$

gives the wave equation,

$$\rho \ddot{u}_i = c_{ijkl} u_{i,kj} . \tag{10}$$

Using equation (10) with the solution to the wave equation (11)

$$u_k = p_k e^{i(\omega t - k_r x_r)} \tag{11}$$

yields the dispersion relationship

$$\rho p_i \omega^2 = c_{ijkl} p_l k_j k_k . \tag{12}$$

where $u$ is displacement, $p$ is unit polarization vector, ω is angular frequency, $c_{ijkl}$ is the elastic stiffness tensor, $x$ is position, $t$ is time and $k$ are propagation directions. For vector $k$, substituting $k_r = (\omega/V)n_r$ into equation (12) gives us an equation for velocity

$$\rho p_i V^2 = c_{ijkl} p_l n_j n_k \qquad (13)$$

where $V$ is velocity, $p$ is unit polarization vector, and $n$ are propagation directions. Owing to symmetry, some of these terms will be eliminated and the dispersion relation can be used to calculate velocities for different propagation and polarization directions.

### 1.2.2 Dispersion considerations for thick plates and high frequencies

The velocity of a phase or a wave train with periodic spacing which propagates infinitely in time is known as the phase velocity $\upsilon_\varphi$. From the phase in equation (11) we can write an equation for how fast the phase moves,

$$\frac{d(\omega t - kx)}{dt} = 0 \qquad (14)$$

From equation (14) phase velocity can be written with respect to angular frequency,

$$\upsilon_\varphi = \frac{dx}{dt} = \frac{\omega}{k} \qquad (15)$$

Group velocity, $\upsilon_g$, is the velocity of multiple waves traveling together with different frequencies and wave numbers where the velocity can be measured by the peak of the wave packet, or the peak of the periodic group that has resulted from the constructive and destructive interference of the waves. Amplitude will be the same for each wave but superimposing the waves will cause amplitude to increase for the group as long as constructive interference can occur. In this work we assume that Hooke's law still applies with small stresses and strains meaning $\omega/k$ will be linear because for a linear (elastic) and non-dispersive system phase velocity equals group velocity. For a composite material, this would not apply and equation (12) would be modified and complex variables would be included (Stratton 1941; Roux 1990; Main 1993). However, for small changes in displacement and time, or very long wavelengths such that wave vector $k$ is small, phase velocity is approximately equal to group velocity.

In order for the wave group to be constructively superimposed, the waves must all have the same phase angle, $\omega t\text{-}kx$ where $\omega$ and $k$ can be independent but the maximum value for the group will always be in the same position and time. Now for at least two propagating harmonic waves with equal amplitude but slightly different frequencies,

$$\left[\frac{d}{d\omega}(\omega t - kx)\right] = constant \tag{16}$$

$$t - \left(\frac{dk}{d\omega}\right) x = constant \tag{17}$$

and taking the derivative of both sides yields,

$$\upsilon_g \equiv \frac{dx}{dt} = \frac{d\omega}{dk} \tag{18}$$

As mentioned before, for a purely elastic medium (Figure 3), phase velocity equals group velocity when $\omega/k = \partial\omega/\partial k$ which is true for $\upsilon_\varphi = \omega/k = constant$. The group will travel at the same speed as all individual components. We consider the dispersion to be minimal such that there is a linear relationship between $\omega$ and $k$, we can assume phase velocity to be a good approximation of the group velocity used in the calculations throughout this thesis.

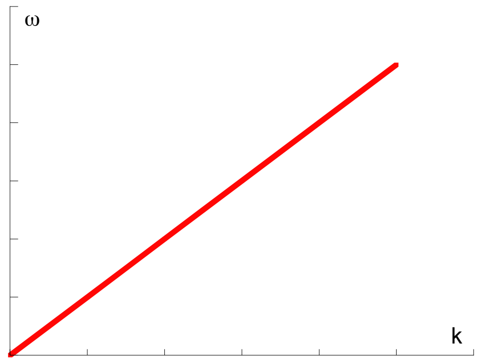

**Figure 3**: Linear dispersion for elastic medium, phase and group velocity are equal

## 1.3 Production of anisotropy in materials

For the experimental work in this thesis, the sources of material anisotropy will be preferred grain orientation due to material processes such as rolling or extrusion and fatigue damage-related structures including induced orientation and microcracking. This background discussion will introduce the preferred orientation of grains and mechanisms behind microcracking. Wave propagation and its dependence on the integrity of a material will lead into background on various crack-induced birefringence effects in metals, rocks and graphite.

Aligned microcracking can occur when the opening and closing of microcracks depends on the compression mechanism and whether uniform pressure is applied. Randomly oriented cracks will experience uneven areas of closure during compression depending on their orientation to the axis of compression. Cracks running perpendicular to the axis of compression will close and those running parallel will become wider. The dependence of open crack distribution on the axis of compression will have an anisotropic effect on the stiffness, making this property directionally dependent on the axis of compression (Sayers 1988, Mauge & Kachanov 1994).

Fatigue damage occurs when a material undergoes cyclic strain fluctuations at a load that allows that type of material to sustain damage. As a material deforms plastically by fatigue or by processing techniques such as cold rolling, dislocations with Burgers vectors of the same sign will repel one another, pile up against a barrier on the slip plane such as a grain boundary, and cause a large stress concentration to develop at the leading edge of the pileup (Hertzberg 1996:83). With a sufficient number of dislocations, plastic deformation can easily occur along these slip directions. For a single crystal loaded in tension, slip will occur on a primary slip system and in polycrystalline materials multiple slip systems will be activated. Having too few dislocations will not allow any freedom of movement for the slip planes, and too many dislocations will interfere with one another and hinder any movement by the slip planes (Clarebrough 1959).

### 1.4 Effects of material properties on wave propagation

Ultrasound interacts with the microstructure of a material and can be a powerful yet nondestructive method to monitor changes in material mechanical properties. Ultrasonic waves can be transmitted using a variety of techniques including contacting transducers, electromagnetic acoustic transducers, and lasers. Cold rolling of the material and fatigue damage will both have an impact on the microstructure of the material, and related effects on the propagating wave will differ depending on the amount of change induced in the microstructure. Potential scatterers of the propagating wave include grains, slip planes, dislocation pileups, and microcracks. Depending on the size of the scatterer, and the wavelength and frequency content of the transmitted wave, the wave that is detected after passing through the material could have significant changes in frequency, velocity, or attenuation after multiple reflections (Gross & Zhang 1992).

Grain scattering is a large contributor to disruptions in wave propagation owing to the size of the grains relative to the ultrasonic wavelength. Indeed, a broader range of frequencies is capable of interacting with grains than with smaller material defects. Scruby *et al*. (1986) measured attenuation and scattering in steel alloys by the forward scattering laser ultrasonic method, monitoring pulse shape, amplitude and the frequency content of the transmitted wave. They found that materials with the larger grains have greater signal levels with additional oscillations corresponding to stronger grain scattering. In contrast, a material with a smaller grain size (on a length scale smaller than that of the transmitted wavelength) scatters less and therefore grain contributions to the data have decreased amplitudes, improving the signal-to-noise ratio.

From micrographs taken of aluminum alloy 2024 shown in Figure 4, it is obvious that microcrack initiation occurs at second phase particles. Voids commonly form at these particle interfaces and the surrounding material matrix, and will ultimately (Figure 5) be a prime source of crack initiation (Rao & Ritchie 1992; Sharma *et al*. 2009; Wang 2006; Zimmermann 2012).

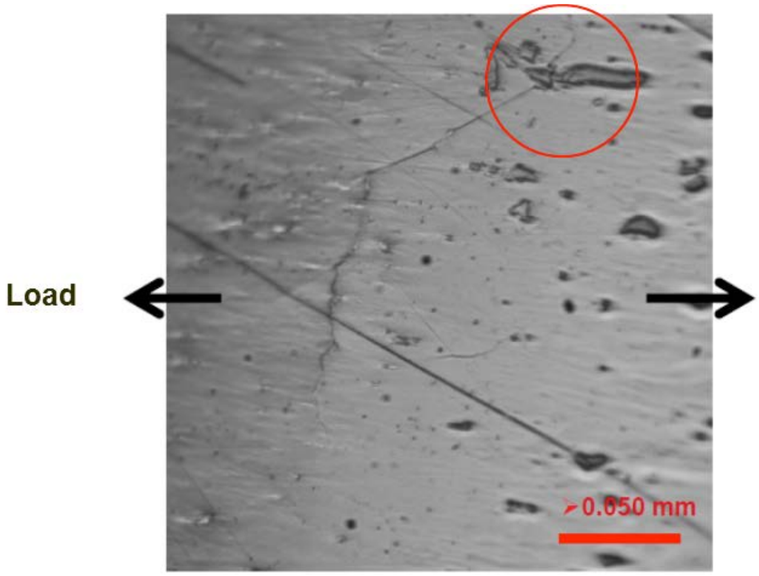

**Figure 4**: Aluminum 2024 micrograph showing second phase crack nucleation produced by Peralta research group at ASU

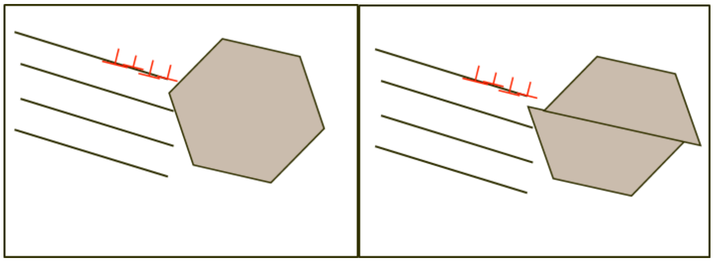

**Figure 5**: Origins of fatigue damage in aluminum alloys. Dispersion of second phase particles readily cut by dislocations yields planar slip and large dislocation pileups. This leads to high stresses, easy initiation of microcracks and brittle behavior.

On the smaller end of the scattering size spectrum, dislocation systems have an impact on higher frequency waves. Maurel *et al*. (2009) have rigorously outlined, expanded the Granato and Lücke theory, to include two- and three-dimensional treatments of elastic waves interacting with dislocations either as single or multiple dislocation systems. Using their development, data might be interpreted such that changes in wavespeed are isolated to interactions with dislocations. They compare the current theory to prior authors' experimental work measuring attenuation, velocity or frequency and plan on conducting experiments isolating specific dislocation situations for verification of the outlined theory of those parameters that show variation with dislocation interaction. For example, in the case of scattering by a single dislocation, either with an elastic wave propagating in two dimensions and interacting with a dislocation having an in-plane Burgers vector, or an elastic wave propagating in three dimensions with a pinned dislocation segment in infinite space, longitudinal and transverse waves interacting with dislocations can each be partially scattered into longitudinal and transverse waves with a preference for both types to be scattered as transverse waves. Maurel *et al.* show this yields four scattering amplitudes and gives expressions for each, which considers the angle of incident wave and the Burgers vector for the dislocation. For the three-dimensional case they show all four scattering amplitudes scale to the ratio of dislocation length to wavelength.

$$f \sim L(L/\lambda)^2 \tag{19}$$

where $f$ is scattering amplitude, $L$ is dislocation length and $\lambda$ is wavelength. For multiple dislocation systems in two dimensions, they show effective phase velocity for anti-plane case (scalar problem, one polarization) and in-plane case (vector problem, two polarizations) increases when dislocations exist, however group velocity will decrease. Finally, in a three-dimensional system with multiple dislocations, equations for attenuation for longitudinal and transverse waves are developed. The ratio of these attenuations from theory is compared to those from experimental results using resonant ultrasound spectroscopy and electromagnetic acoustic resonance on single and polycrystalline copper and $LiNbO_3$.  Maurel *et al*. also believe that their theory can be applied to low angle grain boundaries which can essentially act as arrays of dislocations.

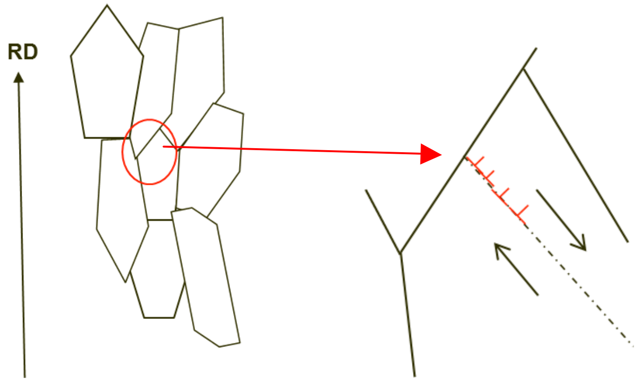

**Figure 6**: Dislocation pileups along a barrier

Dislocation pileups creating a locally high stress field lead to microcracks, another scattering mechanism commonly found in fatigue-damaged materials (Figure 6). Our first look into the fatigue damage problem is driven by the identification of these microcracks, which are a clear indicator fatigue damage has occurred.  Not only do these microcracks and cracks contribute to anisotropic material properties, they also affect wave propagation. Cracks initiated by fatigue damage will still allow ultrasound to propagate because they are not entirely open and portions of the crack faces will touch. This type of crack has been modeled extensively to determine the best method of interpretation (Achenbach *et al*. 1989; Zhang & Achenbach 1988).

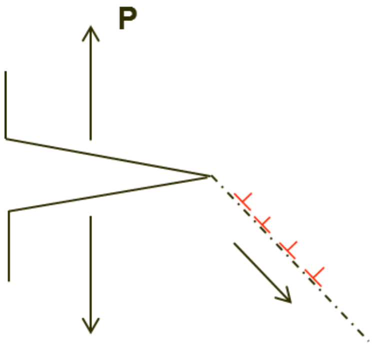

**Figure 7**: Stress concentration from dislocation pileup at a microcrack tip

Interactions with the crack tip will have an impact as well on wave propagation, attenuation, frequency and velocity (Figure 7). Ravenscroft *et al*. (1991) theory with experiment showed dependency of transmission and mode conversion of ultrasonic waves on open or closed artificial cracks as well as the angle around the crack tip that ultrasound was transmitted. Open cracks show a minimum ultrasonic amplitude but the angle expected for that minimum varied between cracks, whereas closed cracks showed no change in amplitude regardless of the angle for ultrasonic transmission. This indicates how simple, through transmission ultrasound needs to be modified in order to capture changes in fatigue damaged materials.

In addition to their existence disrupting material behavior and wave propagation, crack orientation, whether aligned or perfectly random, can impact the elastic stiffness which will affect results of fatigue and ultrasonic testing (Kushch *et al*. 2009). The next section will discuss more in depth on how cracking can have a major impact on velocity in a variety of materials.

## 1.5 Acoustic Birefringence and measuring texture with ultrasound

Acoustic birefringence refers to the difference in velocities of polarized waves propagating through an anisotropic material. This phenomenon is most often recorded from shear wave interactions with the material because an ultrasonic shear wave can be represented by orthogonally polarized waves. Normally these waves are recorded as one shear arrival and not often separated unless the material is anisotropic. Even weakly anisotropic materials, however, can cause one of these polarized shear waves to dominate depending on the preferred orientation of the material. If this preferred orientation changes due to material processing, fatigue or other deformation mechanisms, the dominating shear polarization can change, displaying a new shear velocity despite bulk material geometry or composition not having been altered. In extreme cases of material anisotropy and therefore acoustic birefringence, both shear wave arrivals can be recorded. Differences in longitudinal wave velocity have also been termed birefringence if the wave is oriented to propagate along different axes of symmetry through a sample so that velocity is dependent on microstructure orientation (Dutton & Dewhurst 2007).

When a wave propagates perpendicular to aligned open microcracks, the velocity of the wave decreases (Zadler & Scales 2008; Sayers & Kachanov 1995). The uneven areas of closure experienced during fatigue will distort the velocity of the traveling wave. The dependence of open microcrack orientation on the axis of compression allows two orthogonally polarized shear waves to propagate at different velocities, and this difference in velocity gives us shear wave birefringence. (Sayers 1988) Shear wave birefringence can also be seen with anisotropy due to rolling texture in a processed material.

To quantitatively describe the birefringence and preferred crystallographic orientation of a material, a set of coefficients can be derived from the elastic stiffness calculated by the ultrasonic wave velocities (Appendix A). These coefficients are termed the orientation distribution coefficients (ODCs) and are important values for industry in the formability of materials especially during cold rolling processes. Ultrasonics has an advantage over other methods in that it measures the bulk of the material to determine the ODCs rather than the surface of the material in the case of other characterization methods. These other methods for calculating the ODCs have included X-ray diffraction, neutron diffraction and electron backscatter diffraction (EBSD). We can compare our ultrasonic methods and results to these other techniques but our focus will be on developing the ultrasonic determination of these coefficients further than is currently described in the literature.

### 1.5.1 Birefringence in metals and alloys

Previous work by Thompson *et al.* (1989) and Kawashima (1990), follow the development by Roe (1965) for describing the probability of finding specific orientations of each crystallite in a sample using the orientation distribution function (ODF) which contains the orientation distribution coefficients. Both Thompson *et al.* and Kawashima used electromagnetic acoustic transducers (EMATs) and considered only angles of 0, 45, and 90 degrees from the rolling direction in order to obtain three independent orientation distribution coefficients $W_{400}$, $W_{420}$, and $W_{440}$. Only these three ODCs exist because of the symmetries (orthogonal properties such as mirror planes) in the Legendre functions used to represent the orientation distribution function (Roe 1965). These coefficients take into account waves propagating in the through thickness direction of the sample, as well as the shear waves propagating in the rolling direction and transverse to the rolling direction. For the importance of deep drawing used in making for example aluminum cans, $W_{400}$ gives the resistance of deep drawing, while $W_{420}$ and $W_{440}$ give the likelihood of 2- or 4-fold symmetry present, respectively (Sayers 1982; Anderson *et al*. 1996). Kawashima used EMATs to send and receive ultrasonic waves through the thickness of steel, and used the ultrasonic velocity measurements and the single crystal elastic stiffness components to calculate the ODCs in the rolled steel sheets. Creating pole figures with the ultrasonic results, Kawashima compared these to pole figures derived from X-ray diffraction and found that there was much less information contained in the ultrasonic results compared to those generated using X-ray diffraction. However, because X-rays do not completely indicate bulk texture, he concluded that there was still a significant amount of comparable information in the ultrasonic result, given the test was fast, and does not require special or significant sample preparation. The ODCs extracted proved to be reliable when used for other material constant calculations.

Thompson *et al*. (1989) used a similar method with EMATs calculating the ODCs for thin, pure copper and commercially pure aluminum alloy 1100 sheets. Their goal was to verify the accuracy of previous ultrasonic calculations of the ODCs and compare them with the values determined by X-ray diffraction. They noted that the aluminum did have significant second phase content in the bulk, but that the surfaces for X-ray diffraction of both materials satisfactorily represented the bulk. Aluminum proved to be a particularly difficult case for Thompson *et al.* to identify all the contributing errors in the final calculation of the ODCs. They added that residual secondary phases could be a significant factor in the accuracy of the ODC calculation. Because of aluminum's small elastic anisotropy, error is greater than in those materials such as copper and steel which have a much higher elastic anisotropy. It can be interpreted from their experimental results that aluminum alloys may have similar or more significant errors due to the secondary phases.

The laser ultrasonic resonance (LUR) technique was used to measure texture in steel sheets in the work done by Moreau *et al*. (2002). The LUR technique uses a pulsed ultraviolet laser for generation of the ultrasound, and a Fabry-Perot interferometer for detection. Using Fourier techniques, the resonance frequency is measured after collecting several pulse echoes. The resonance frequencies are then associated with the longitudinal and shear modes. This information allowed Moreau *et al*. to make an accurate calculation of sheet thickness and texture coefficients. A prototype of their technique was implemented on an inspection line to measure the crystallographic texture and the average plastic strain ratio.

Dixon *et al*. (2008) described shear wave birefringence measurements using radially and linearly polarized EMATs that allowed them to obtain the $W_{400}$ and $W_{420}$ orientation distribution coefficients. The birefringence effect (where the polarization of transverse waves affects wavespeed) was measured using through-thickness ultrasonic resonance methods that yield a double peak in the frequency spectrum. They explained the differences in the velocities in the rolling and transverse directions in a material by the interference between frequencies. Limitations in the bandwidth of the EMATs only allowed them to observe the first harmonic in very thin, 0.2 mm, sheets. However, using 1 mm thick sheets, they were able to observe three additional peak maxima in their

Fourier transforms. The group concluded that these through thickness shear wave measurements are not reliable and the curve fitting model used showed that there are discrepancies in calculating the ODCs depending on the maximum frequency chosen for the best fit.

There are many other examples of shear wave birefringence recorded using various ultrasonic techniques. Papadakis (1971) measured shear wave velocities in metal alloy strips propagating at 15° interval angles relative to the rolling direction of the material. He determined texture information using the maxima and minima velocities at 0, 45, and 90 degrees between propagation and rolling directions (rolled plates have orthorhombic symmetry while extruded bars and wires are transversely isotropic). The results revealed similarities to the Tam and Leung (1984) aluminum results such as maximum velocities at 45° in titanium 6Al-4V and Fe-Ni alloy while the steel results were more intuitive with a velocity minimum at 45°. Alers (1966) described texture without using pole figures by measuring the Young's modulus of various materials as a function of angle relative to the rolling direction. For highly isotropic materials like aluminum and tungsten this method could still be applicable by the comparison with measured and calculated values of Young's modulus, looking for any variation between those values. Using the longitudinal wave, Tam and Leung (1984) studied anisotropy in extruded aluminum 6061-T6 bars with laser generated ultrasound and a contacting transducer as a receiver positioned directly opposite the laser so that wave propagation was dependent on the angle relative to the extruded direction. It is expected that velocity be the fastest when propagation is along the extruded direction, 0°, and slowest for propagation at 90° from extrusion. They found this aluminum alloy to have a maximum velocity when the wave propagates 45° from the extruded direction and a minimum when the wave propagated in the 0° extrusion direction. Foster *et al*. (1999) used ultrasound to compare texture in copper and copper alloys containing zinc with neutron diffraction measurements of the orientation distribution coefficients. Their results did not reveal significant anisotropic behavior in pure copper, but with the addition of zinc the material became highly anisotropic and easily characterized using ultrasound. By generating Rayleigh and bulk waves through several aluminum alloys, Wormley *et al*. (2002) found small changes in velocity between polarizations and calculated the stress required to cause the initial anisotropy in the materials. Their results show a strong indication that texture is the main cause of initial anisotropy (prior to loading) because the large statistical uncertainty produced exceeds the changes in the calculated acoustoelastic constants, contained in $A(\theta)$ the anisotropy factor (Tam & Leung 1984):

$$\frac{V(\theta)-V(0)}{V(0)}=A(\theta) \tag{20}$$

where $V(\theta)$ is the velocity at some polarization angle relative to the rolling direction and V(0) is velocity at the rolling direction.

### 1.5.2 Birefringence in geologic materials

Shear wave birefringence has been studied for decades by geologists (Crampin 1981; 2005; 2008) who most recently observed birefringence changes to detect areas most likely to suffer from moderate earthquakes. Geologists see shear splitting in rocks, and measure changes in velocity prior to registered earthquakes. When they observe a loss in shear strength of these cracks, they determine a fracture criticality and can give a narrower window for an impending earthquake (Crampin & Peacock 2005; Crampin *et al*. 2008). In Figure 8, birefringence is described pictorially. As a wave is incident on a surface, strong alignment of microcracks will cause the shear wave's orthogonal polarization to take on independent velocities that are dependent on the directional stiffnesses of the microcracks.

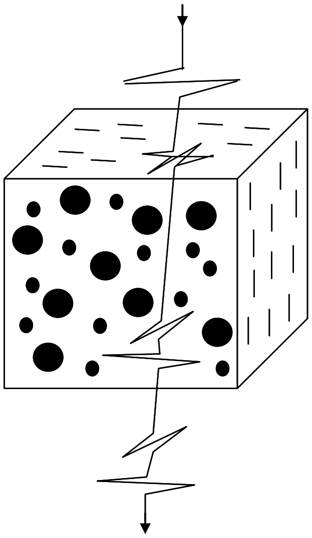

**Figure 8**: Shear wave propagation through an aligned, cracked medium, diagram after Crampin *et al*. 2008.

It has been modeled using elastic constants and experimentally shown that, for rocks undergoing compression, open microcracks aligned perpendicular to the axis of compression will close, increasing velocity along the compression axis, while new microcracks parallel to the axis of compression will open, causing velocity perpendicular to the axis of compression to decrease. In rocks undergoing stress, microcracks are aligned so that ultrasonic waves are affected by this anisotropy. Due to the opening of new cracks, measuring velocities that are perpendicular to the axis of compression will show larger changes in velocity than measuring along the axis of compression where cracks have closed (Stanchits *et al*. 2003; Sayers & Kachanov 1995; Zheng 2000). These changes in wave velocities give an indication of the damage occurring in the rock and the apparent recovery.

For random crack orientations, overall isotropy of effective stiffness is unchanged. When penny shaped cracks are aligned (Figure 9), there is a transversely isotropic orientation distribution of the cracks. This anisotropy is represented by elastic tensors that are dependent on crack density (Sayers & Kachanov 1995).

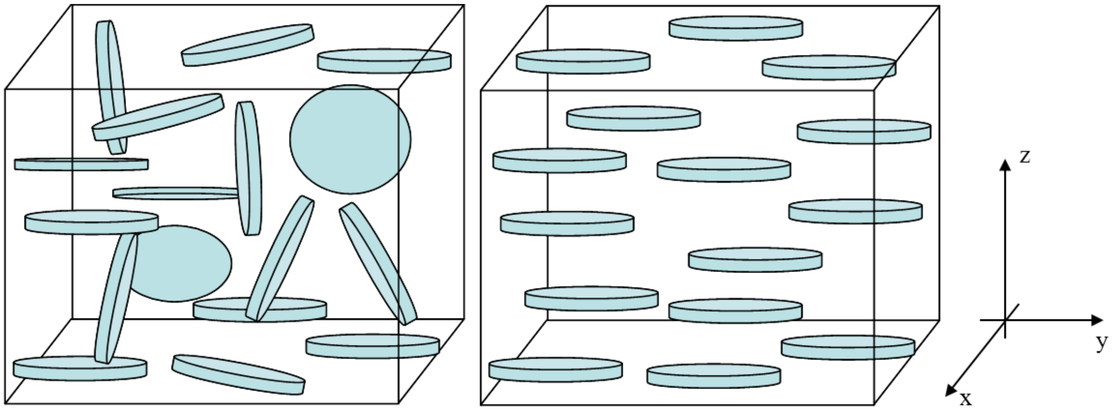

**Figure 9**: Randomly oriented and aligned penny shaped cracks

For a transversely isotropic medium, the following stiffnesses can be determined using longitudinal and shear wave velocities,

$$c_{11} = \rho\upsilon_{11}^{2} \tag{21}$$

$$c_{33} = \rho\upsilon_{33}^{2} \tag{22}$$

$$c_{55} = \rho\upsilon_{13}^{2} \tag{23}$$

$$c_{66} = \rho\upsilon_{12}^{2} \tag{24}$$

where the non-zero stiffness components are, $c_{11} = c_{22}$, $c_{33}$, $c_{44} = c_{55}$, $c_{66}$, $c_{13} = c_{23}$ and $c_{12} = (c_{11}-2c_{66})$. The first subscript on velocity is the propagation direction and the second subscript on velocity is polarization direction. Crack orientation distribution is treated the same way preferred orientation in a material is treated using the orientation distribution function. $W_{lmn}$ for even values of $l,m,n$ are real and as long as $n$=0, $W_{lmn}$ does not equal 0 for circular cracks. Therefore, $W_{220}$, 200, 420, 400, 440 are the only values that can exist in geological materials. For a material composed of cubic crystallites with overall orthorhombic sample symmetry only the 400, 420 and 440 exist, while odd numbered $l,m,n$ do not exist because of symmetry in the material (Sayers 1988).

### 1.5.3 Birefringence in graphite

The abundance of pores and microcracks in nuclear grade graphite prior to installation and operation in a reactor core, suggests that the birefringence effect should be seen and, like in rock, once degradation begins the graphite "fracture criticality" should be observed. Graphite that has been extruded might especially exhibit this behavior due to alignment of grains and microcracks. Monitoring this material throughout irradiation in a reactor core might show degradation by measuring the change in velocity and therefore elastic stiffness due to the same opening and closing behavior observed in rocks.

Dutton and Dewhurst (2007) measured anisotropy in thin, high porosity, pile grade A (PGA) graphite samples using laser generated ultrasound and detected the ultrasonic waves using EMATs. This method allowed them to record the changes in the longitudinal wave based on orientation of wave propagation through the material using an epicentral set-up of generator and receiver. Cylindrical samples were cut so that microstructure was oriented either perpendicular or parallel to the propagating waves. In this experiment shear waves were not detected. Limitations on sample thickness caused scattering of the ultrasonic waves which interfered with the shear wave detection. The results show that orientation of the microstructure impacts longitudinal velocity. Faster velocities were recorded for samples with microstructure parallel to wave propagation; therefore calculation of Young's modulus was also higher for this orientation.

Several methods were used by O'Brien *et al*. (1992) to measure texture in graphite of different grain size and porosity. The most significant methods were contacting ultrasonics and laser generation and detection of ultrasound using a Fabry-Perot interferometer. The Fabry-Perot has an advantage over the Michelson-type in that it does not require a polished surface to collect reflected light. Shear wave time-of-flight measurements were made with the contacting ultrasonic technique in N3M (moderate grain size graphite) and H451 (coarse grain). Two orthogonally polarized shear piezoelectric transducers were used in a pulse-echo configuration. By polarizing the propagating shear waves, birefringence was observed most strongly in specimens cut near the surface of both grades of graphite billets. For the non-contacting ultrasonic technique, longitudinal and surface Rayleigh waves were recorded. Despite both materials being successfully characterized by the contacting technique, the non-contacting technique was more dependent on pore size and reliable results were only obtained on the N3M graphite. The time-of-flight measurements for the Raleigh waves on N3M did follow trend with the shear waves recorded using the contacting technique. Neither technique showed any significant difference in the longitudinal wave velocity. Ultimately the authors state that the coarse grained H451 would not be suitable for interferometric detection even if the surface were polished because the microstructure would distort the ultrasonic signal path.

### 1.5.4 Comparing other techniques to ultrasound for measuring texture and the ODCs

Traditionally, X-ray diffraction pole figure plots are used to determine the orientation of crystals in a metal and, from the pole figure, orientation distribution coefficients can be calculated. Similarly, electron backscatter diffraction can also give a rough calculation of the ODCs. To improve on the accuracy of calculating the ODCs, ultrasound has begun to emerge as an accurate, inexpensive and transportable method to characterize the texture of a material. One ultrasonic technique that has proven to show results comparable to traditional techniques is the surface generated Lamb wave. (Palmer *et al*. 2008) In an experiment to compare ultrasound to EBSD in determining texture of thin aluminum alloy plates (0.5-1.5 mm thick), Lamb waves are generated and detected using non-contacting electromagnetic acoustic transducers that rotate above the specimen surface (Figure 10). Through-thickness EBSD measurements were taken by scanning a cross-sectional area of the sample (Figure 11). The results were used to calculate ODCs and compared to the Lamb wave measurements. Preferred orientation of the grains was seen to vary through the thickness of these very thin sheets. An example of EBSD results is shown in Figure 11.

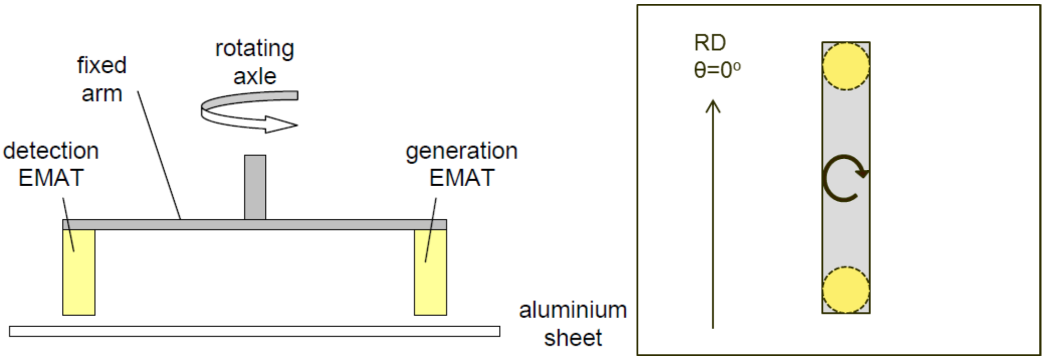

**Figure 10**: Experimental setup by Palmer using EMATs to generate and detect ultrasound for calculating the ODCs of aluminum

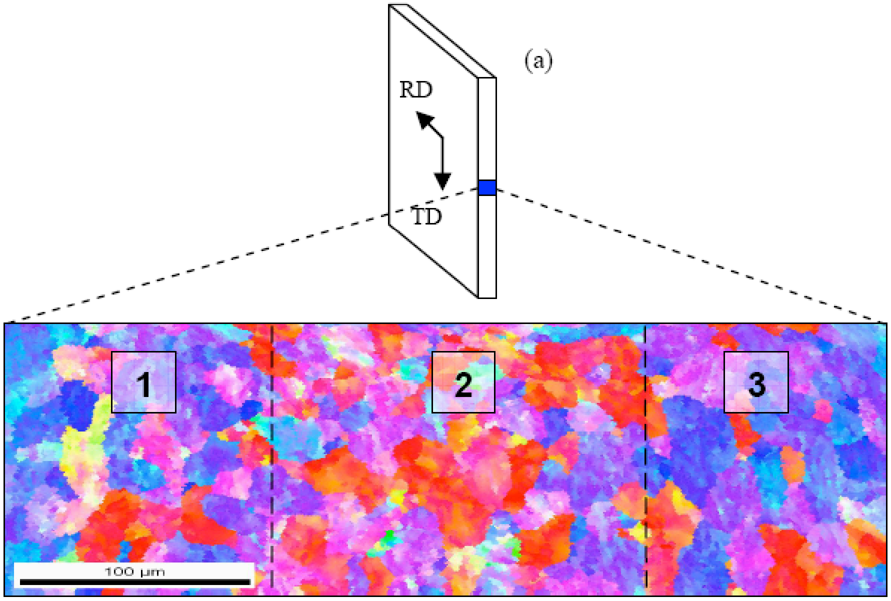

**Figure 11**: EBSD image taken from aluminum sheet and used to generate ODCs and compared to ultrasonic results (Palmer *et al*. 2008).

Figure 12, Figure 13, and Table 1 show the ultrasonic results were successful in measuring texture previously determined using EBSD. In many ways, ultrasonic results will be more useful than EBSD or XRD measurements mainly because the ultrasonic wave will measure the bulk elastic properties of the material, which is critical when calculating orientation distribution coefficients. In addition to accuracy, the information collected by Palmer's group shows that ultrasound can provide all necessary texture information much faster and at less cost than EBSD or X-ray diffraction. To improve further on texture characterization using ultrasound, it would be beneficial to use bulk waves so that the through thickness of a material could be examined, including any surfaces not accessible by ultrasonic equipment. We now ask, can we predict the correct ODCs for bulk material using ultrasound?

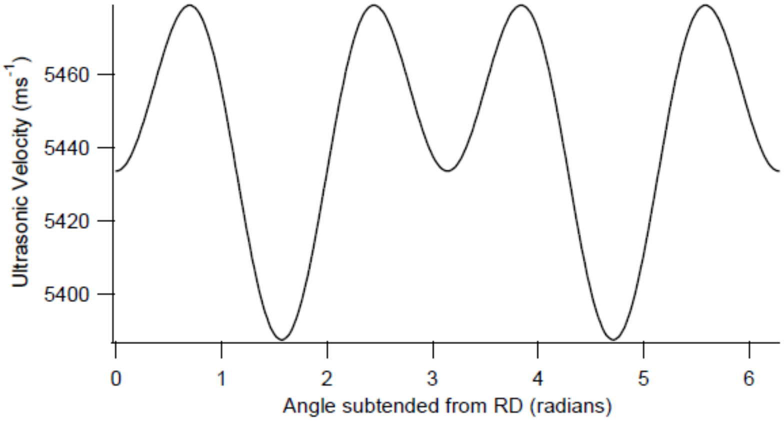

**Figure 12**: Predicted velocity using EBSD measurements (Palmer *et al*. 2008)

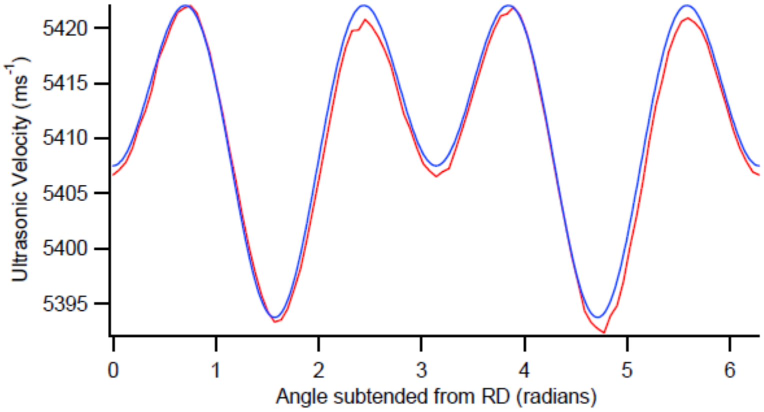

**Figure 13**: Measured ultrasonic velocities of lamb waves in Aluminum alloy 1.5mm thick shown with predicted velocities (Palmer *et al*. 2008)

**Table 1**: ODCs calculated from EBSD and ultrasound presented by Palmer *et al*. (2008)

| ODC | Predicted value from EBSD | Value from ultrasound |
|---|---|---|
| $\mathbf{W_{400}}$ | $-7.17 \times 10^{-3}$ | $-8.58 \times 10^{-3}$ |
| $\mathbf{W_{420}}$ | $-1.43 \times 10^{-3}$ | $-3.09 \times 10^{-3}$ |
| $\mathbf{W_{440}}$ | $2.24 \times 10^{-3}$ | $9.02 \times 10^{-4}$ |

Subsequent sections of this dissertation will show experimental results on an ultrasonic technique that uses the transverse waves to measure velocity at any polarization angle while keeping the propagation direction in the through thickness direction of a metallic plate. A laser point and line source are modeled to show isolation of the shear wave when shear wave birefringence is present in a material but difficult to distinguish, especially in aluminum where the material behaves nearly isotropically. Experiments using the laser line source are discussed and compared to electron backscattered diffraction results in order to describe texture. Orientation distribution coefficients are calculated from the experimental results to help show the variation in material properties present between samples even when samples are cut from the same stock. Line source measurements are also taken on some nuclear grade graphite samples to show the correlation between ultrasonic results and micrographs of the graphite, identifying the dependency of the waveforms on porosity. Finally laser point source results are shown on fatigued damaged aluminum monitoring changes in velocity as the number of fatigue cycles increases.

# 2 MODELING LASER ULTRASOINC PROCESSES

## 2.1 Laser generation of ultrasound

Ultrasound is most commonly generated by a contacting transducer but pulsed lasers have also been used. Both have advantages: the transducer is inexpensive and is fast and easy to use, while the laser has the ability to operate under any environmental and geometrical condition, and also produces a much broader frequency range. When looking for very small changes in material properties, access to laser generated ultrasound might uncover more information than a transducer could produce. For example, aluminum will have a compressive wave velocity of 6300 m/s. Using a 1064 nm pulsed laser with a 10 ns pulse length to generate ultrasound and an interferometer capable of detecting up to 50 MHz, one would generate wavelengths in the material between 60 μm and 6 mm (corresponding to 100MHz-1MHz) so that the material resolution from the laser-in laser-out system would be 100 μm.

In contrast, Stanchits *et al*. (2003) measured microcracks in granite (compressional velocity around 4820 m/s) with transducers having a range of 200-1200 kHz giving them a resolution of only 4 mm. They determine this wavelength to be much longer than microcracks in the rock which would be expected to be about 0.2 mm, roughly the grain size of the rock. Scattering from individual microcracks is not plausible but they may observe changes in the bulk material. In order to observe individual scattering they would need a frequency closer to 24 MHz.

## 2.2 Point source and line source ultrasonic generation

This work uses thermoelastic waves generated by a laser point or line source. The laser is focused to the highest possible intensity without removing material from the surface of the specimen thus leaving the specimen thickness unchanged. Not changing any of the material characteristics by the testing method will also allow us to repeatedly gather ultrasonic data from the same location until all necessary information has been extracted from the given specimen. A point source for ultrasonic generation will contain the longitudinal and two orthogonally polarized shear waves. Isotropic materials will appear to have only one shear arrival but use in an anisotropic medium, arrivals for both shear waves might be identified.

A simplified model of thermoelastic epicentral displacement by a point source, shown in Figure 14 has been developed by Rose:

$$g_z^H(0,h,t) = 4\Lambda b^2 h[\dot{F}_L(t,h) + \dot{F}_T(t,h)] \tag{25}$$

where

$$F_L(t,h) = -H(t-ah)(\zeta^2\alpha^2\beta\gamma R^2)_{\zeta=(t^2/h^2-a^2)^{1/2}} \tag{26}$$

$$F_T(t,h) = H(t-bh)(\zeta^2\alpha\beta^2\gamma R^2)_{\zeta=(t^2/h^2-b^2)^{1/2}} \tag{27}$$

$$\alpha = (a^2+\zeta^2)^{1/2}, \beta = (b^2+\zeta^2)^{1/2} \tag{28}$$

$$\gamma = (b^2+2\zeta^2), R = (\gamma^2 - 4\zeta^2\alpha\beta)^{-1} \tag{29}$$

and where $a$ and $b$ are the reciprocals of the longitudinal and shear wavespeeds, $4\Lambda b^2 h$ is a scaling factor, $h$ is the thickness of the sample, $t$ is time, and *H(t)* is the Heaviside step function.

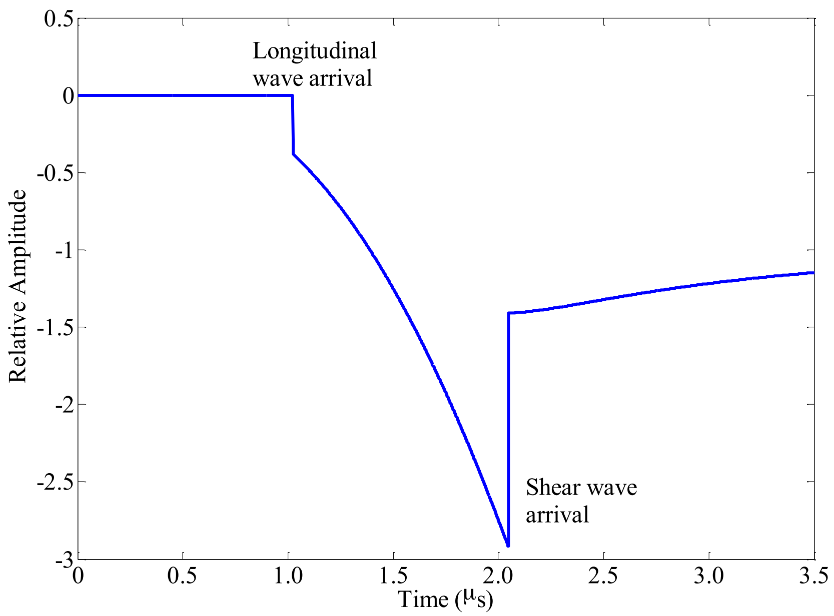

**Figure 14**: Predicted ultrasonic displacement from a laser point source using Rose's model (eq. (24))

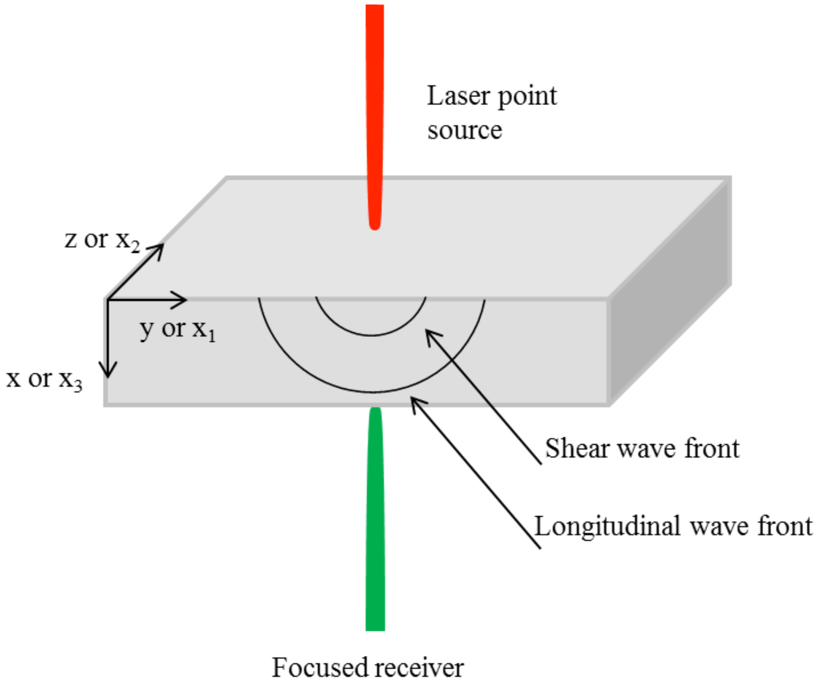

**Figure 15**: Schematic for point source ultrasonic generation with interferometric detection

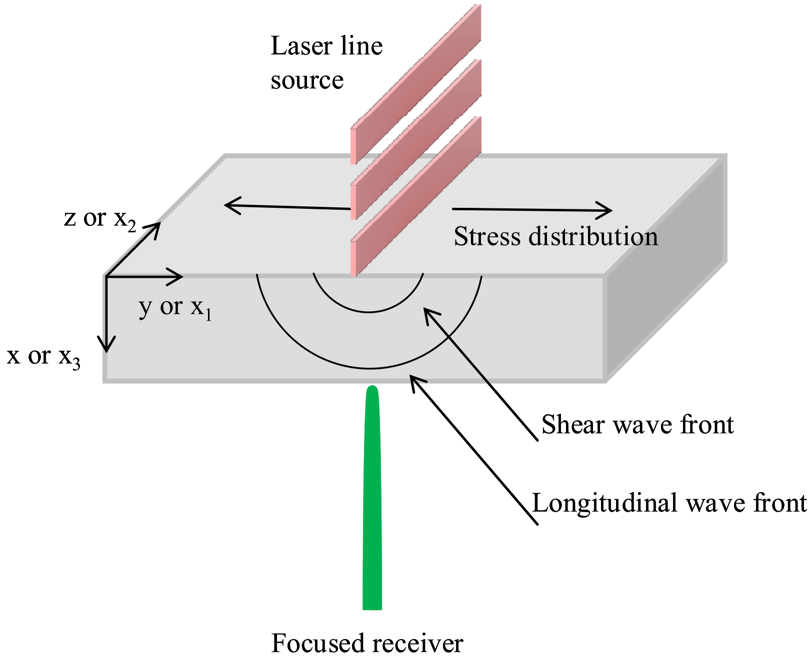

**Figure 16**: Diagram of laser line source propagating bulk waves through a material with an epicenter placed receiver

For the line source, directionality is imposed by the line and allows us to concentrate more energy onto the surface and into one of the shear waves. The longitudinal wave velocity does not change between the point and line source but by using the line source the polarization of the shear wave is forced and the intensity dependent on the length of the line. The longer the line the stronger the perpendicular shear wave (xy in Figure 16) will be, thus masking the arrival of the second shear wave. Using the methods developed by Payton (1983) and Hurley (1998), a transversely isotropic model (Figure 17) will aid in the identification of wave arrival times for both the longitudinal and shear waves. The model displays the potential outcomes of laser line generated ultrasound. In the transversely isotropic case, the ultrasonic wave will propagate along the axis of symmetry giving the fastest arrival for both the longitudinal and shear waves. When anisotropy is introduced into the material, such as in a rolled plate or extruded bar, ultrasonic waves propagating perpendicular to the axis of symmetry will share a common longitudinal arrival time but differ in shear wave speed. This is due to the dependence of ultrasonic polarization on material stiffness. The following equations come from the model showing two different longitudinal waves $v_2$ and $v_3$ but keeping the shear wave constant. This corresponds to the blue and red lines, respectively, in Figure 17.

$$v_3 = \tfrac{1}{2\pi}\,\mathrm{Re}[H(\tau_1 - 1)B_1 \frac{s}{\Gamma_2^{1/2}} \frac{\partial \Gamma_2}{\partial \tau_1} + H(\tau_2 - 1/_{\alpha^{1/2}})B_2 \frac{s}{\Gamma_2^{1/2}} \frac{\partial \Gamma_2}{\partial \tau_2}] \tag{30}$$

where,

$$B_1 = \left(\left(\frac{c_{44}}{\rho}\right)^{-1/2} \frac{\kappa\gamma_2^2}{s}\right)\left[(\gamma_2^2 + 1)(1-\kappa) - \alpha\gamma_{33}^2\right]\gamma_{31} \div (D) \tag{31}$$

$$B_2 = -\left(\left(\frac{c_{44}}{\rho}\right)^{-1/2} \frac{\kappa\gamma_2^2}{s}\right)\left[(\gamma_2^2 + 1)(1-\kappa) - \alpha\gamma_{31}^2\right]\gamma_{33} \div (D) \tag{32}$$

$$\Gamma_2 = \gamma_2^2 = \frac{1}{2\beta}[\gamma_3^2 x - (\beta+1) \pm [(\gamma_3^2 x - (\beta+1))^2 - 4\beta(\alpha\gamma_3^4 - (\alpha+1)\gamma_3^2 + 1)]^{1/2}] \tag{33}$$

$$\frac{\partial \Gamma_2}{\partial \tau} = \frac{1}{x_3}\frac{\partial \Gamma}{\partial \gamma_3} \tag{34}$$

$$\frac{\partial \Gamma_2}{\partial \gamma_3} = \frac{2x\gamma_3\Gamma_2 + 2(\alpha+1)\gamma_3 - 4\alpha\gamma_3^3}{2\beta\Gamma_2 + (\beta+1) - x\gamma_3^2} \tag{35}$$

$$D = \kappa(\gamma_{31} - \gamma_{33})\{[\gamma_2^2 + 1][2(1-\kappa)\gamma_2^2 - (X\gamma_2^2 + \alpha)] - \alpha\gamma_{31}\gamma_{33}\} \tag{36}$$

$$\gamma_{33} = [2\alpha]^{-1/2}\{[(\alpha+1) + x\gamma_2^2] - \varphi^{1/2}\}^{1/2} \tag{37}$$

$$\varphi = [(\alpha+1) + x\gamma_2^2]^2 - 4\alpha[\beta\gamma_2^4 + (\beta+1)\gamma_2^2 + 1] \tag{38}$$

with,

$$\kappa = 1 + \frac{c_{23}}{c_{44}}\ ,\ \alpha = \frac{c_{33}}{c_{44}}\ ,\ \beta = \frac{c_{11}}{c_{44}},\ x = 1 + \alpha\beta - \kappa^2 \tag{39}$$

$$\begin{aligned} \tau_1 &= \gamma_{31}x_3 \\ \tau_2 &= \gamma_{33}x_3 \end{aligned} \tag{40}$$

The same equations apply to v$_2$ but instead using subscripts 21 and 23 to indicate a change in propagation direction.

$$v_2 = \tfrac{1}{2\pi}\operatorname{Re}[H(\tau_1 - 1)B_1 \frac{s}{\Gamma^{1/2}_3}\frac{\partial\Gamma_3}{\partial\tau_1} + H(\tau_2 - {}^{1}\!/_{\alpha^{-1/2}})B_2 \frac{s}{\Gamma_3^{1/2}}\frac{\partial\Gamma_3}{\partial\tau_2}] \tag{41}$$

$$B_1 = \left(\left(\frac{c_{44}}{\rho}\right)^{-1/2}\frac{\kappa\gamma_3^2}{s}\right)\left[(\gamma_3^2 + 1)(1-\kappa) - \alpha\gamma_{23}^2\right]\gamma_{21} \div (D) \tag{42}$$

$$B_2 = -\left(\left(\frac{c_{44}}{\rho}\right)^{-1/2}\frac{\kappa\gamma_3^2}{s}\right)\left[(\gamma_3^2+1)(1-\kappa)-\alpha\gamma_{21}^2\right]\gamma_{23} \div (D) \tag{43}$$

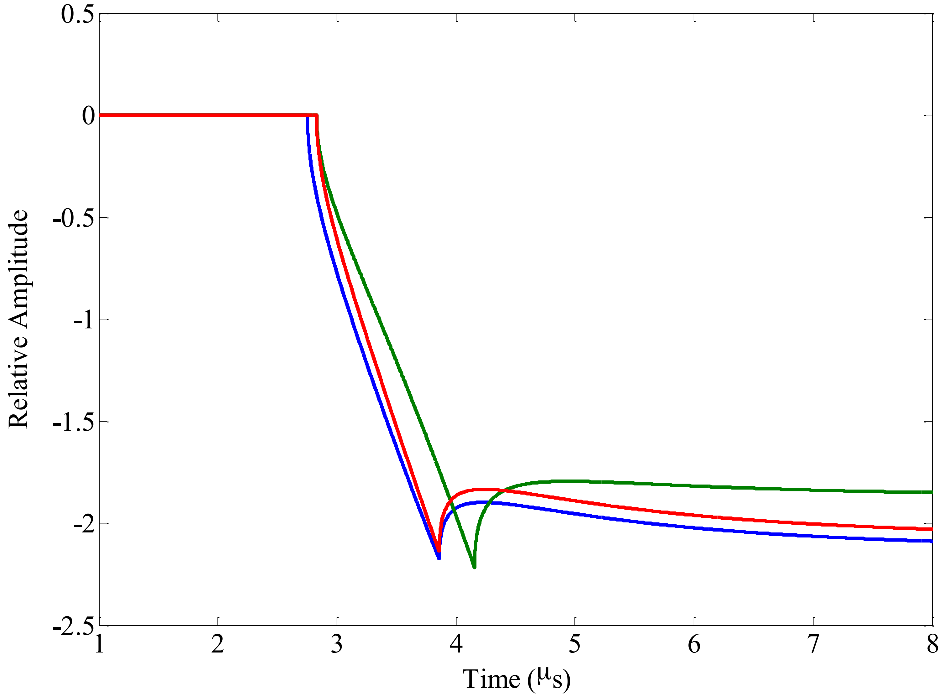

**Figure 17**: Model used to identify shear arrival, specifically for a transversely isotropic material (time displayed to match graphite). Blue- Transversely isotropic: wave propagation along axis of symmetry, Green- Isotropic: laser line parallel to axis of symmetry, Red- Line perpendicular to axis of symmetry.

The laser line source has been implemented by authors such as Wang *et al.* (2008) to analyze wave propagation in the principal directions of a fiber reinforced composite plate while assuming transverse isotropy. When the laser line is perpendicular to the fiber direction (anisotropic plane), the elevation in temperature and the stress fields are symmetric about the isotropic plane and ultrasound propagates parallel to the anisotropic plane. When the laser is parallel to the fiber direction (isotropic plane), waves propagate parallel to the isotropic plane. In general, there are three possible ultrasonic modes generated: pure shear, quasi-shear, and quasi-longitudinal. With a laser line source, however, Wang *et al*. (2008) noted that no pure shear mode is generated when polarization is perpendicular to the fiber direction. Pan *et al*. (2003) also used a line source to predict the acoustic field generated in a transversely isotropic cylinder. Their notation relates the $C_{11}$ and $C_{12}$ elastic constants to the plane perpendicular to the z-axis where the z-axis is the direction along the length of the cylinder and to which the laser line is parallel. In this case the group neglects thermal effects and instead uses the step function developed by Rose (1984) in the thermoelastic case and a dipolar force to represent the source shape. In the non-ablating regime, the surface yields a waveform model dominated by a step function (Rose 1984; Scruby & Drain 1990:277). Bernstein and Spicer (2000) and Hutchins (1981) also describe the model of the line source as a two-dimensional shear stress dipole model. Where a single point source includes the volume expansion equivalent to three mutually perpendicular dipoles, the line source can be represented as an array of points where the line of expansion has two equal and opposite stresses (dipoles) perpendicular to the line direction. Directivity patterns for a laser line source in aluminum (Figure 18) propagating in a cylindrical half-space in the thermoelastic regime show the energy radiated to be a maximum at thirty degrees from the surface normal. These patterns are for a thick sample, but in thin plates energy peak maxima can be detected directly across from the source. The orientation of the line will tell us the location of the fatigue-damaged region, assuming that changes in material properties due to fatigue are identifiable by this ultrasonic method.

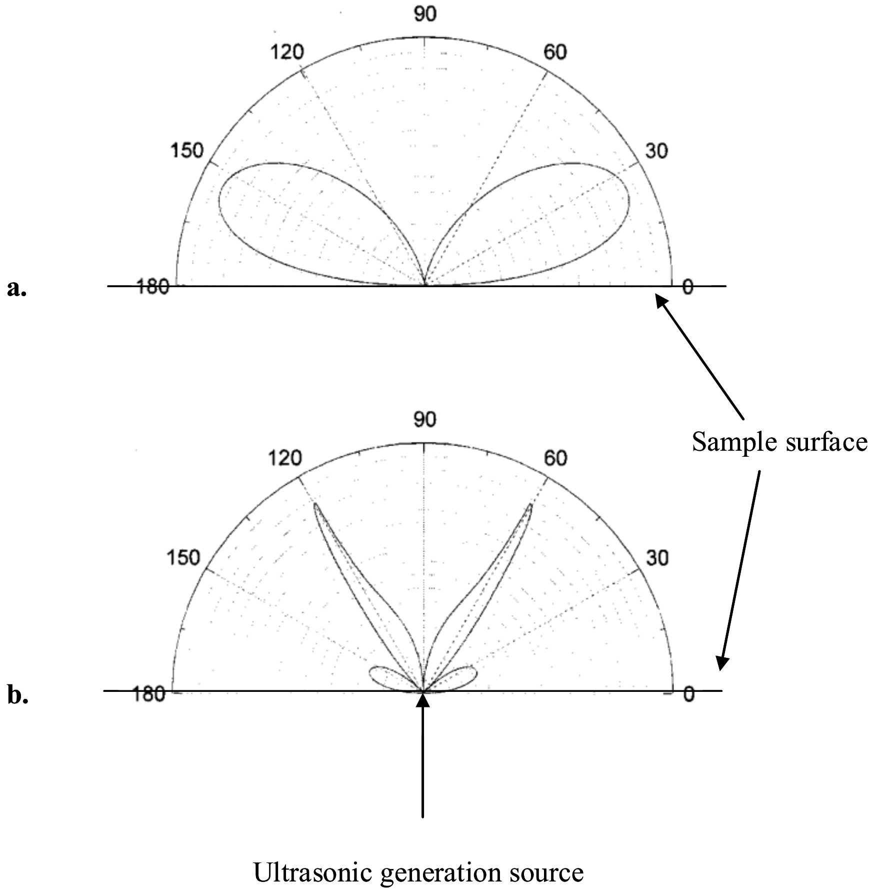

**Figure 18**: a. Longitudinal, b. shear, directivity patterns, experimental laser line source (Bernstein & Spicer 2000).

Additional instances with authors changing the propagation direction of the ultrasound occur in Aussel *et al.* (1988) where equations for displacement are given for the thermoelastic and ablative regime along with experimental waveforms in each regime from semi-cylindrical and rolled plate specimens. Epicentral measurements were taken on the rolled plates, while radial measurements were taken with an interferometer at different angles on the semi-cylindrical specimens.

In the next section, we will show data resulting from the rotation of a laser line source on rolled or extruded metal plates and how the shear wave velocity can be controlled by enhancing one of the polarizations. There is measurable variation in the velocity that is dependent on the orientation of the line source relative to the rolling or extruded direction of the plate. This leads us to calculate the texture of a material and quantitatively compare this to texture results from electron backscatter diffraction.

# 3 LASER ULTRASOUND FOR TEXTURE ANALYSIS

## 3.1 Materials and sample preparation

This chapter will explore the capabilities of a laser line source to characterize materials in terms of stiffness and use results to calculate texture described by the orientation distribution coefficients. Metal alloy materials used include as-received rolled square plates of alpha brass (66% Cu, 34% Zn) and copper (measuring 2 in x 2 in x 0.1875 in), as well as 2 in x 2 in x 0.25 in rolled and extruded aluminum 2024-T351 (Cu rich) and extruded 6061 (Mg rich) – see Table 2. The addition of copper and brass to the sample set was useful in characterizing materials that are known to be highly anisotropic. All three materials have individual crystallites with cubic symmetry, but being rolled makes the overall sample symmetry orthorhombic. Including the extruded samples, whose overall sample symmetry is transversely isotropic, will give us a direction in the material that might behave closest to an isotropic material when the shear wave is polarized perpendicular to the extruded direction.

**Table 2:** Sample list for metal alloy materials investigated using laser line source ultrasonics

| **Sample** | **Alloy** | **Thickness** | **Density** |
|---|---|---|---|
| **Al 1** | 2024-T351 rolled | 0.627 cm | 2.804 g/cm3 |
| **Al HT** | 2024 rolled, heat treated | 0.616 cm | 2.765 g/cm3 |
| **Al 3** | 2024 extruded isotropic round | 0.635 cm | 2.770g/cm$^3$ |
| **Al 4a** | 6061 extruded | 0.6337 cm | 2.697 g/cm3 |
| **Al 4b** | 6061 extruded isotropic round | 0.632 cm | 2.697 g/cm3 |
| **Al 5** | 2024-T351 Extruded square bar | 0.627 cm | 2.773 g/cm3 |
| **Al 6** | 2024 extruded transverse square bar | 0.312 cm | 2.789 g/cm3 |
| **Al 8** | 2024-T351 rolled | 0.641 cm | 2.777 g/cm3 |
| **Brass 1** | 64/36 rolled | 0.4646 cm | 8.449 g/cm3 |
| **Brass 2** | 70/30 rolled | 0.475 cm | 8.427 g/cm3 |
| **Copper 1** | Rolled, unknown alloy 99.9% pure | 0.461 cm | 8.776 g/cm3 |

In addition, nuclear grade graphite has been a large portion of the study on preferred orientation. Isotropic cokes form isotropic or near-isotropic graphite. This type is generally preferred for nuclear reactors and includes petroleum cokes (oil derivatives) and pitch cokes (coal tar pitch). Anisotropic cokes (like needle coke - a highly crystalline petroleum coke) have a coefficient of thermal expansion, thermal conductivity and electrical resistivity that exhibit anisotropic qualities. Graphite produced from these cokes would be susceptible to high internal stresses and cracking caused by anisotropic dimensional changes from irradiation if used in a nuclear reactor (Burchell *et al*. 2007).

Four different grades of nuclear graphite have been acquired for ultrasonic testing and are currently or have once been candidates for reactor cores (Table 3). Each varies in porosity and pore and grain size, as well as the portion of the billet from which a sample was extracted. These graphite grades are known to comply with the chemical purity requirements of ASTM standard D 7219-08. However, it is unknown at this time whether all grades listed on the table were processed to meet these established standards. While some grades are no longer commercially produced, the sample set provides a broader representation of graphitic microstructures.

For the current ultrasonic arrangement, specimens from each graphite grade were cut into 5 cm x 5 cm x 0.635 cm plates. Like the metal samples, one side of each specimen was polished to a 1 μm, semi-mirror finish and ultrasonically cleaned in a water bath. Specimens were allowed to dry before ultrasonic measurements were made to minimize effects related to excess water trapped in the pores.

**Table 3**: Nuclear grade graphite samples with currently known information and processing history

| **Graphite** | **Manufacturer** | **Coke** | **Processing** |
|---|---|---|---|
| **NBG-18** | SGL | Pitch | Vibramolded, large grain size, up to 1.6 mm |
| **NBG-18** | SGL | Pitch | Top of billet |
| **PCEA-4** | Graftech | Petroleum | Extruded, medium grain size |
| **BAN** | Graftech | Needle-secondary Petroleum | Extruded, reconstituted, small grain size |
| **IG-110** | Toyo Tanso | Petroleum | Isostatically pressed, superfine grain size |

## 3.2 Laser line source generation to assess material anisotropy

When making remarks about the location of the laser line source, we will refer to any angle as being relative to the rolling direction. Particle displacement occurs perpendicular to the line, which we will call polarization. We consider the line oriented perpendicular to the rolling direction to be zero degrees, as shear waves are polarized in the rolling direction at this angle. When the line is parallel to the rolling direction, they are polarized in the transverse direction – or 90 degrees from the rolling direction (Figure 19).

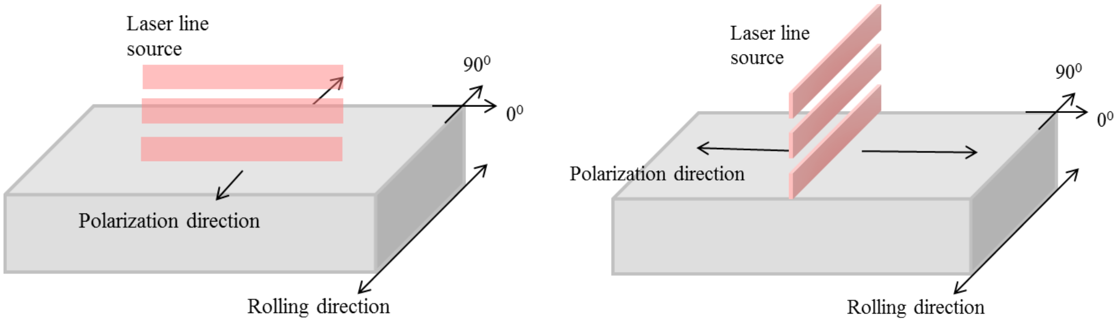

**Figure 19**: Orientation of the line source relative to the rolling direction.

For ultrasonic wave generation, a pulsed Nd:YAG 1064 nm laser is first passed through a filter to reduce the initial energy. To transform the laser into a line source, the beam is routed through a double concave lens and a double convex lens for expansion and collimation, and then finally focused into a line with a cylindrical lens. Our resulting line measures approximately 20 mm x 0.35 mm with a fluence of 0.1 J/cm$^2$ for thermoelastic wave generation.

### *Detection by Transducer*

Ultrasonic waves are detected using the 1.5 MHz conical transducer coupled to the back side of the selected material. Each sample is mounted onto a 360-degree rotational stage, with the initial laser line positioned perpendicular to the rolling direction of the material (zero degrees). While keeping the laser line at this fixed position, the sample is rotated at 10-degree intervals from zero to 360 degrees, with an additional point taken at 45 degrees. Data were recorded at each interval, and each interval contains an average of 500 waveforms for noise reduction. Recording all of the intermediate angles displays a change in wavespeed relative to the rolling direction that can be displayed as slowness or stiffness plots.

### *Detection by Interferometer*

The same experiment was done using a Michelson-type interferometer rather than the transducer to detect displacement. This method was chosen as a way to verify the sensitive results obtained by the transducer while also eliminating the possibility of contamination due to the nature of using a transducer and couplant. Although the signal-to-noise ratio may be much lower if not carefully dealt with, we believe the overall experimental error will be much lower and more consistent with this non-contacting approach.

Both the ultrasonic generation beam and the receiving beam are arranged to make contact with the exact center of the sample but opposite one another. As the sample is rotated we must check that there is no tilt in the sample mount so that the receiving beam does not wobble around the reference and cause a voltage drop or an interruption in interference altogether. Data were collected in the same manner as the transducer, with the sample rotating in 15-degree intervals and 500 waveforms averaged at each angle.

The same sample set was used for both the interferometric detection and the transducer detection, with the exception that all samples were polished on one side to a one-micron mirror finish. In addition to the rolled plate specimens, extruded bar specimens for brass and aluminum were cut in the transversely isotropic direction and from the middle along the isotropic (elongated) direction.

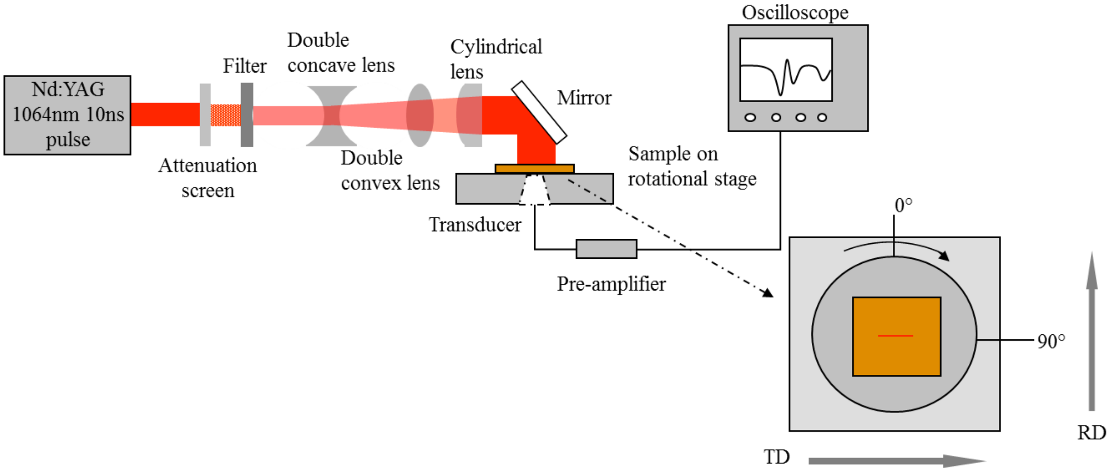

**Figure 20**: Experimental apparatus showing the laser line focused onto the sample surface oriented perpendicular to the rolling direction with ultrasonic detection using a contacting transducer

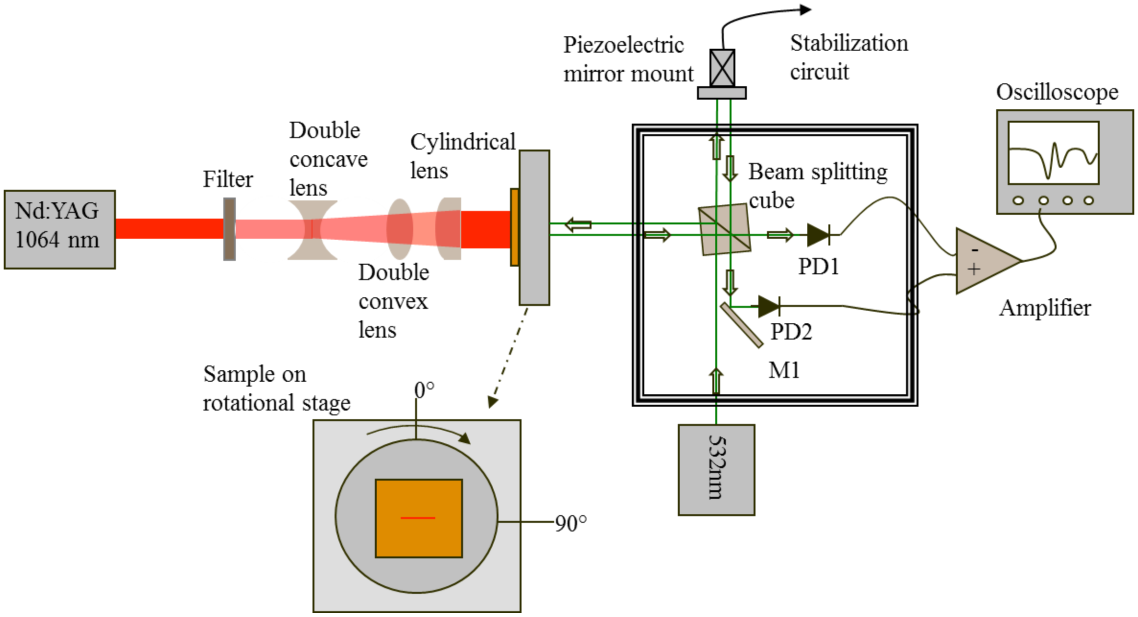

**Figure 21**: Experimental apparatus showing the laser line focused onto the sample surface oriented perpendicular to the rolling direction with ultrasonic detection using an interferometer

### 3.3 Line source results on as-received metal alloys

To observe shear birefringence in the metal alloys, arrival times of the shear wave must be carefully monitored as differences in shear arrivals can be very small especially in nearly isotropic materials such as aluminum. Figure 22 displays three waveforms from Al 3 (extruded 2024 round bar, waves propagating along extrusion direction). As expected, the waves have the same longitudinal (1μs) and shear (2μs) arrival times regardless of line orientation (0, 45, or 90 degrees). Figure 23 displays waveforms from aluminum 2024 extruded square bar, Al 5 and Al 6 with time normalized to the first longitudinal arrival - set at 0.5. Al 5 is cut in the transverse direction and waves propagate along the extruded direction. This corresponds to the line source model as having the fastest arrival times for both the longitudinal and shear waves. Al 6 is cut out along the extruded direction so that ultrasonic propagation is perpendicular to the extruded direction. The red line corresponds to the line oriented such that shear waves are polarized parallel to the rolling direction, and the green line corresponds to shear waves polarized perpendicular to the rolling direction. These waves agree with the line source model (Figure 24) showing that while longitudinal arrivals match up, there is slight variation in shear arrival with the red waveform arriving just ahead of the green waveform (isotropic direction). The discrepancy in this plot is between the two samples. While these waveforms have been normalized for sample thickness, the shear arrival of the blue line should correlate with the shear arrival of the red line. According to the model, following the shear arrival the amplitudes should nearly match with the blue line only slightly greater initially. Our data show the blue line to have a greater positive amplitude. These discrepancies could be due to laser intensity variations, mis-alignment of epicentral placement of lasers, or unaccounted sample anomalies.

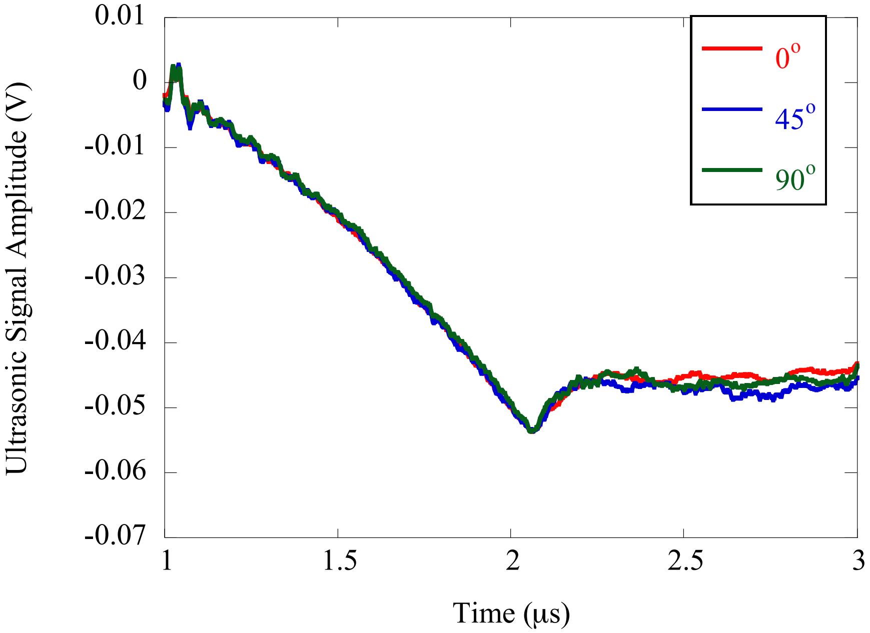

**Figure 22**: Aluminum sample Al 3, line propagating along extruded direction

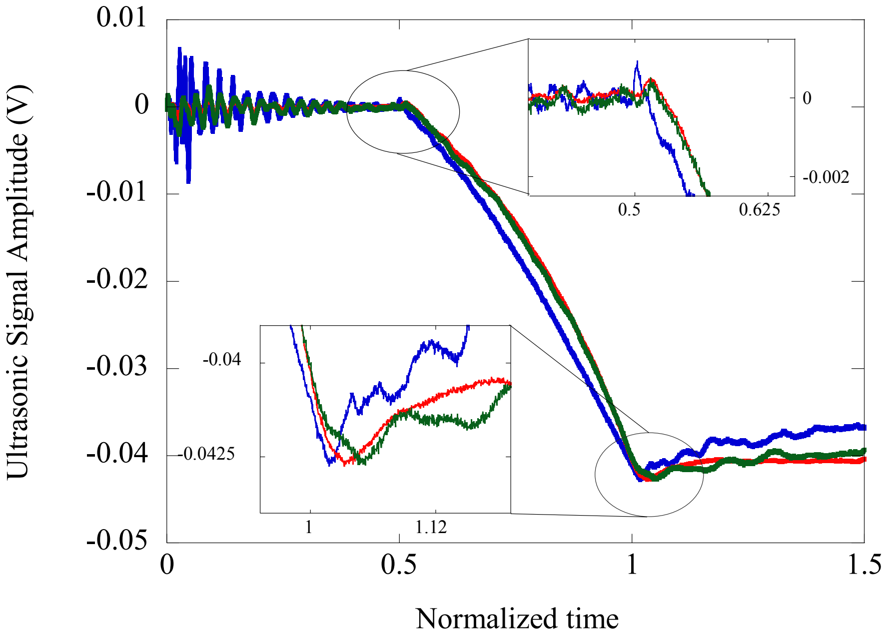

**Figure 23**: Blue line from Al 5 (square extruded 2024), green and red lines from Al 6 (cut perpendicular to extruded 2024 square bar) Blue: Transversely isotropic sample Red: Line perpendicular to axis of symmetry, Green: Isotropic – Line oriented along rolling direction

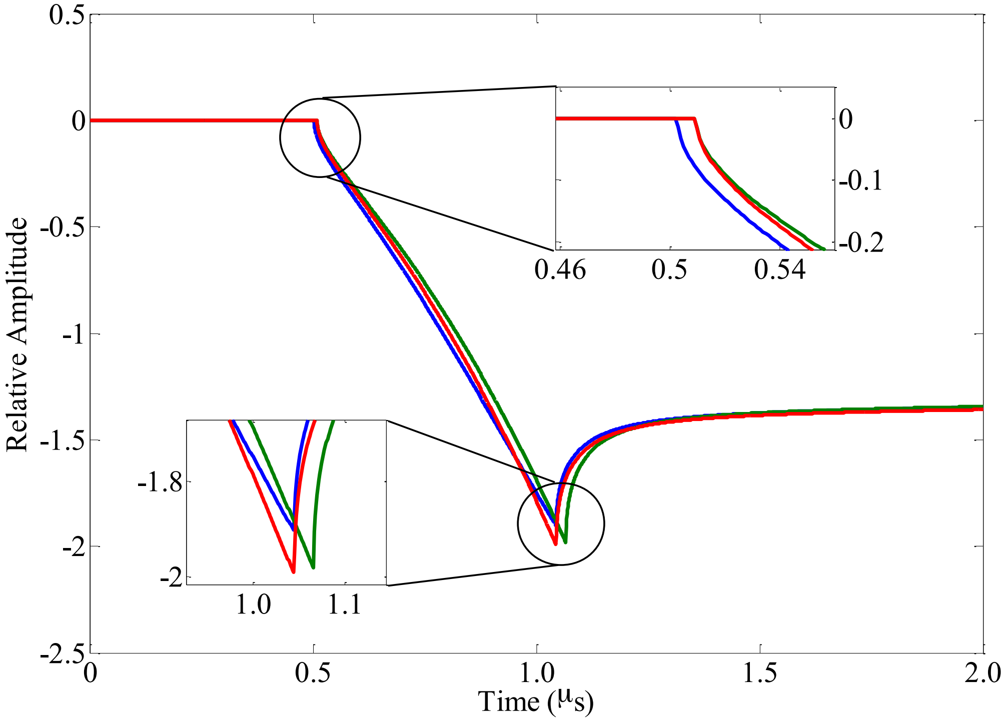

**Figure 24**: Model corresponding to Al 5 and Al 6. Blue: Transversely isotropic – wave propagation along axis of symmetry, Green: Isotropic – line parallel to axis of symmetry, Red: Line perpendicular to axis of symmetry

The following symmetry plots are made by measuring the arrival of the dominating shear wave or earliest arrival of the shear wave as shown in Figure 23. In some cases both shear waves appear, but one still has the greater, more defined amplitude. After deciding the time-of-flight for the shear wave, velocity is calculated using $v = h/t$ where $h$ is thickness and $t$ is time-of-flight. Next, stiffness is calculated with $c_{ij} = \rho v^2$ and using the density ($\rho$) values in Table 2. Polar plots can be made with stiffness as a function of laser line angle relative to the rolling direction.

Isotropic aluminum data were collected from an extruded square bar of 2024-T351 and an extruded round bar of aluminum 2024. The samples were cut from the bars such that wave propagation was along the extruded direction (Figure 25). While shear velocity should remain constant regardless of polarization direction in either case, there is still a 1-2% variation between the maximum and minimum calculated elastic stiffnesses (Figure 26). Two scales are shown for each data set to enhance the degree of variation observed from the shear wave. Error will be small and difficult to measure in these experiments since optical alignment is critical for data acquisition to be possible. In fact, the ultrasonic signal is what is used to ensure final alignment and minimize error. The line source and receiving point source are focused to the center of the sample, but the point source can be more difficult to find that center of rotation since it is unable to leave an ablative mark showing its path on the sample. It is centered using an iris mounted to the back of the sample be even this cannot ensure perfect alignment. The errors shown are from one complete rotation of the line assuming a zero and 360 degree rotation would have no change in the final position or beam profile of the line and each degree should have the same time-of-arrival. This will be true if the receiving point source is perfectly centered.

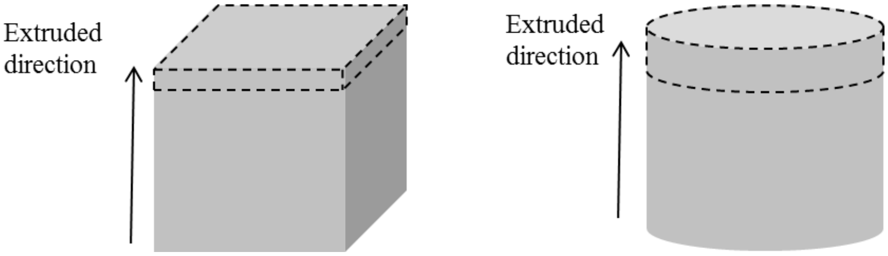

**Figure 25:** Orientation of sample extraction for extruded square and round bar stock

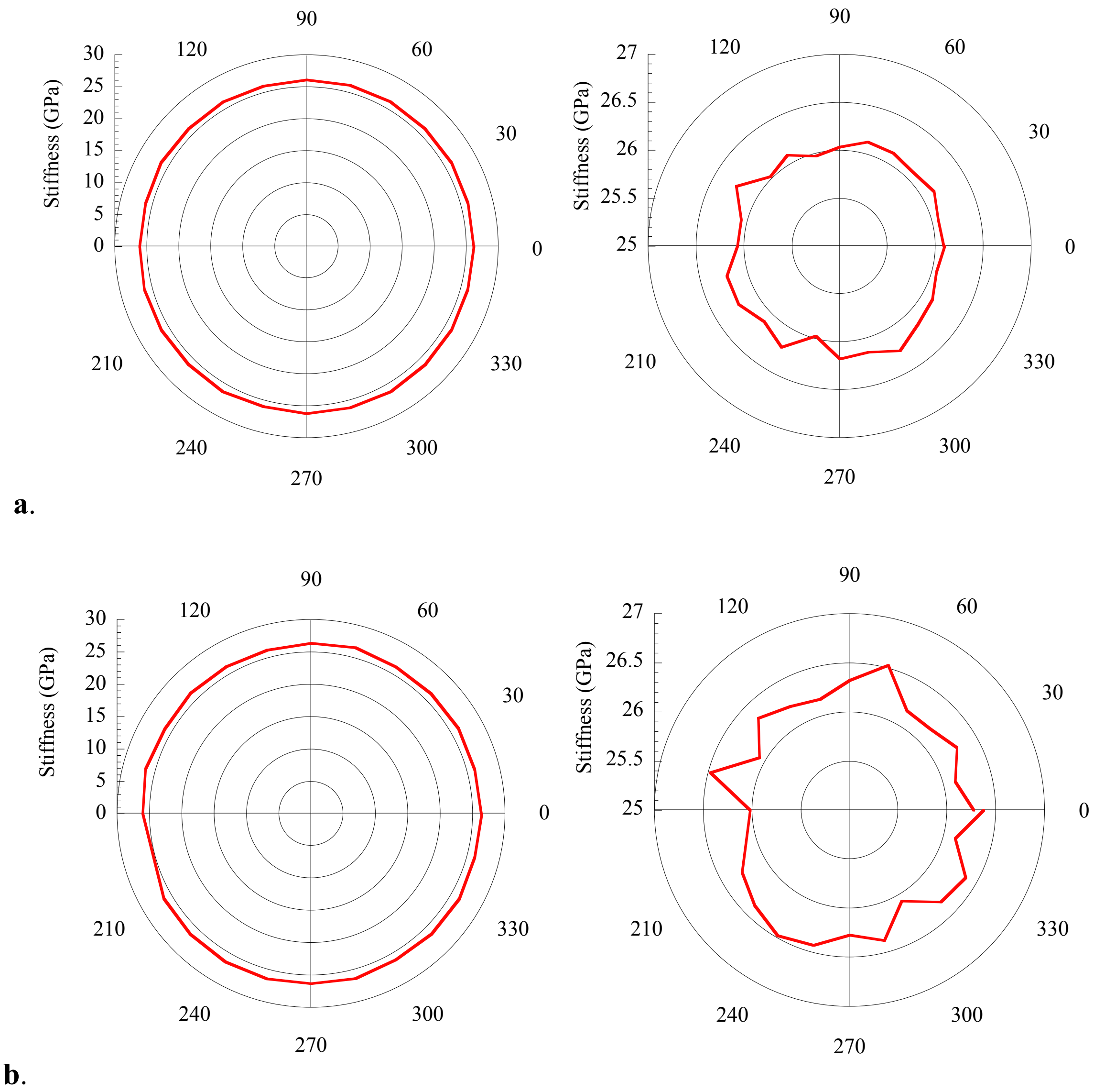

**Figure 26**: **a.** Extruded (square bar) aluminum 2024-T351 (Al 5) oriented for isotropic data acquisition with 1.09% variation in stiffness and 0.0038% error at one complete rotation (measurements at 0 and 360 degrees) **b.** Extruded (round bar) aluminum 2024-T3 (Al 3) data taken along extruded direction, 1.93% variation in stiffness and 0.97% error

To isolate changes in elastic stiffness to either rolling-induced anisotropy or anisotropy inherent to the material, a sample of aluminum 2024 was heat-treated following ASM recommendations. The sample was brought to 497°C and held for 55 minutes, then quenched in room-temperature water. This procedure would ideally remove stress associated with initial processing of the material such as large dislocation pileups due to cold rolling and allow the texture of the material to reconfigure. Figure 27(a) shows the result of a 360-degree rotation using a transducer for data acquisition. It is obvious that the transducer has a larger error in this ultrasonic testing arrangement because there is greater mismatch when the sample is fully rotated back to the original position. One possibility for this mismatch is that the exact location of the piezo sensor on the transducer may not be centered on the contact foot. In addition, the use of contacting couplant creates additional refraction of the ultrasonic wave as the sample glides over the surface of the transducer. Figure 27(b) displays the interferometric results using the same heat treated sample. The recorded times-of-flight had very little variation as the sample was rotated. The improved accuracy with this technique is also apparent with error calculated to be zero because the arrival times for 0 and 360 degrees were unchanged.

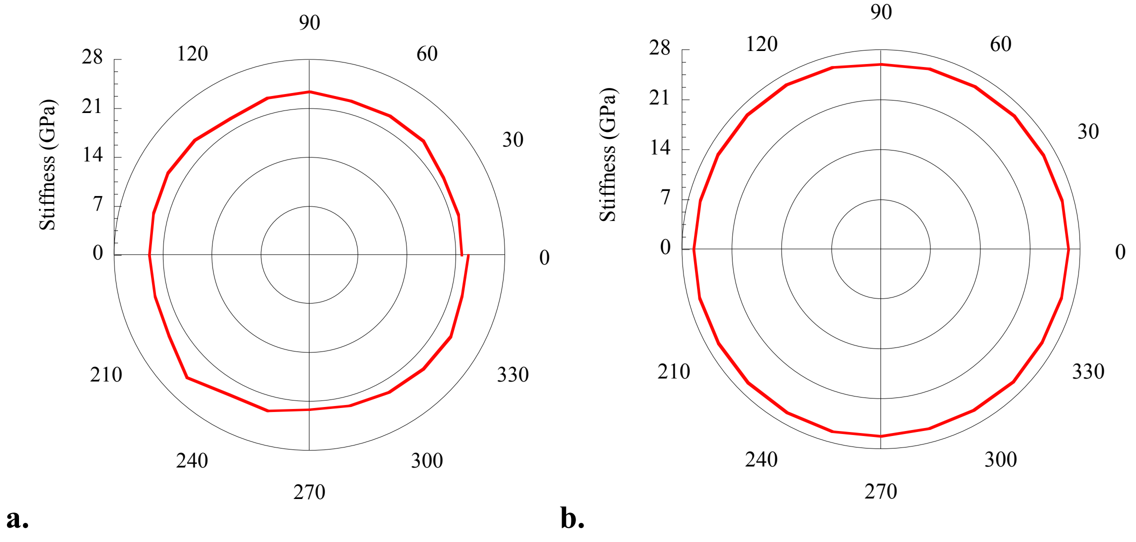

**Figure 27**: Heat-treated aluminum alloy 2024-T351 (Al HT) a. Transducer (12.18% variation, 4.15% error) and b. Interferometer (2.57% variation, 0% error)

After these initial tests to establish a standard, the same ultrasonic testing procedures were used for several samples of aluminum. Rolled aluminum plates (Figure 28) show some dependency of stiffness on line orientation with some amount of two-fold symmetry displayed.

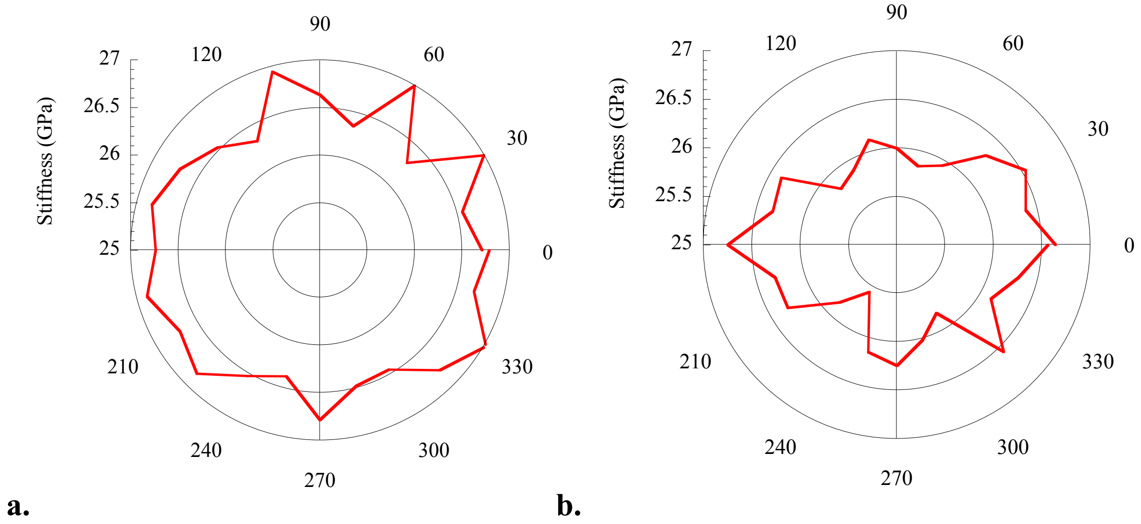

**Figure 28**: Rolled aluminum 2024-T351 data acquired by interferometer (a) Al 8 with 2.6% variation and 0.29% error, and (b) Al 1 with 4.4% variation and 0.3% error

Data taken in the transverse direction of an extruded bar (Figure 29) had a more exaggerated effect on the two-fold symmetry and is shown along with an ellipse for comparison.

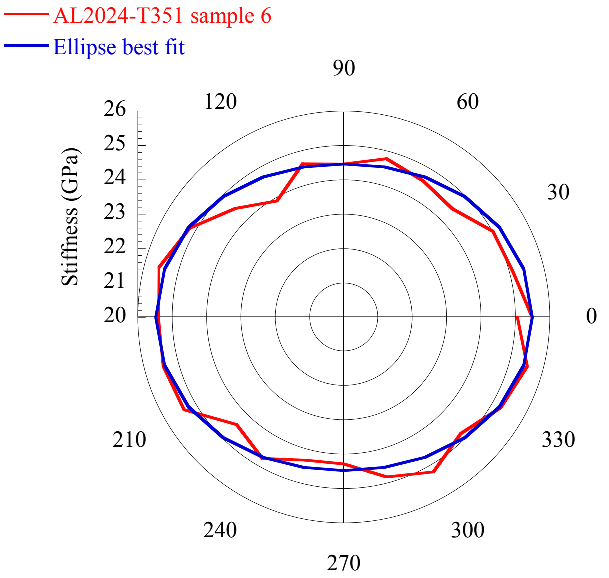

**Figure 29**: Extruded aluminum 2024 (Al 6) data acquired by interferometer with 6.5% variation and 1.7% error. The results are shown with an ellipse for clarification of the changes in elastic stiffness.

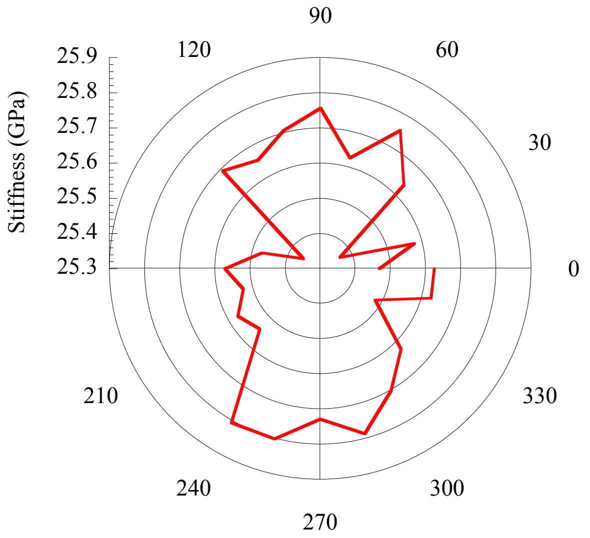

**Figure 30**: Aluminum 6061 (Al 4) extruded bar with propagation perpendicular to the extruded direction and taken with the interferometer having 1.7% variation and 0.6% error

For verification of our experimental apparatus, the addition of copper helps us to understand the components of the ultrasonic waveforms that undergo changes as a function of material qualities and wave polarization. Many authors, such as Thompson *et al*. (1989), have characterized the texture and calculated the orientation distribution coefficients for copper and have had great success when using it as a model system. Contrary to the results discussed by Foster *et al*. (1999), our data show copper to have some rolling-induced anisotropy. Like the rolled aluminum alloy, pure copper sometimes demonstrates a two-fold symmetry when wavespeed is displayed in a polar plot against the laser line orientation. Figure 31 compares ultrasonic data collected using an interferometer and then using a transducer on the same rolled copper sample. When polarization of the line source is parallel to the rolling direction (zero degrees) elastic stiffness for the material is at a maximum. The data reveal similar trends for both cases, although the interferometric data show less variation at corresponding angles, and a difference in calculated elastic stiffness is noticeable between the two detection methods.

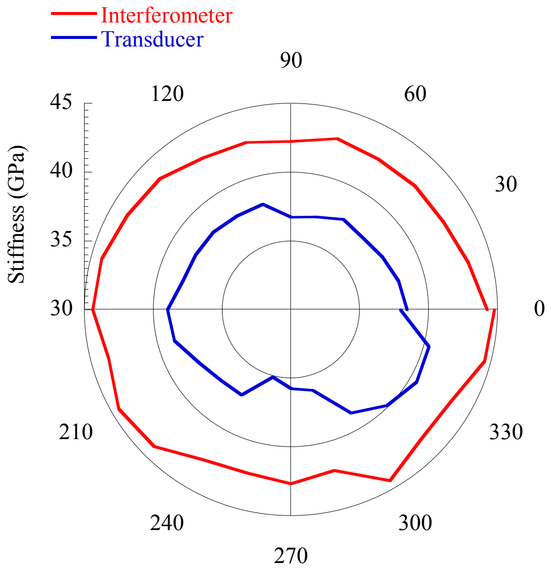

**Figure 31**: Stiffness for rolled copper calculated from ultrasonic data by interferometric (red) with 5.9% variation, 1.16% error, and transduction (blue) with 13.1% variation, 1.26% error.

Using shear velocity measurements and density for the alpha-brass, we can calculate stiffness and show variations with respect to the direction of wave propagation. The brass alloy Cu64Zn36 (Figure 32) showed a very clear two-fold symmetry with every data set taken regardless of the method used (laser or transducer detection). By repeating the experiment on the same brass sample, we see consistent results exhibiting the greatest stiffness 45 degrees from the rolling direction.

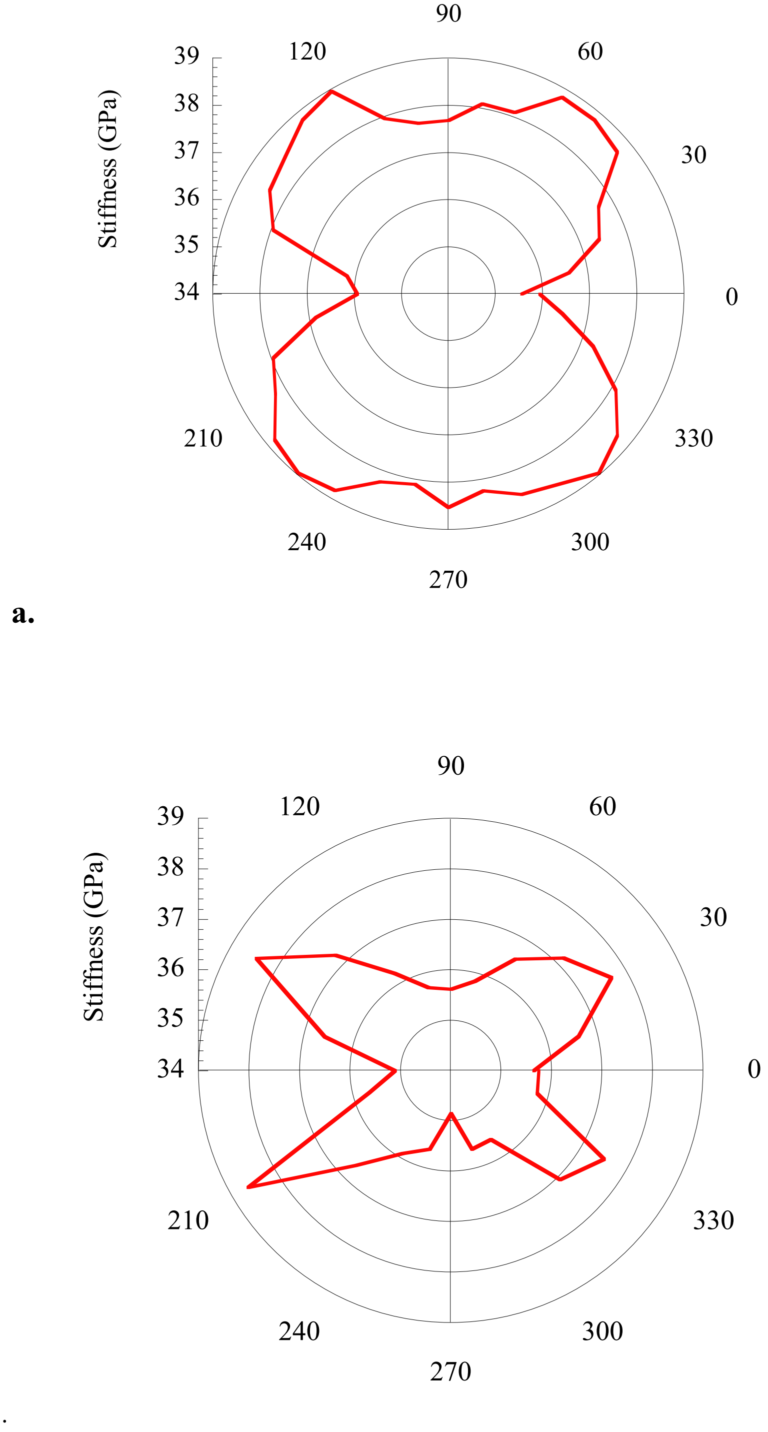

**Figure 32**: Stiffness plots for alpha-brass using data taken by (a) conical transducer (8.76% variation, 1.07% error) and (b) interferometer (9.77% variation, 0.27% error)

The same symmetrical accuracy was not seen in Cu70Zn30 (Figure 33), although some symmetry does occur and a slight rotation of this symmetry off the y-axis may be due to the sample not being cut exactly along the rolling direction. The alignment of the laser line to the sample relies on the sample being cut accurately along and perpendicular to the rolling direction. This off-center symmetry is an example of the sensitivity of our system to the entire sample preparation and experimental set-up.

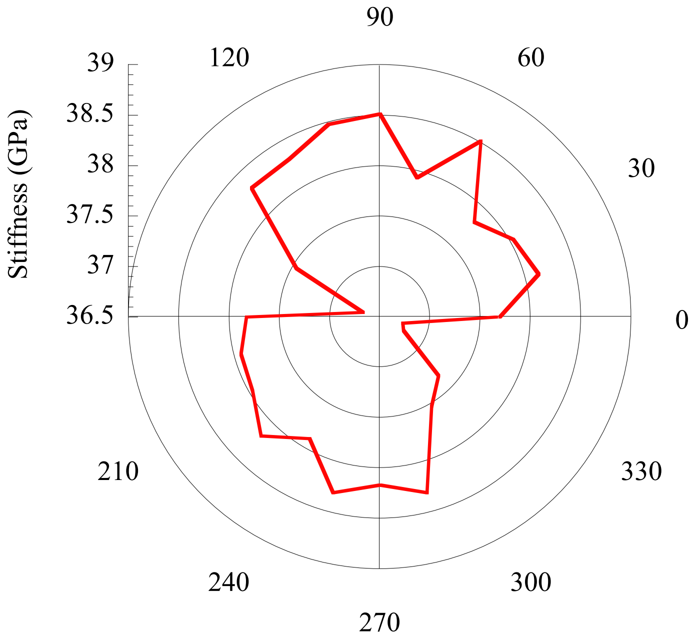

**Figure 33**: 70/30 rolled brass plate (sample 2) with 4.77% variation in stiffness and 0.088% error

### 3.4 Calculating the orientation distribution coefficients

To quantitatively describe the texture, we used the orientation distribution coefficients (ODCs) to give a value to the degree of anisotropy found in the material. Using the stiffnesses calculated from the ultrasonic velocity results, and stiffness values for single crystals, these ODCs can be calculated with simple algebra. The equations derived by Sayers (1982) can be rearranged to solve directly for the orientation distribution coefficients for a transversely isotropic material using data collected from a longitudinal wave propagating along the axis of symmetry in the z direction $C_{zz}$, and the shear waves propagating perpendicular to the axis of symmetry in the x direction $C_{xy}$ and $C_{xz}$ (Figure 34).

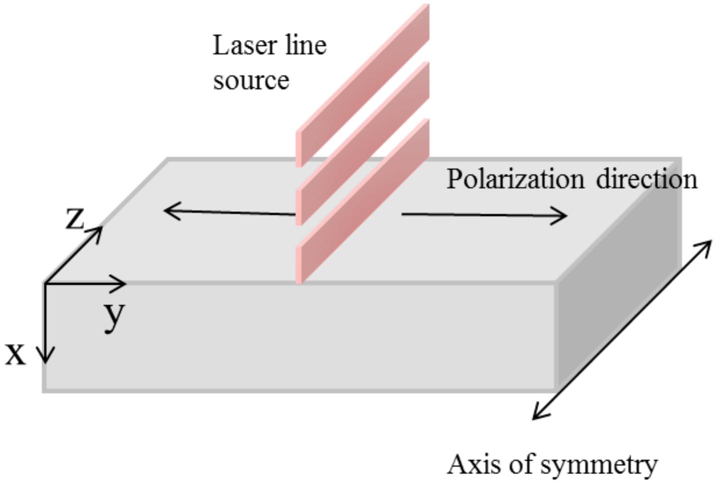

**Figure 34**: Wave propagation and polarization directions for a laser line source

$$C_{zz} = C_{11} - 2C(\tfrac{1}{5} - \tfrac{16}{35}\sqrt{2}\pi^2 W_{400}) \tag{44}$$

$$C_{xy} = C_{44} + C[\tfrac{1}{5} + \tfrac{4}{35}\sqrt{2}\pi^2 (W_{400} - \sqrt{70}W_{440})] \tag{45}$$

$$C_{xz} = C_{44} + C[\tfrac{1}{5} - \tfrac{16}{35}\sqrt{2}\pi^2 (W_{400} - \sqrt{\tfrac{5}{2}}W_{420})] \tag{46}$$

So that the orientation distribution coefficients are:

$$W_{400} = \frac{\left(\frac{C_{zz} - C_{11}}{2C}\right) + \frac{1}{5}}{\frac{16}{35}\sqrt{2}\pi^2} \tag{47}$$

$$W_{440} = \frac{\left[\left(\frac{\left(\frac{C_{44} - C_{xy}}{C}\right) + \frac{1}{5}}{\frac{4}{35}\sqrt{2}\pi^2}\right) + W_{400}\right]}{\sqrt{70}} \tag{48}$$

$$W_{420} = \frac{\left[\left(\frac{\left(\frac{C_{xz} - C_{44}}{C}\right) - \frac{1}{5}}{\frac{16}{35}\sqrt{2}\pi^2}\right) + W_{400}\right]}{\sqrt{\frac{5}{2}}} \tag{49}$$

Single cubic crystal elastic stiffnesses can be found in numerous texts. We are using values from Waterman (1959) in Table 4 with units for elastic stiffness constants in GPa. Substituting single crystal elastic stiffness values for $C_{11}$, $C_{12}$ and $C_{44}$ and the elastic stiffness data for $C_{zz}$, $C_{xy}$, and $C_{xz}$, we can solve for the orientation distribution coefficient $W_{400}$, and then use that coefficient to solve for $W_{440}$ and $W_{420}$ in equations 48 and 49.

**Table 4**: Single crystal elastic stiffnesses (GPa) and densities

| **Material** | **$C_{11}$** | **$C_{12}$** | **$C_{44}$** | **Density kg/m$^3$** |
|---|---|---|---|---|
| **Aluminum** | 108 | 62.2 | 28.4 | 2780 |
| **Copper** | 170 | 123 | 75.3 | 8940 |
| **α-Brass** | 147 | 111 | 72.0 | 8470 |

## 3.5 EBSD vs. ultrasound in determining the ODCs

Electron Backscatter Diffraction (EBSD) measurements were made on aluminum 2024, brass 64/36, and brass 70/30. Pole figure plots and inverse pole figure maps are shown for both brass samples below. Elastic stiffness matrices were generated using the Euler angles and areas of each grain. To do this calculation, Euler angles in Bunge notation were rotated so that the crystallite axis, XYZ, were aligned with the sample axis xyz (see Appendix A). Using Mathematica, upper and lower bounds were generated using the Voigt and Reuss averaging scheme respectively, and the Hill average was calculated from those schemes to give a stiffness matrix.

$$c_H = \tfrac{1}{2}(c_V + c_R) \tag{50}$$

With the matrix components $C_{11}$, $C_{22}$, $C_{44}$ and $C_{55}$, and the single crystal stiffness values (Table 4) the ODCs were calculated and are shown in Table 6.

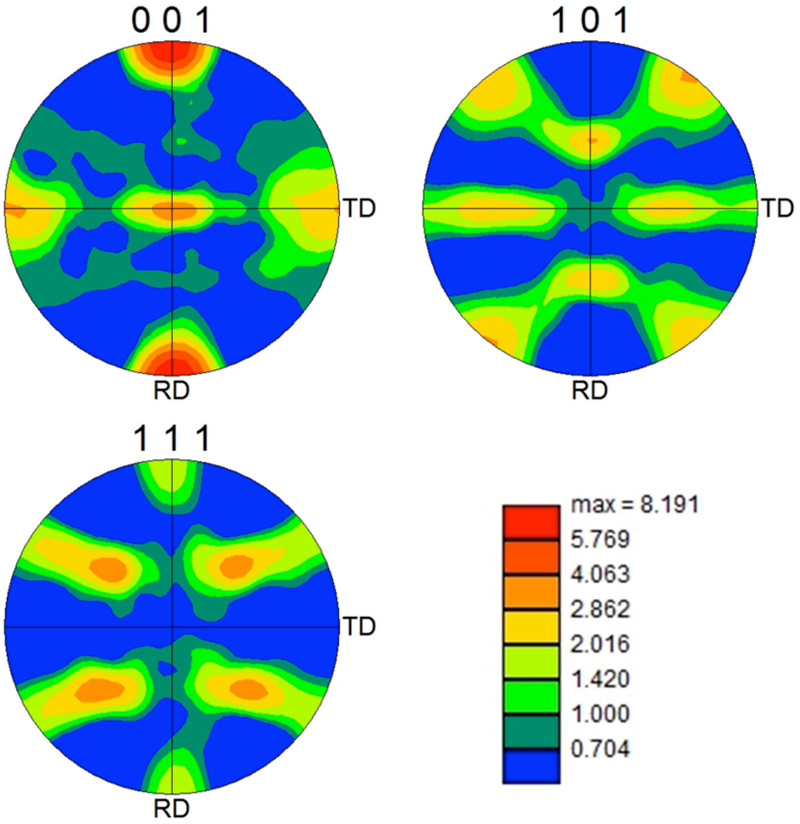

**Figure 35**: Pole figure plots for Brass 1 (64/36 composition)

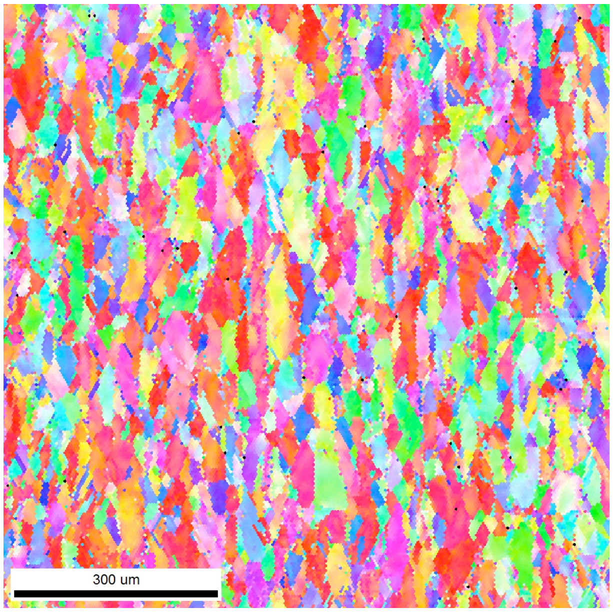

**Figure 36**: EBSD map showing orientation of grains for 64/36 brass

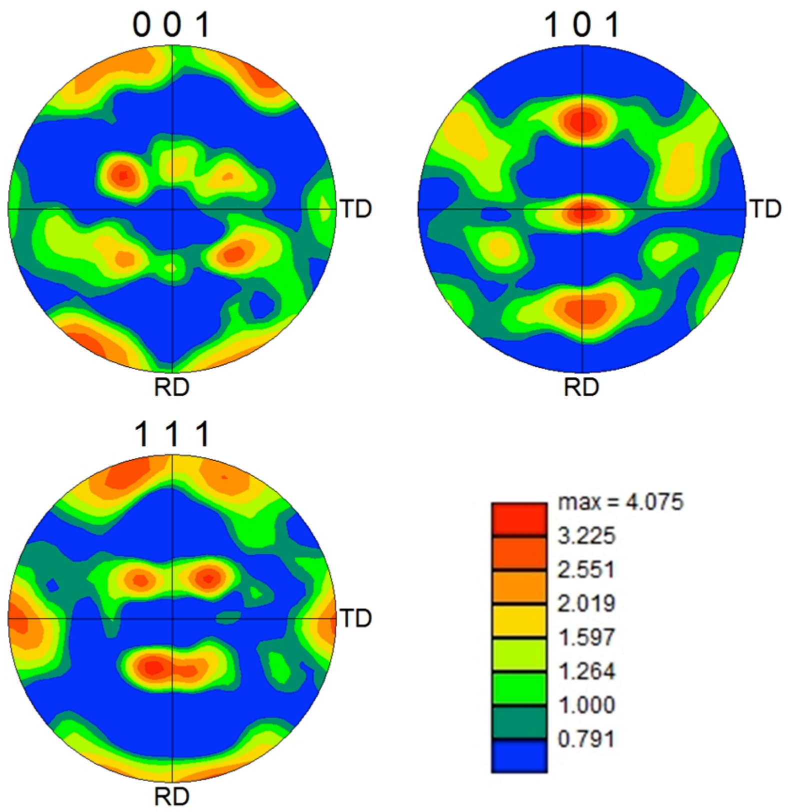

**Figure 37**: Pole figure plots for Brass 2 (70/30 composition)

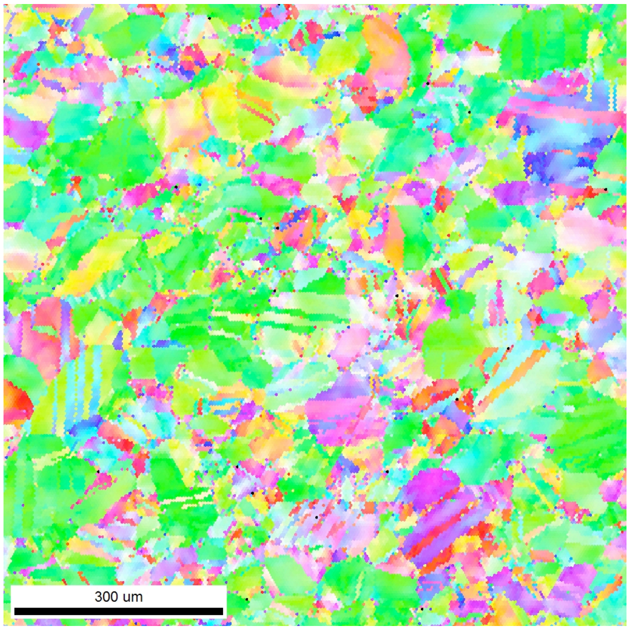

**Figure 38**: EBSD map showing orientation of grains for 70/30 brass

The ODC results from ultrasonic and EBSD measurements are tabulated below. The first thing to note is Brass 1 in both tables refers to the same sample. This is the only sample that was available for comparison in both the ultrasonic and EBSD experiments. The second thing to note are the values for the row labeled “Al single crystal”. Using the literature values presented in Table 4 as the $C_{zz}$, $C_{xz}$ and $C_{xz}$ components in equations 47, 48, and 49, $W_{420}$ becomes 0 and values for $W_{400}$ and $W_{440}$ are relatively large compared to the values for the tested alloys. Also be aware that using other single crystal values found for aluminum that deviate from those presented in Table 4 will yield much different results including +/- sign changes. We have now set up a neutral base to compare the experimental results.

For values of $C_{zz}$ below or close to $C_{11}$, $W_{400}$ will be positive. Values of $C_{zz}$ that are much greater than $C_{11}$, several GPa, will cause $W_{400}$ to turn negative. Out of all of the materials tested only Al 1 had a $C_{zz}$ that was lower than $C_{11}$ and this result pushes $W_{400}$ to be highest for any material. Having a very large $C_{zz}$ can also cause $W_{420}$ to become negative and $W_{440}$ to be positive. A very large $C_{zz}$ was never the case in any of the experiments so all $W_{400}$ are positive. Because $W_{400}$ is always positive, the signs for $W_{420}$ and $W_{440}$ depend on $C_{xz}$ or $C_{xy}$. For all cases $C_{xz}$ and $C_{xy}$ were always lower than the single crystal value for $C_{44}$. In addition, $C_{xz}$ was always greater than $C_{xy}$ except for the Al 4a and 4b case, showing that within reasonable parameters the ODCs are not necessarily dependent on which stiffness value is used. What they are most dependent on however is how close $C_{xz}$ and $C_{xy}$ are to approaching single crystal values. In each material with the exception of Al 8, values for $C_{xz}$ and $C_{xy}$ were several GPa below the single crystal value of $C_{44}$. However, in Al 8 those numbers approached $C_{44}$ to within 2

GPa causing a switch in +/- signs for $W_{420}$ and $W_{440}$. For $W_{420}$ and $W_{440}$ to both be positive, $C_{xz} = C_{xy}$. The aluminum sample in Table 6 comes very close causing $W_{440}$ to be nearly zero.

**Table 5**: Calculated orientation distribution coefficients from laser ultrasonic results

| **Material** | $W_{400}$ | $W_{420}$ | $W_{440}$ |
|---|---|---|---|
| **Al single crystal** | 0.0313 | 0 | 0.0187 |
| **Al 5 and Al 6** | 0.0174 | 0.0176 | -0.0098 |
| **Al 4a and Al 4b** | 0.0028 | 0.0084 | -0.0027 |
| **Al 1** | 0.0883 | 0.0688 | -0.0186 |
| **Al 8** | 0.0054 | -0.0011 | 0.0036 |
| **Brass 1** | **0.0282** | **0.0314** | **-0.0069** |
| **Copper 1** | 0.0268 | 0.0269 | -0.0057 |

**Table 6**: Orientation distribution coefficients calculated from EBSD results

| **Material** | $W_{400}$ | $W_{420}$ | $W_{440}$ |
|---|---|---|---|
| **Aluminum** | 0.0072 | 0.0021 | -0.0009 |
| **Brass 1** | **0.0180** | **0.0129** | **-0.0020** |
| **Brass 2** | 0.0084 | 0.0124 | -0.0068 |

From this analysis, given a table of ODCs for a material with no information on the elastic stiffnesses, it could be inferred that for values of $W_{420}$ and $W_{440}$ that both fall close to zero means the shear stiffnesses $C_{xz}$ and $C_{xy}$ are nearly the equal. For a change in sign such that $W_{420}$ is negative and $W_{440}$ is positive indicates that values for $C_{xz}$ and $C_{xy}$ are both approaching the single crystal value for $C_{44}$.

Comparing the Brass 1 results from ultrasound in Table 5 to EBSD in Table 6 shows that each coefficient carries the same sign but in general EBSD coefficients fall slightly closer to zero than those for ultrasound. Results from EBSD show the aluminum coefficients an order of magnitude smaller than the ultrasonic coefficients.

From the EBSD results we are also able to give a better interpretation of the differences seen in our ultrasonic results involving the two different brass samples. The EBSD orientation maps show large grains and twinning in the Brass 2 sample where the Brass 1 sample has a smaller distribution of grain sizes with a more obvious rolling direction. Going back to ultrasonic stiffness plots, Figure 32 and Figure 33, the symmetry observed for Brass 1 is much cleaner than that observed for Brass 2 because of the difficulty in interpreting the shear arrival, which now might be explained by these EBSD micrographs such that the larger grains in Brass 2 will increase the effect of scattering on the ultrasonic waves. Although we used EBSD to aid in the interpretation of this result, ultrasonics will still provide a faster through-thickness determination of material texture. To achieve the same results with EBSD, a thorough layer-by-layer destructive analysis would need to be performed.

### 3.6 Line source results on as-received clean nuclear grade graphite

From the model in section 2.2, calculated waveforms of an extruded material are shown in Figure 39 as a guide for the experimental waveforms to follow. Line source results have been gathered and normalized at 0- and 90-degree orientations with respect to the extruded or cast billet directions for graphite grades PCEA (Figure 40 and Figure 41), BAN (Figure 42 and Figure 43), IG-110 (Figure 44 and Figure 45), and NBG-18 (Figure 46 and Figure 47). We can see a strong dependence on longitudinal wave speed to orientation in the extruded specimens PCEA and BAN. The shear wave is more difficult to interpret without the use of a model.

In Figure 40, graphite grade PCEA is displayed to correspond to the model in Figure 39 showing the three possible arrival times for this extruded material. The transversely isotropic case can clearly be identified by the arrival of the longitudinal wave. The remaining two cases are more difficult to interpret because of scattering interference occurring around the time of the shear arrival. Using the model from section 2.2 to fit the data makes it possible to extract a shear arrival time and determine the orientation of the original billet.

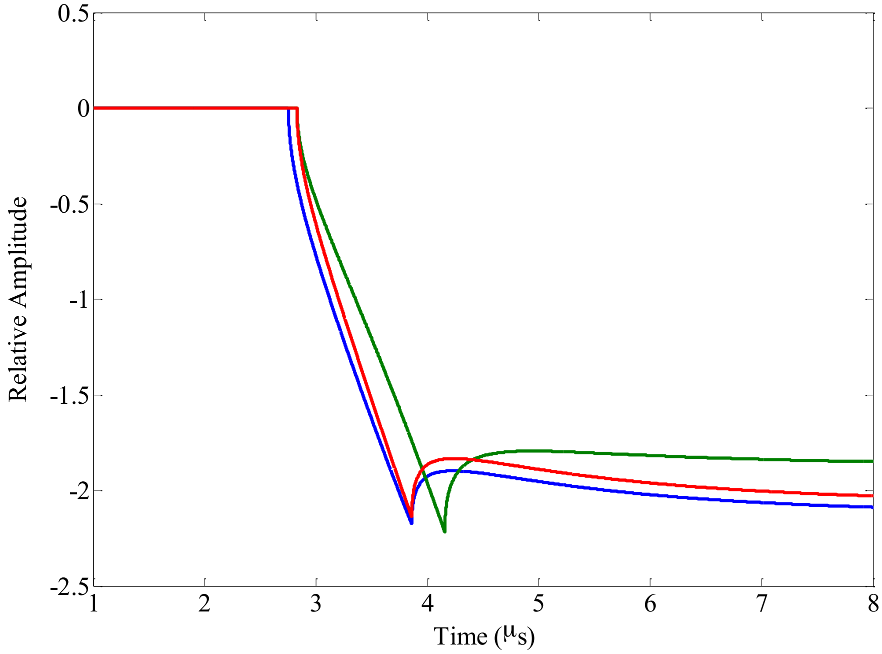

**Figure 39**: Line source model to fit graphite grade PCEA. Blue- Transversely isotropic: wave propagation along axis of symmetry, Green- Isotropic: laser line parallel to axis of symmetry, Red- Line perpendicular to axis of symmetry.

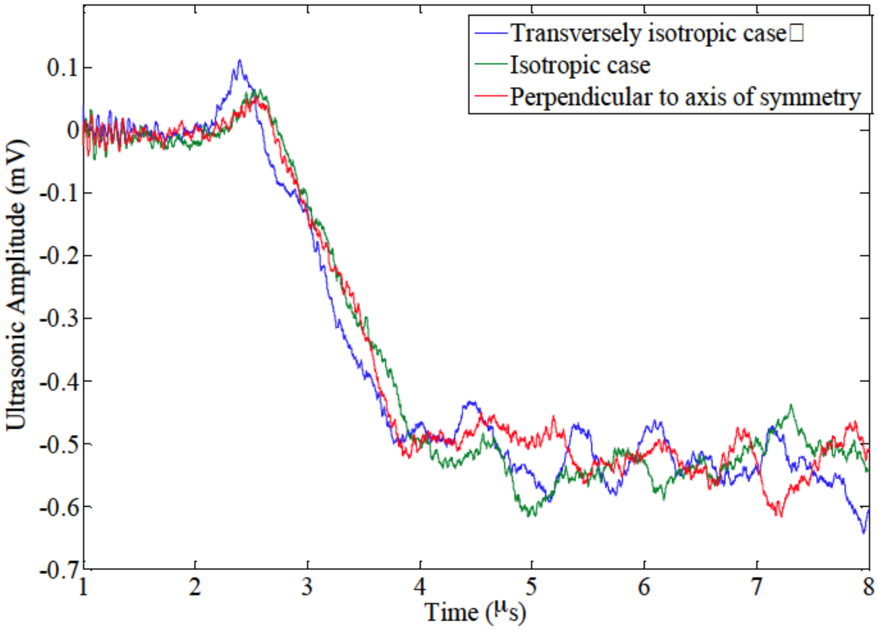

**Figure 40**: Data collected from extruded graphite grade PCEA shows the three different orientations of the billet.

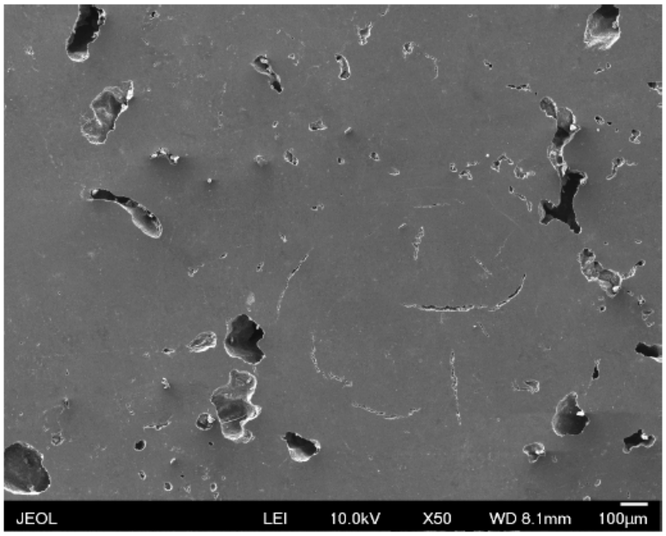

**Figure 41**: SEM micrograph of PCEA

The same analysis was used for graphite grade BAN shown in Figure 42 and Figure 43. Interpretation of BAN was aided in that the portion of the acquired billet was cylindrical instead of a cut block of unknown origin and orientation. Two specimens were cut from the cylinder, one perpendicular and one parallel to the extrusion direction.

Now, having known the orientation of extrusion prior to ultrasonic testing, the results can be verified to agree with the model as well as those results from PCEA and give an even more definitive example of qualification of the experimental method and interpretation.

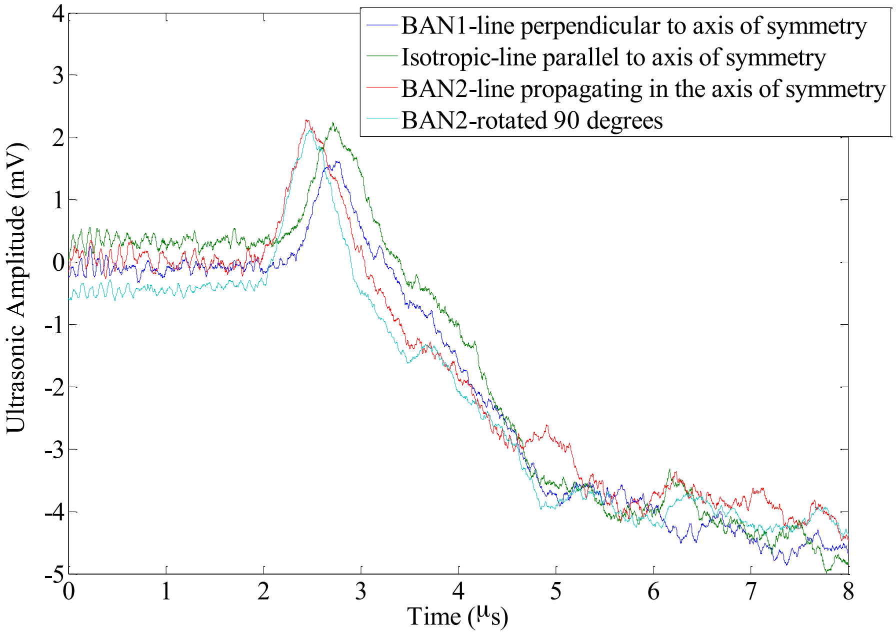

**Figure 42**: Two samples of graphite grade BAN cut parallel and perpendicular to the extruded direction of the billet. Each sample has two waveforms displayed showing results for orthogonal laser line orientations.

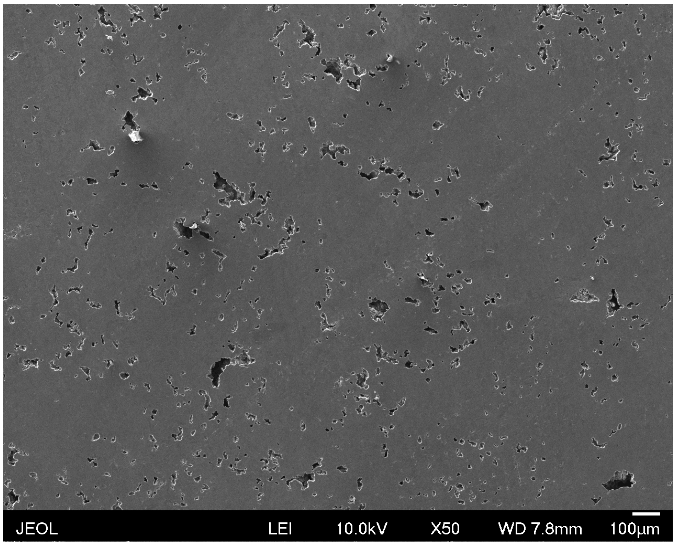

**Figure 43**: SEM micrograph of BAN

Graphite grade IG110 shown in Figure 44 is noted for having ultrafine grain and pore size (Figure 45). This has a direct effect on the ultrasonic data showing a smaller amplitude of scattered waves occurring around the shear arrival time compared to previous graphite grades that have a much larger grain size and large scattering amplitudes. The narrow longitudinal arrival is also an indicator of small grain and pore size. The smaller pores give the material a shorter effective skin depth allowing for enhancement of the ultrasonic signal. The longitudinal wave times-of-flight vary between samples 1 and 2 likely because the location from which the graphite block was cut from the original billet is unknown and there will be variation in density of material. This will be apparent in the vibramolded samples and we might interpret that the higher-density samples were likely cut from the side of the block closest to the central or lower portion of the original billet, yielding a faster time-of-arrival.

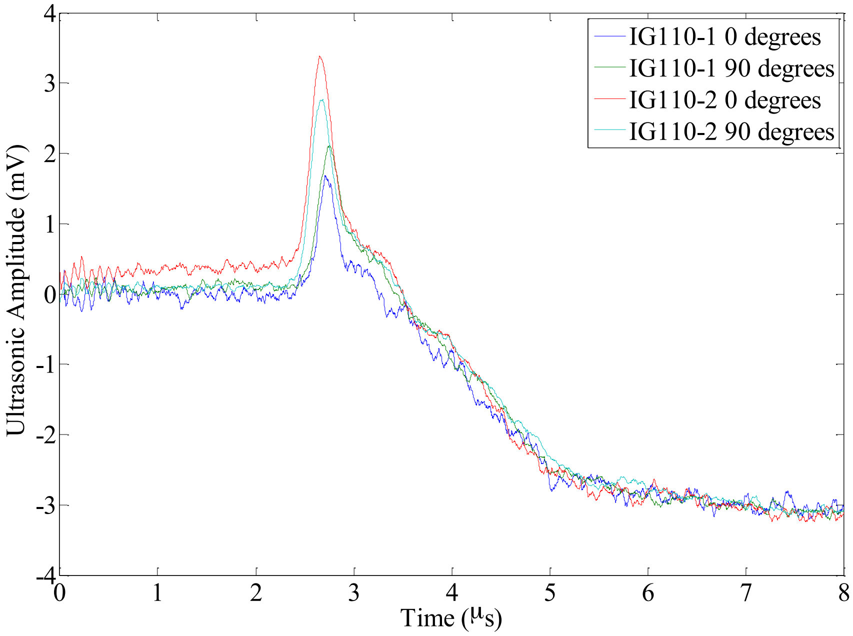

**Figure 44**: Two samples of vibramolded, ultrafine-grain graphite grade IG110. The samples were cut from different locations in the billet and results from orthogonal laser line orientations are shown for each.

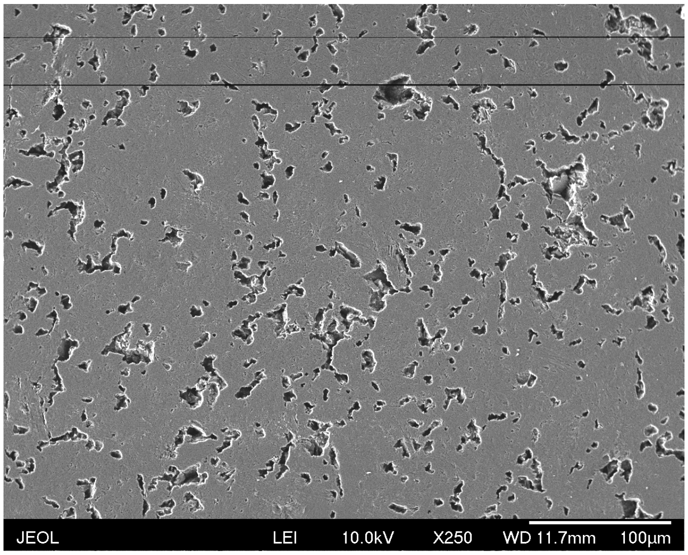

**Figure 45**: SEM micrograph of IG-110

Compare IG-110's longitudinal arrival with NBG-18 in Figure 46 and notice how this medium-grained material has a much broader longitudinal arrival. The results of NBG-18 also tell us that when inspecting a billet of vibramolded graphite, it may be critical to be aware of differences in ultrasound that are dependent on the location of data acquisition. Two samples of NBG-18 are displayed in Figure 46. One is taken from a portion of a billet sent directly by the manufacturer (SGL), although location of this block from the original billet is unknown. The second sample was cut from a block taken from the top of a billet (acquired from Oak Ridge National Laboratory). Although there could be discrepancy between waveforms of these two samples simply because they originate from two different billets, it is important to note that these differences could also be due to samples being made from extreme ends of a vibramolded billet. As seen with IG110, location of the cut sample can impact wavespeed.

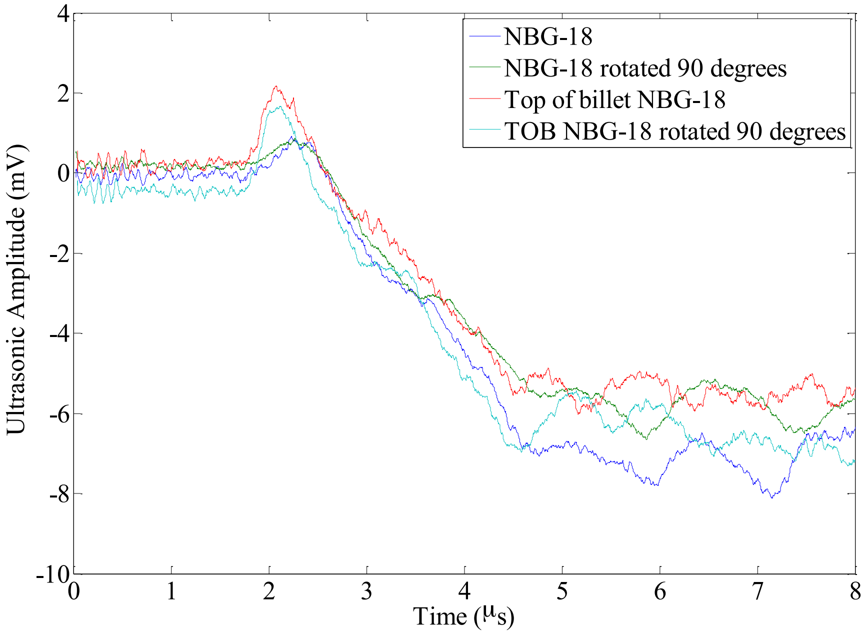

**Figure 46**: One sample each of vibramolded graphite grade NBG-18 taken from two different billets. Two waveforms for each sample are shown, generated by orthogonal laser line orientations.

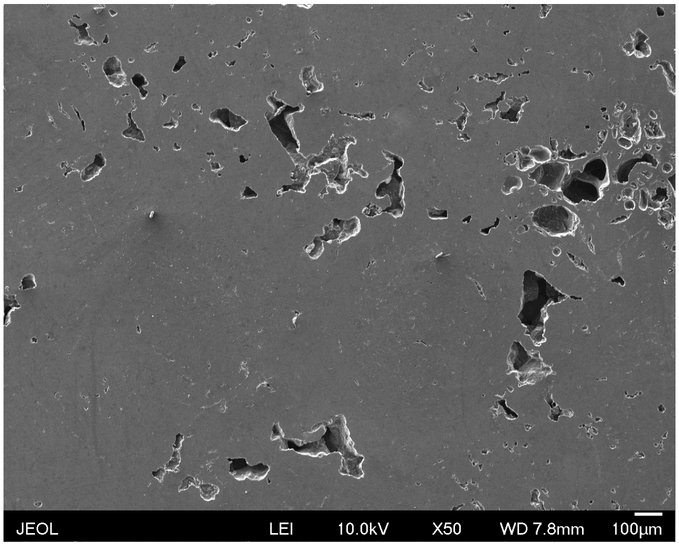

**Figure 47:** SEM micrograph of NBG-18

This chapter has described experimental results to match theory that polarized ultrasonic shear waves can be used to measure the texture of a material as well as characterize material systems like graphite. Orientation distribution coefficients have yet to be calculated for the graphite, however, the results prove anisotropic properties exist even though the system is normally considered to be isotropic. As discussed in section 2.3.3, the equations presented in this thesis are for FCC materials and calculating the ODCs for graphite will require equations for hexagonal crystallites. Further examination of the literature (Kielczynski & Busslère 1991) and a development of the orientation distribution function to calculate the ODCs for hexagonal crystals and specifically these graphite systems with no single crystal information available, will be up to future work. However, the importance of the current results and future work in quantifying the texture of these materials can be seen in the next chapter. We will show experimental results on fatigue damaged material that again show a dependence on the shear wave.

# 4 LASER ULTRASONICS TO DETECT FATIGUE DAMAGE

In the following experiments, ultrasound was generated in all samples by a 1064 nm pulse laser with a 10 ns pulse length and 10 Hz repetition rate. Low laser fluence is maintained throughout all experiments to generate ultrasound in the thermoelastic regime so no material is removed from the specimen surface and the temperature gradient is not severe enough to change the state of the material. In this thermoelastic regime, more energy is given to the shear component (Bernstein & Spicer 2000) giving us the ability to monitor changes in material properties using the well-defined characteristics of the shear component more efficiently than if we were to use the broader and sometimes unidentifiable longitudinal component.

For detection of ultrasound, a 1.5 MHz contacting conical transducer or a Michelson-type path-stabilized interferometer was used. Either detector was positioned opposite the generation laser to measure waves traveling in the through thickness direction of the specimens.

## 4.1 Laser point source generation to monitor fatigue damage in aluminum alloys

The first indication of acoustic birefringence in a fatigued material using laser ultrasonics was during three point bend of rolled aluminum plates. A shift was observed in the shear arrival as the lasers were scanned along the fatigued region of the plate. This initial test used an Instron mechanical testing system with a three point bend apparatus. The material used for these experiments included Aluminum 6061-T6, received with a mirror finish and cut into 3.5in x 0.7in x 0.125in bars, as well as aluminum 2024-T351, which was cut into the same bar size and polished to a mirror finish on one side. The samples were fatigued on a three-point bend fixture, with a 75lb load at 5Hz. Every 10,000 cycles, the fatigue process was interrupted and samples were evaluated with the laser ultrasonic system.

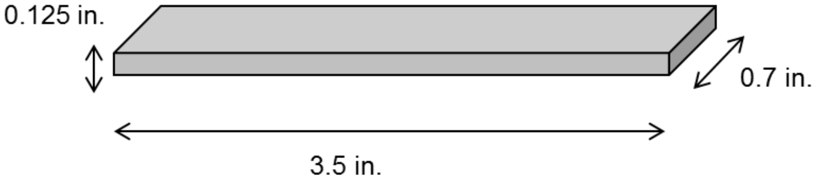

**Figure 48**: Dimensions of three-point bend aluminum specimens

**Figure 49**: Fixture used to conduct high cycle fatigue for aluminum samples using three points of contact with deflection in the center of the sample

To collect ultrasonic information localized to regions that are suspected to contain fatigue damage in our sample, the laser source and receiver were focused on epicenter to approximately 0.1 mm. The source and receiver were scanned across the sample to gather ultrasonic information as a function of position. Data were resolved at each location by averaging 500 wave forms for noise reduction. The sample was mounted on an xyz-translation stage so that the fatigued area could be easily scanned.

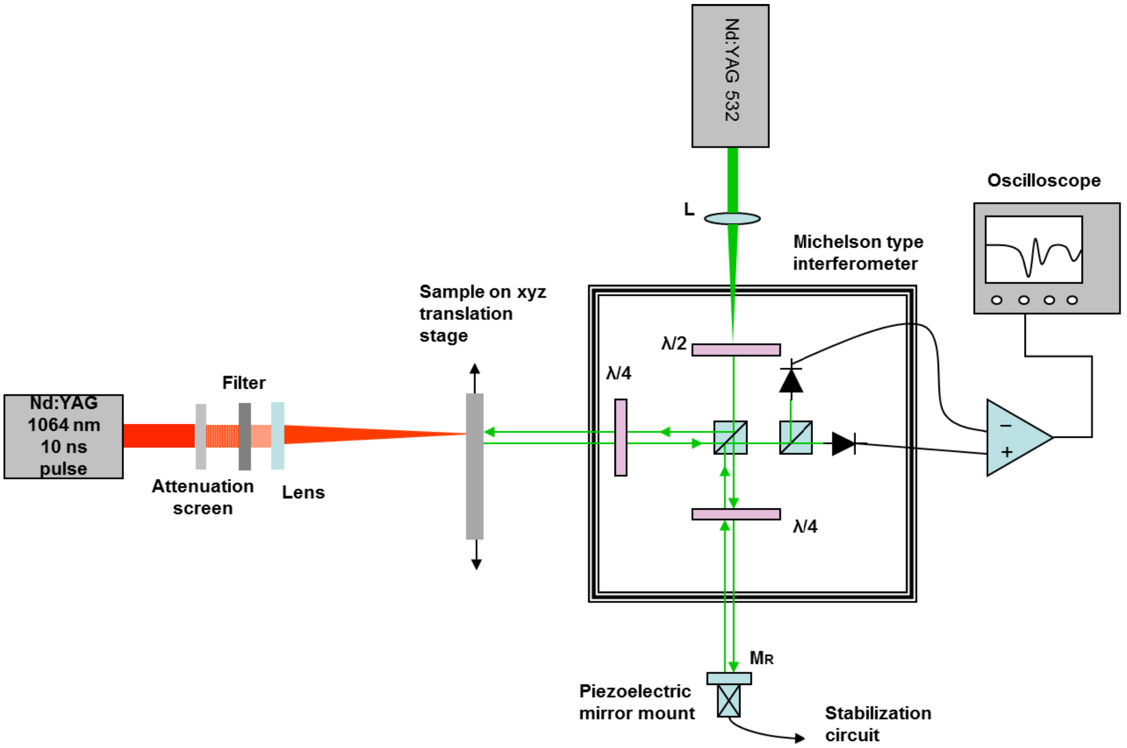

**Figure 50**: Experimental setup for lug joints using a pulsed laser for generation and a Michelson-type interferometer for detection

The next sample set were lug joint specimens modeled after an aircraft airframe component. Fabricated from aluminum alloy 2024-T351 these lugs are a version of a U-shaped test specimen with pin grips (Figure 51 and Figure 52). Before testing, one face of each lug joint was polished to a one micron surface finish (if an interferometer was used for detection) and evaluated in the expected stressed area with ultrasound. The fatigue testing schedule for the majority of specimens was a 100-1100 pound tension load, with a 10Hz cyclic fatigue rate and interruptions for specimen removal and ultrasonic testing every 10-20 kilocycles. While undergoing fatigue, the specimens failed at the interior shoulders. Due to material irregularities and the loading conditions of the fatiguing apparatus, occasionally only one shoulder exhibited signs of plastic deformation and ultimately failed.

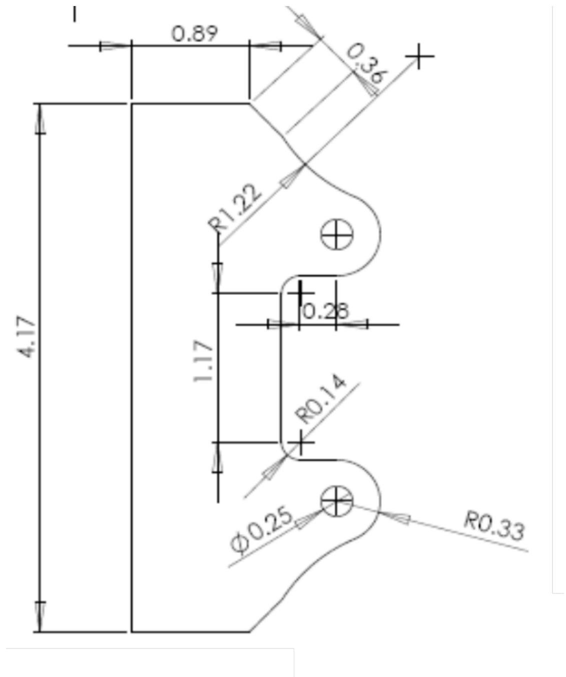

**Figure 51**: Lug joint dimensions (inches)

**Figure 52**: Fatigue fixture used for lug joints

Ultrasound was generated by either a 1064 nm pulsed Nd:YAG laser, or an 800 nm femtosecond pulsed laser, and focused to a 1 mm point source while still operating in the thermoelastic regime. The point source was focused on the lug joint in the area with the most concentrated fatigue damage, as identified by finite element modeling in Figure 53.

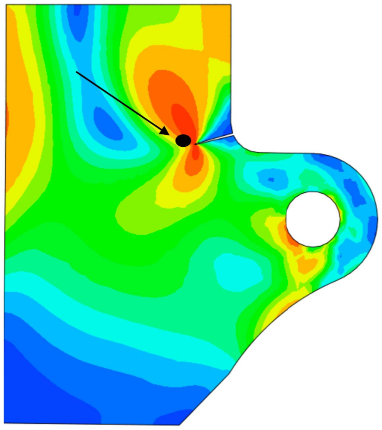

**Figure 53**: Stress concentration region of lug joint specimens indicating crack initiation at the interior shoulder during high cycle fatigue testing (Chattopadhyay 2008). Black spot indicates typical ultrasonic data acquisition.

Initial ultrasonic results were detected using the contacting transducer (Figure 54). The sample was mounted on an xyz-stage so that data acquisition points around the fatigue-damaged region could be easily repeated between fatigue states. To reduce noise, 500 waveforms were averaged for each data point. Figure 55 shows a photograph of the laser-in, transducer-out arrangement. To center the laser over the piezo sensor after the sample had been secured, longitudinal and shear waves were monitored continuously to identify the shortest arrival time for each wave.

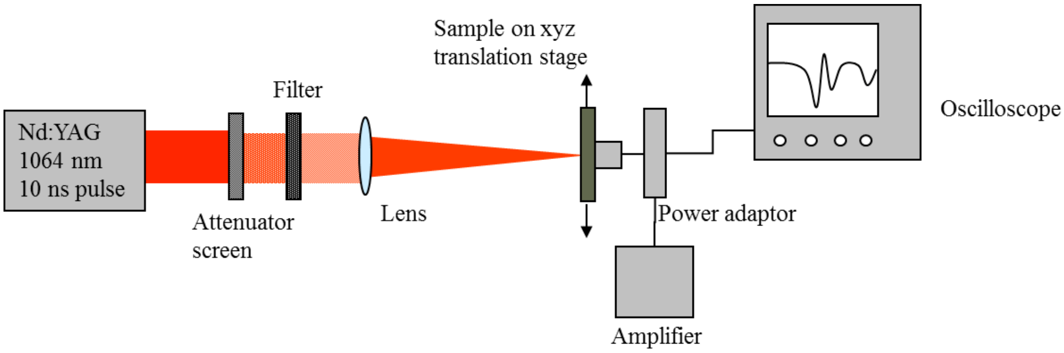

**Figure 54**: Experimental setup for lug joints using a pulsed laser for generation and a contacting transducer for detection.

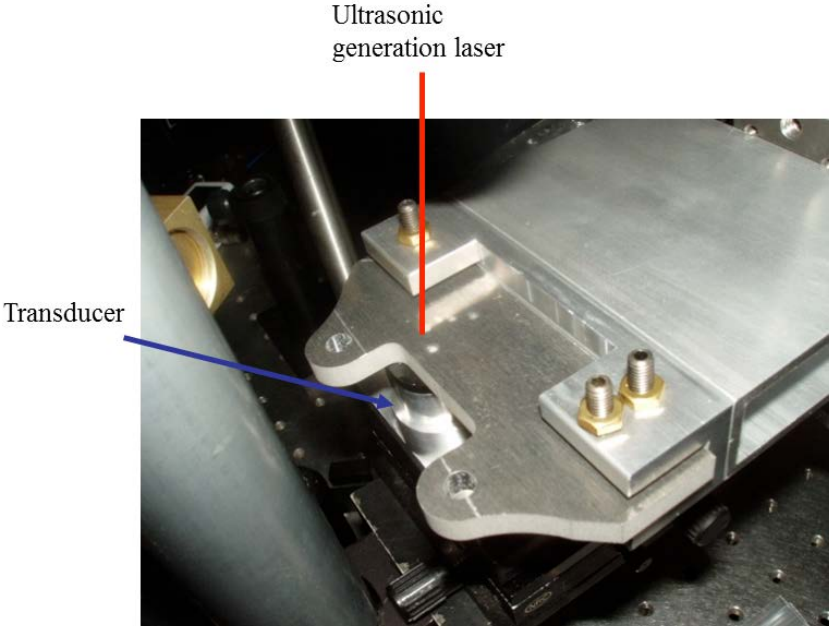

**Figure 55**: Photograph of the generation laser and transducer arrangement for ultrasonic testing of the lug joints.

Results on the data acquired by the transducer were difficult to interpret due to the limitations of a narrower frequency range, but were intriguing enough to warrant a more complex experiment using the interferometer instead for ultrasonic detection. For lug joints monitored using the interferometer, either the 1064 nm pulse laser or the 800 nm pulse laser was used for ultrasonic generation. In either case, as seen in Figure 50, the same interferometer was used for detection, focused directly opposite the laser point source.

## 4.2 Laser point source results on fatigue-damaged aluminum alloys

The most curious result from the three-point bend samples were comparing the as-received and fatigue damaged samples to Rose's model for an isotropic material shown previously. The model should closely follow the waveform for aluminum because aluminum is nearly isotropic. These data show that the as-received material has a greater variation in shape than the fatigue-damaged material. Since the model agrees more with the fatigue-damaged material, the aluminum is behaving more isotropically once further damage is induced post processing. Rolling induced anisotropy is no longer the main contributor to the material's texture.

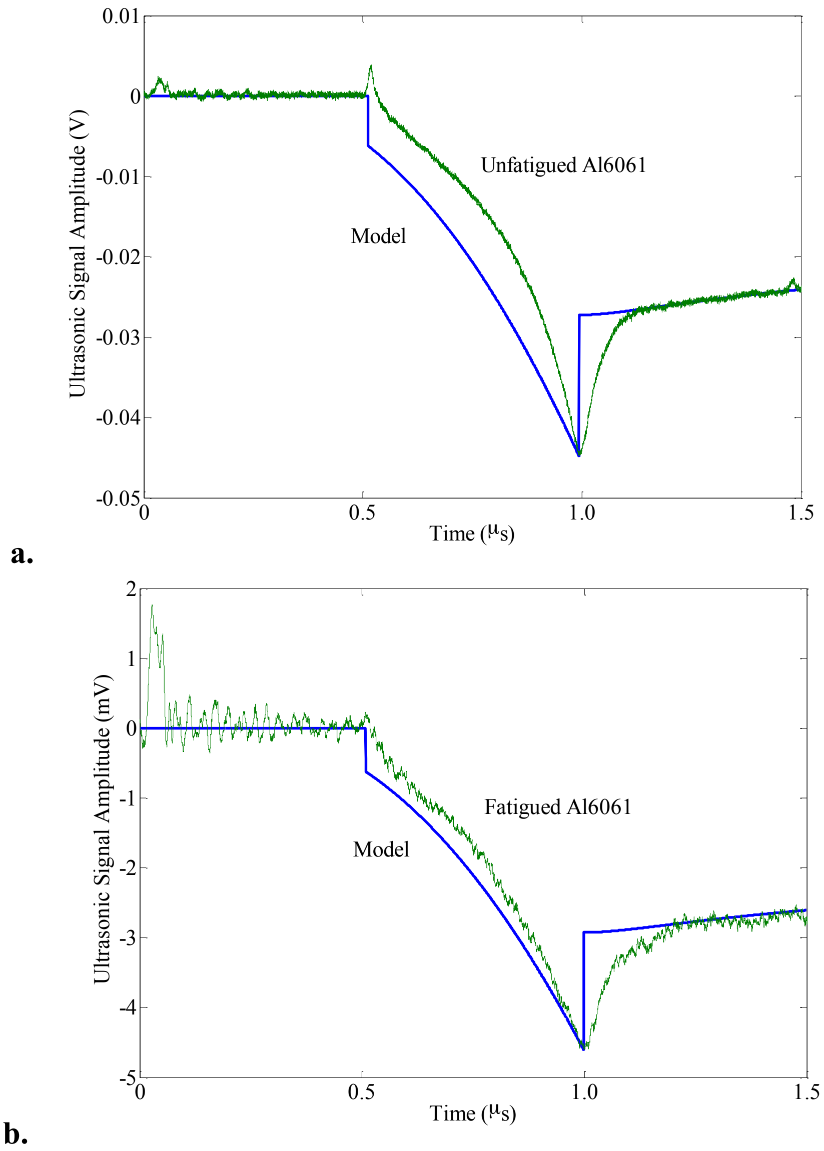

**Figure 56**: Point source results on **a.** unfatigued aluminum 6061 and **b**. fatigued aluminum 6061 compared to the point source model

Point source generation of ultrasound with detection by contacting transducer on the lug joints also indicates there is some sensitivity to the state of fatigue damage in aluminum alloy 2024. Lug joint number N2 was fatigued to 80,000 cycles with ultrasonic data taken every 20,000 cycles. In Figure 57, lug N2 displays a decrease in time-of-flight at 20,000 fatigue cycles, followed by a time-of-flight increase until 80,000 fatigue cycles when time-of-flight again decreases. Lug joint samples typically fail around 100,000-140,000 fatigue cycles; to measure a sudden change in N2 indicates the sample could be starting to show signs of microcracking.

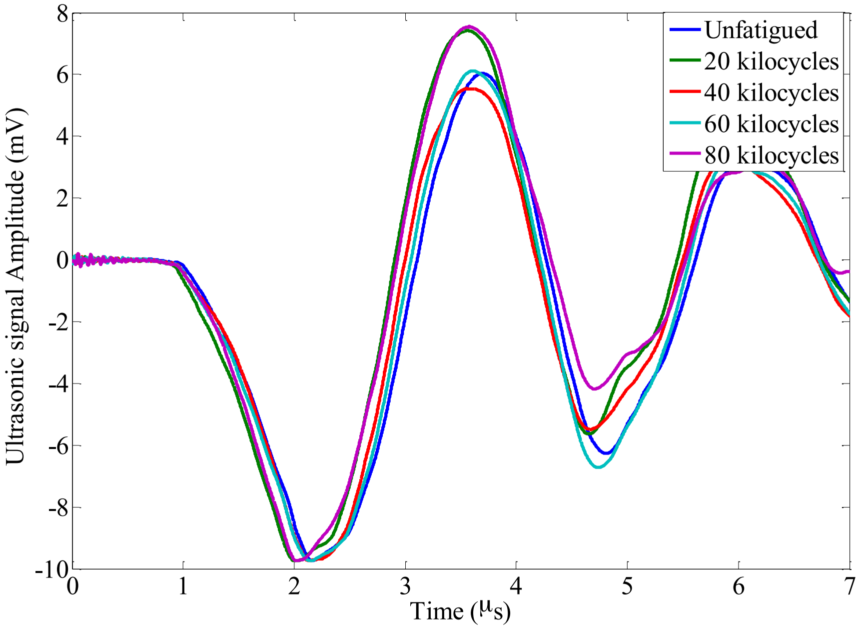

**Figure 57**: Lug joint N2, same position for all fatigue cycles for unfatigued to 80,000 fatigue cycles

Figure 58 displays the trend in fatigue damage versus velocity for a number of samples. In most cases, the lug joints follow the example of N2, with an initial increase in velocity and elastic stiffness, and a spike in velocity towards the end of the specimen life. At this time it is concluded that the increase in velocity at 20,000 fatigue cycles is due to the introduction of defects that change the effects of material processing defects, which cause a change in texture. This initial increase is followed by a relaxation over a few fatigue testing cycles. As the material continues to undergo fatigue damage, localized regions experience additional changes in texture causing the velocity and elastic stiffness to increase prior to failure. Aligned open microcracks will cause a decrease in velocity, as stated in section 2.3.2, and a material loaded in tension will experience the opening and closing of these microcracks continuously. During the fatigue life, if these microcracks coalesce into one primary crack, the crack tip radius will also affect the velocity and stiffness where large numbers of dislocations will cause the area to experience an increase in stiffness.

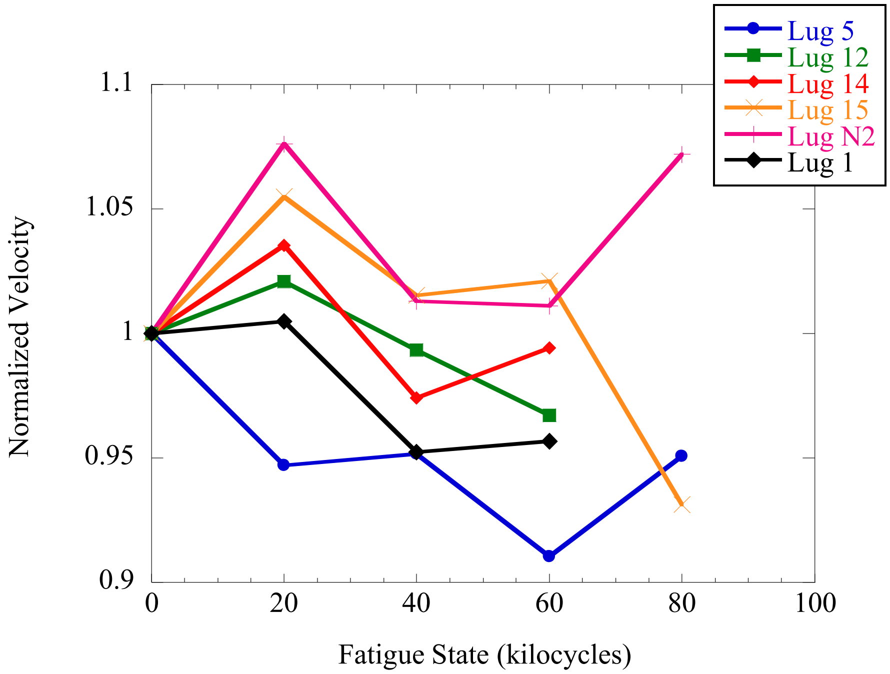

**Figure 58**: Series of lug joints, Al2024-T351, fatigued to near failure (60 or 80 kilocycles) with velocities normalized to one. Sample names as originally declared are indicated in the legend for reference.

Lug joint geometry is not ideal for our ultrasonic arrangement. Fatigue damage happens at the edge and that is not a location that can be interrogated because reflections off of the sample side will interfere with the direct through transmission waves. In addition to this side-wall interference, the exact location of crack initiation was not precisely predictable and while only one of the interior shoulders was monitored, that shoulder sometimes never exhibited any visible damage while the opposite shoulder would eventually be a point of failure. To increase the capabilities of the system to detect early fatigue damage, multiple locations around one shoulder were monitored. Locations used to collect ultrasonic data on lug joints are indicated in Figure 59.

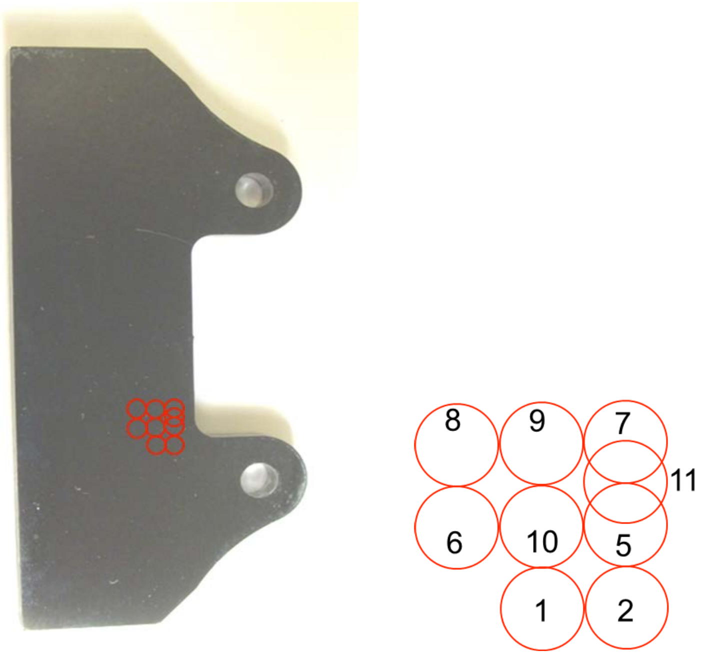

**Figure 59**: Data acquisition points on a lug joint around the fatigue-damaged region

Waveforms from these locations are shown together in Figure 60 and Figure 61 and are indicated by position number. The results in both figures are from lugs with visible surface cracking. For these cracked lugs, numbers 9 and 11, a shift in shear arrival is recorded at one or more position that is dependent on the crack tip and the localized region around the crack tip. Lug 11 has a short crack length of 2 mm and a noticeable shift in shear wave time-of-flight occurs at position 2, just below the end of the visible cracking region. Lug 9 displays the same behavior; however its crack length is 5 mm, and therefore position 6 shows the largest shift in time-of-flight. The data from both lugs indicate that these very localized regions are less stiff than the surrounding material matrix.

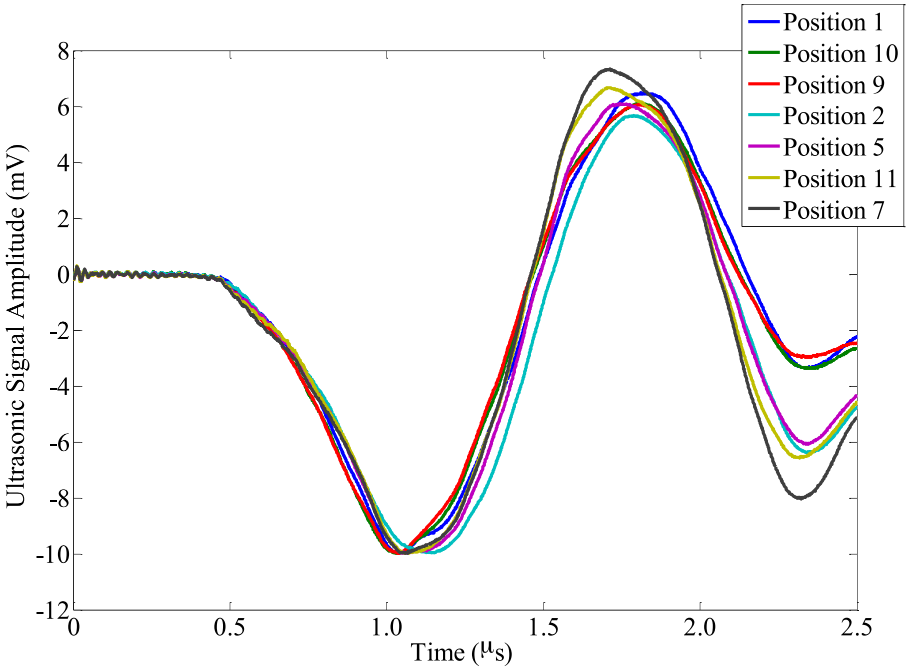

**Figure 60**: Data acquisition from positions shown in Figure 59 for a cracked lug joint (lug number 11). Lug joint 11 has a crack length of 2 mm.

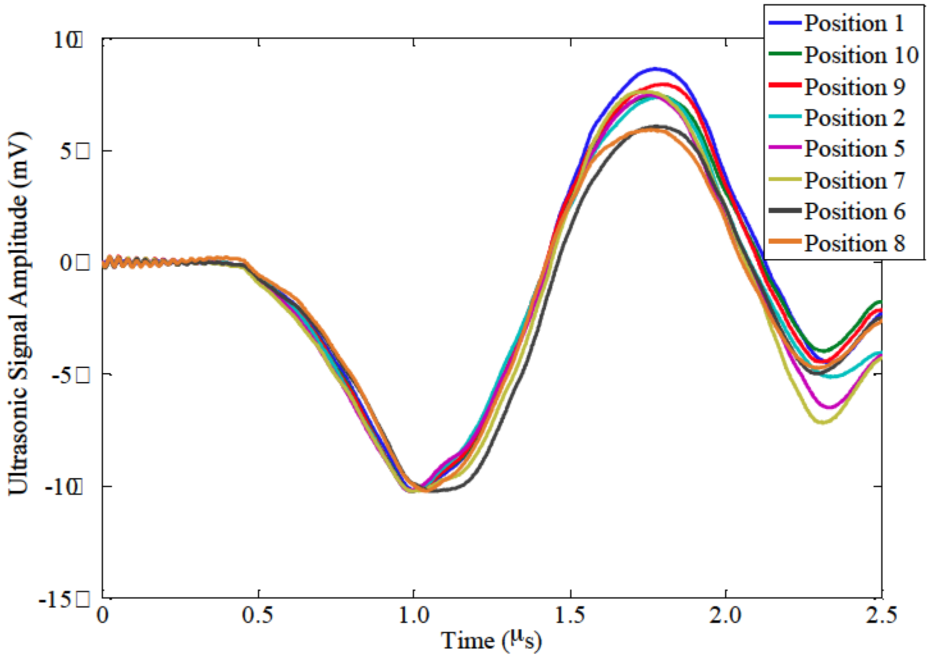

**Figure 61**: Data acquisition from positions shown in Figure 59 for a cracked lug joint (lug number 9). Lug joint 9 has a crack length of 5 mm.

For these experiments, the transducer was used as a means to generate large amounts of data very quickly. However, the recorded waveforms revealed some unusual characteristics of the transducer signal compared to what would be recorded using an interferometer. The longitudinal and shear arrival times are very broad, making analysis more challenging. Instead of using simple data analysis tools in graphing programs, the data often required additional review and a manual method had to be implemented for determining wave arrivals. The unusual waveforms directed us back to a non-contacting approach and once results using the transducer indicated a dependency on stiffness to fatigue damage, a transition to interferometric detection was decided as a next step. Over thirty additional lugs were fatigued and tested with the laser-in, laser-out point source method. However no discernible differences in wave forms regardless of fatigue state were found. Occasionally while fatigue testing, the lug joint would only fail at one end and as an attempt to save samples and time, a notch was cut into one shoulder of several samples to be certain fatigue damage would accelerate at the desired side of ultrasonic interrogation.  This still failed to yield any evidence of fatigue damage by interferometric detection, so it is concluded that the lug joint geometry is not an ideal candidate for laser ultrasonic characterization as has been investigated in this thesis.

A number of factors could be changed to achieve ideal results when looking for fatigue using either laser point or line source. Geometry will always be an issue for a chance of success in fatigue detection using the point and line source methods presented, and sample shape and size should continue to be changed.  While the methods presented in this thesis are not the only laser ultrasonic arrangements possible, they have been thoroughly analyzed and should be transitioned into other sample systems.

# 5 CONCLUSIONS

We have characterized several material systems using polarized ultrasonic shear waves exposing the stiffness variations in the as-received or post process state. In some systems we had access to orthogonal directions from the bulk material allowing us to calculate the orientation distribution coefficients, giving us a way to quantify the texture and compare results between samples of the same origin. Therefore, the work in this thesis has led us to the conclusion that laser ultrasonics can measure texture in materials in a more economical way than traditional texture analysis techniques. Ultrasound can give an average texture result that includes the bulk of the material, whereas surface scanning techniques like XRD and EBSD must look at multiple layers to describe the structure of the material's bulk. Conducting ultrasonic testing using a laser line source and interferometer to calculate the ODCs has not been studied until now, and references for the comparison between other ultrasonic methods and EBSD for generating the ODCs are minimal with several papers coming out of a single research group (Palmer *et al.* 2008; Essex *et al.* 2007; Essex *et al.* 2008; Davis *et al.* 2008).

Our results also show that fatigue damage in aluminum alloys has an impact on bulk material properties that can cause variation in ultrasonic results. This variation is enough that fatigue damage should be taken into consideration when characterizing the initial state of a material and throughout the monitoring of a material's lifetime well before visible cracking would occur. Velocity changes because of dislocation density and aligned microcracking. These might be distinguished such that phase velocity increases and group velocity decreases with dislocation density (Maurel *et al.* 2009; Min *et al.* 2005), and velocity decreases in the presence of aligned microcracking (Sayers &

Kachanov 1995). Both effects can be measured by the ODC, but the ODC for cracking is an actual measurement of crack content. An increase in measured velocity could mean an increase in dislocation density and a velocity decrease could be interpreted as a high concentration of aligned microcracks however both effects could be present during material fatigue.

Continuing studies on fatigue-damaged specimens should give a more definitive timeframe for when damage is likely to be detected. At this state in the research, changes in ultrasonic properties have been seen as early as twenty percent of the specimen lifetime with a clear indication of material failure could be determined as early as sixty-percent of lifetime as seen in the lug joint testing from section 4.2 and Figure 58. Future work on calculating texture in the fatigue-damaged materials would be more beneficial for structural health monitoring, and would quantify results so that standards could be put in place for earlier detection of material failure.

# REFERENCES

Achenbach, J.D., Sotiropoulos, D.A., Zhang, Ch. (1989). Effects of near-tip inhomogeneities on scattering of ultrasonic waves by cracks. *Metallurgical Transactions A*, 20A, 619-626.

Alers, G.A. & Liu, Y.C. (1966). Calculation of elastic anisotropy in rolled sheet. *Transactions of the Metallurgical Society of AIME*, 236, 482-489.

Anderson, A.J., Thompson, R.B., Bolingbroke, R., Root, J.H. (1996). Ultrasonic characterization of rolling and recrystallization textures in aluminum. *Textures and Microstructures*, 26-27, 39-58.

Aussel, J.D., Le Brun, A., Baboux, J.C. (1988). Generating acoustic waves by laser: theoretical and experimental study of the emission source. *Ultrasonics*, 26, 245-255.

Bernstein, J.R. & Spicer, J.B. (2000). Line source representation for laser-generated ultrasound in aluminum. *Journal of the Acoustical Society of America*, 107(3), 1352-1357.

Bunge, H.J. (1982). *Texture Analysis in Materials Science*. London: Butterworth & Co.

Burchell, T., Bratton, R., Windes, W. (2007). NGNP graphite selection and acquisition strategy (ORNL/TM-2007/153). Materials Science and Technology Division. Oak Ridge National Laboratory. Oak Ridge, TN.

Cantrell, J.H. & Yost, W.T. (2001). Nonlinear ultrasonic characterization of fatigue microstructures. *International Journal of Fatigue*, 23, S487.

Chattopadhyay, A. P.I. (2008). A Multidisciplinary Approach to Structural Health Monitoring and Prognosis of Metallic Aerospace Systems. *AFOSR performance report*, 38

Clarebrough, L.M. & Hargreaves, M.E. (1959). Work Hardening of Metals. *Progress in Metal Physics*, 8, 1-103.

Crampin, S. (1981). A review of wave motion in anisotropic and cracked elastic-media. *Wave Motion*, 3, 343-391.

Crampin, S. & Peacock, S. (2005). A review of shear-wave splitting in the compliant crack-critical anisotropic Earth. *Wave Motion*, 41, 59-77.

Crampin, S., Gao, Y., Peacock, S. (2008). Stress-forecasting (not predicting) earthquakes: A paradigm shift? *The Geological Society of Am*erica, 36(5), 427-430.

Davis, C.L., Strangwood, M., Potter, M., Dixon, S., Morris, P.F. (2008). Prediction of elastic modulus + anisotropy using x-ray and electron backscattered diffraction texture quantification and ultrasonic (electromagnetic acoustic transducer) measurements in aluminum sheets. *Metallurgical and Materials Transactions A*, 39A, 679-687.

Department of Energy, Office of Nuclear Energy (April 2010). Next generation nuclear plant report to congress.

Department of Transportation, Federal Aviation Administration. (2010). Ageing airplane program: widespread fatigue damage. *Federal Register*, 75(219).

Dixon, S., Fletcher, M.P., Rowlands, G. (2008). The accuracy of acoustic birefringence shear wave measurements in sheet metal. *Journal of Applied Physics*, 104(11), 114901-5.

Dutton, R. & Dewhurst, R.J. (2007). Graphite anisotropy measurements using laser-generated ultrasound. *Journal of Optics A: Pure and Applied Optics*, 9, S7-S11.

Essex, S.D., Potter, M.D.G., Dixon, S. (2007). Ultrasonic characterization of texture in rolled aluminum correlated with electron backscatter diffraction measurements. *American Institute of Physics Conference Proceedings,* 894, 1237-1244.

Essex, S.D., Potter, M.D.G., Dobedoe, R.S., Dixon, S. (2008). Ultrasonic characterization of effective elastic constants and texture in aluminum correlated with EBSD. *American Institute of Physics Conference Proceedings,* 975, 1176-1183.

Essex, S.D. (2009). Ultrasonic characterization of rolled aluminum and steel sheet correlated with electron backscatter diffraction measurements. PhD thesis, University of Warwick.

Foster, K., Fairburn, S.L., Leisure, R.G., Kim, S., Balzar, D., Alers, G., Ledbetter, H. (1999). Acoustic study of texture in polycrystalline brass. *Journal of the Acoustical Society of America*, 105(5), 2663-2668.

Garoi, F., Apostol, D., Damian, V., Schiopu, P. (2010). Traceable vibration amplitude measurement with a laser interferometer. *Romanian Journal of Physics*, 55(3-4), 369-375.

Granato, A. & Lücke, K. (1956)A. Theory of mechanical damping due to dislocations. *Journal of Applied Physics*, 27(6), 583-593.

Granato, A. & Lücke, K. (1956)B. Application of dislocation theory to internal friction phenomena at high frequencies. *Journal of Applied Physics*, 27(7), 789-805.

Gross, D. & Zhang, C. (1992). Wave propagation in damaged solids. *International Journal of Solids and Structures*, 29(14-15), 1763-1779.

Hertzberg, R.W. (1996). *Deformation and fracture mechanics of engineering materials*, John Wiley & Sons, Inc.

Hikata, A., Chick, B., Elbaum, C., Truell, R. (1962). Ultrasonic attenuation and velocity data on aluminum single crystals as a function of deformation and orientation. *Acta Metallurgica*, 10, 423-429.

Hikata, A., Chick, B.B., Elbaum, C. (1965). Dislocation contribution to the second harmonic generation of ultrasonic waves. *Journal of Applied Physics*, 36(1), 229-236.

Hurley, D.H. & Spicer, J.B. (1999). An investigation of the effects of material anisotropy and heterogeneity on pulsed, laser-generated acoustic signals. *IEEE Transactions on Ultrasonics, Ferroelectrics and Frequency Control*, 46(6), 1387-1395.

Hurley, D.H. (1998). An investigation of the anisotropic and heterogeneous nature of laser generated ultrasound in carbon-fiber-reinforced epoxy and single crystal materials. The Johns Hopkins University, ProQuest, UMI Dissertation Publishing, 9821137.

Hutchins, D.A., Dewhurst, R.J., Palmer, S.B. (1981). Directivity patterns of laser-generated ultrasound in aluminum. *Journal of the Acoustical Society of America*, 70(5), 1362-1369.

Joshi, N.R. & Green, R.E. (1972). Ultrasonic detection of fatigue damage. *Engineering Fracture Mechanics*, 4, 577-583.

Kawashima, K. (1990). Nondestructive characterization of texture and plastic strain ratio of metal sheets with electromagnetic acoustic transducers, *Journal of the Acoustical Society of America*, 87(2), 681-690.

Kenderian, S., Berndt, T., Green, R., Djordjevic, B. (2003). Ultrasonic monitoring of dislocations during fatigue of pearlitic rail steel, *Materials Science and Engineering*, A348, 90-99.

Kielczynski, P.J. and Busslère, J.F. (1991). Characterization of texture in hexagonal materials using a line focus acoustic microscope, IEEE Ultrasonics Symposium, pp. 1009-1013.

Kushch, V.I., Sevostianov, I., Mishnaevsky Jr., L. (2009). Effect of crack orientation statistics on effective stiffness of microcracked solid, *International Journal of Solids and Structures*, 46, 1574-1588.

Li, D.Y. & Szpunar, J.A. (1992). Determination of single crystal elastic constants from the measurement of ultrasonic velocity in the polycrystalline material, *Acta Metallurgica et Materialia.* 40(12), 3277-3283.

Main, I.G. (1993). *Vibrations and Waves in Physics*. Cambridge: Cambridge University Press.

Mauge, C. & Kachanov, M. (1994). Effective elastic properties of an anisotropic material with arbitrarily oriented interacting cracks, *Journal of the Mechanics and Physics of Solids*, 42(4), 561-584.

Maurel, A., Pagneux, V., Barra, F., Lund, F. (2009). Ultrasound as a probe of plasticity? The interaction of elastic waves with dislocations, *International Journal of Bifurcation and Chaos*, 19(8), 2765-2781.

McKie, A.D.W., Wagner, J.W., Spicer, J.B., Deaton, J.B. (1991). Dual-beam interferometer for the accurate determination of surface-wave velocity, *Applied Optics*, 30(28), 4034-4039.

Min, X., Kato, H., Yin, F., Konuma, S. (2005). Change in ultrasonic parameters and dislocation structures during fatigue process of aluminum alloy under high stress amplitude, *Materials Transactions*, 46(6), 1360-1367.

Moreau, A., Lévesque, D., Lord, M., Dubois, M., Monchalin, J.P., Padioleau, C., Bussière, J.F. (2002). On-line measurement of texture, thickness and plastic strain ratio using laser-ultrasound resonance spectroscopy, *Ultrasonics*, 40, 1047-1056.

Mujica, N., Cerda, M.T., Espinoza, R., Lisoni, J., Lund, F. (2012). Ultrasound as a probe of dislocation density in aluminum, *Acta Materialia*, 60(16), 5828-5837.

Musgrave, M.J.P. (1970) *Crystal Acoustics: Introduction to the study of elastic waves and vibrations in crystals*. San Francisco: Holden-Day, Inc.

Nagy, P.B. (1998). Fatigue damage assessment by nonlinear ultrasonic materials characterization, *Ultrasonics*, 36, 375-381.

Nye, J.F. (1972) *Physical Properties of Crystals*. London: Oxford University Press.

O'Brien, M.H., Telschow, K.L., Knibloe, J.R. (1992) Analysis of as-machined nuclear graphite parts using conventional and laser ultrasonic techniques, *Journal of Nuclear Science and Technology*, 29(4), 378-387.

Ogi, H., Hirao, M., Minoura, K. (1997). Noncontact measurement of ultrasonic attenuation during rotating fatigue test of steel, *Journal of Applied Physics*, 81(8), 3677-3684.

Oruganti, R.K., Sivaramanivas, R., Karthik, T.N., Kommareddy, V., Ramadurai, B., Ganesan, B., Nieters, E.K., Gigliotti, M.F., Keller, M.E., Shyamsunder, M.T., (2007). Quantification of fatigue damage accumulation using non-linear ultrasound measurements, *International Journal of Fatigue*, 29, 2032-2039.

Palmer, S.B., Essex, S., Potter, M.D.G., Dixon, S. (2008). Determination of crystallographic texture in metal sheets using ultrasound and EBSD, *SPIE*, 6934, 69340F.

Pan, Y., Rossignol, C., Audoin, B. (2003). Acoustic waves generated by a laser line pulse in a transversely isotropic cylinder, *Applied Physics Letters*, 82, (24), 4379-4381.

Papadakis, E.P. (1971). Elastic wave velocities in various alloy strips, *Metallurgical Transactions*, 2, 575-578.

Payton, R.G., (1983). *Elastic wave propagation in transversely isotropic media*. The Hague, Netherlands: Martinus Nijhoff Publishers.

Proctor, T.M. (1982). An improved piezoelectric acoustic emission transducer, *Journal of the Acoustical Society of America*, 71(5), 1163-1168.

Pruell, C., Kim, JY., Qu, J., Jacobs, L.J. (2009). Evaluation of fatigue damage using nonlinear guided waves, *Smart Materials and Structures*, 18(035003), 1-7.

Pursey, H. & Cox, H.L. (1954). The correction of elasticity measurements on slightly anisotropic materials, *Philosophical Magazine*, 45(362), 295-305.

Rao, K.T.V. & Ritchie, R.O. (1992). Fatigue of aluminum-lithium alloys, *International Materials Reviews*, 37(4), 153-185.

Ravenscroft, F.A., Newton, K., Scruby, C.B. (1991). Diffraction of ultrasound by crack: comparison of experiment with theory, *Ultrasonics*, 29, 29-37.

Roe, J.R. (1965). Description of crystallite orientation in polycrystalline materials. III. General solution to pole figure inversion, *Journal of Applied Physics*, 36(6), 2024-2031.

Rose, L.R.F. (1984). Point source representation for laser-generated ultrasound, *Journal of the Acoustical Society of America,* 75(3), 723-732.

Roux, J. (1990). Elastic wave propagation in anisotropic materials, *IEEE Ultrasonics Symposium*, 1065-1073.

Sayers, C.M. (1982). Ultrasonic velocities in anisotropic polycrystalline aggregates, *Journal of Physics D: Applied Physics*, 15, 2157-2167.

Sayers, C.M. (1988). Stress-induced ultrasonic wave velocity anisotropy in fractured rock, *Ultrasonics*, 26, 311-317.

Sayers, C.M. & Kachanov, M. (1995). Microcrack-induced elastic wave anisotropy of brittle rocks, *Journal of Geophysical Research*, 100(B3), 4149-4156.

Scruby, C.B., Smith, R.L., Moss, B.C. (1986). Microstructural monitoring by laser-ultrasonic attenuation and forward scattering, *NDT International*, 19(5), 307-313.

Scruby, C.B. & Drain, L.E. (1990). *Laser Ultrasonics: Techniques and Applications*. Bristol: Adam Hilger.

Sharma, V.M.J., Kumar, K.S., Rao, B.N., Pathak, S.D. (2009). Effect of microstructure and strength on the fracture behavior of AA2219 alloy, *Materials Science and Engineering A*, 502, 45-53.

Stanchits, S.A., Lockner, D.A., Ponomarev, A.V. (2003). Anisotropic changes in p-wave velocity and attenuation during deformation and fluid infiltration of granite, *Bulletin of the Seismological Society of America*, 93(4), 1803-1822.

Tam, A.C. & Leung, W.P., (1984). Measurement of small elastic anisotropy in solids using laser-induced ultrasonic pulses, *Applied Physics Letters*, 45(10), 1040-1042.

Tanaka, T. & Izawa, Y. (2002). Detection method of fatigue damage in carbon steel using laser ultrasonics, *Journal of Nuclear Science and Technology*, 39(5), 514-519.

Thompson, R.B., Smith, J.F., Lee, S.S., Johnson, G.C. (1989). A Comparison of Ultrasonic and X-Ray Determinations of Texture in Thin Cu and Al Plates," *Metallurgical Transactions A*, 20A, 2431-2447.

Truell, R., Elbaum, C., Chick, B.B. (1969). *Ultrasonic Methods in Solid State Physics.* New York, New York: Academic Press, Inc.

Wang, J.J., Xu, B.Q., Shen, Z.H., Ni, X.W., Lu, J. (2008). Numerical simulation of thermoelastic stress field and laser ultrasound in transversely isotropic plate, *The Japan Society of Applied Physics*, 47(2), 956-963.

Wang, Q.Y., Kawagoishi, N., Chen, Q. (2006). Fatigue and fracture behaviour of structural Al-alloys up to very long life regimes, *International Journal of Fatigue*, 28, 1572-1576.

Waterman, P.C. (1959). Orientation dependence of elastic waves in single crystals, *Physical Review*, 113(5), 1240-1253.

Wormley, S., Thompson, R.B., Alers, G.A., Alers, R., Warchol, M. (2002). The influence of microstructure on the acoustoelastic measurement of stress in aluminum alloys, *Review of Quantitative Nondestructive Evaluation*, 21, 1688-1695.

Yamagishi, H., Fukuhara, M., Chiba, A. (2009). Acoustic effects on cyclic-tension fatigue of Al-4Cu-1Mg alloy by ultrasonic shear wave methods, *Metallurgical and Materials Transactions A*, 40A, 486-493.

Zadler, B.J. & Scales, J.A. (2008). Monitoring crack-induced change in elasticity with resonant spectroscopy, *Journal of Applied Physics*, 104(023536), 1-4.

Zhang, Ch. & Achenbach, J.D. (1988). Scattering by multiple crack configurations, *Transactions of the American Society of Mechanical Engineers*, 55, 104-110.

Zheng, Z. (2000). Seismic anisotropy due to stress-induced cracks, *International journal of Rock Mechanics and Mining Sciences*, 37, 39-49.

Zimmermann, M., (2012). Diversity of damage evolution during cyclic loading at very high numbers of cycles, *International Materials Review*, 57(2), 73-91.

# APPENDICES

## Appendix A: Derivation of the Orientation Distribution Coefficients (Theory)

We refer to derivations of the ODCs by Roe (1965) and Bunge (1982). For most of the work shown in this appendix, Roe's notation will be used.

*Roe*

Orientation distribution function:

$$w(\xi,\psi,\phi) = \sum_{l=0}^{\infty}\sum_{m=-l}^{l}\sum_{n=-l}^{l} W_{lmn} Z_{lmn}(\xi) e^{-im\psi} e^{-in\phi}. \tag{A-1}$$

Where $Z_{lmn}(\xi)$ is the generalization of the associated Legendre function (canonical solutions of the general Legendre equation) and $W_{lmn}$ is the orientation distribution coefficient.

*Bunge*

Orientation distribution function:

$$f(\phi_1,\Phi,\phi_2) = \sum_{l=0}^{\infty}\sum_{m=-l}^{l}\sum_{n=-l}^{l} C_l^{mn} e^{im\phi_2} P_l^{mn}(\Phi) e^{in\phi_1} \tag{A-2}$$

Where $P_l^{mn}(\Phi)$ is the generalization of the associated Legendre function and $C_l^{mn}$ is the distribution coefficient.

To begin the calculation for the probability of finding a crystallite at some orientation, we will represent sample and crystallite locations as most authors have by using the representation angles chosen by Roe (1965) in Figure 62. The sample axes o-xyz are axes fixed in a polycrystalline sample, while the axes O-XYZ are the axes fixed in one crystallite. To generate the crystallite's axis, we will first rotate about the z axis of the sample. Next, rotate about the x axis of the newly generated system. And finally, rotate about the z axis of this third generation coordinate system to yield the crystallite's system O-XYZ. To fix the two systems relative to one another, we will define the angle zOZ to be the polar angle θ, and the angle between plane zox and plane zOZ to be the azimuthal angle ψ. To finally fix the coordinate systems, we will define the y axis by defining the angle between the zoZ plane and the XOZ plane as φ.

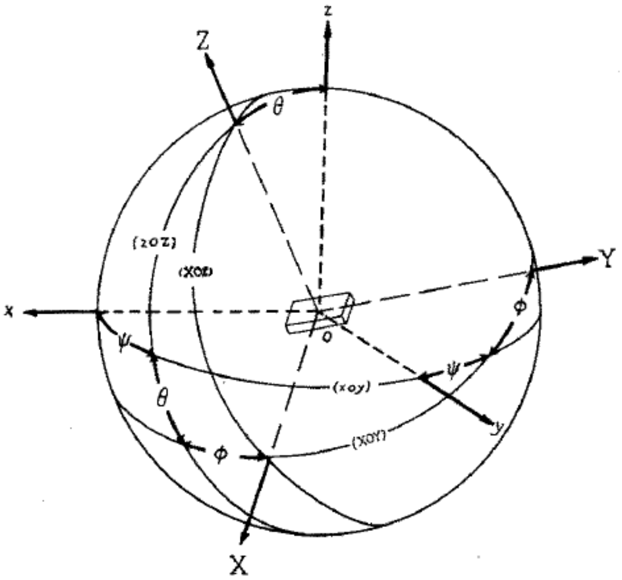

**Figure 62**: Eulerian angles representing orientation of crystallite coordinate system 0-XYZ with respect to sample coordinate system 0-xyz

If the z-axis of the sample and Z-axis of the crystallite are parallel, then this shows that ξ will go to one, while ψ no longer exists and forces ϕ to also go to zero because of its dependency to ψ. If all crystallites are not aligned with the z-axis of the sample, we can now define the orientation of all crystallites in the sample with

$$\int_{0}^{2\pi}\int_{0}^{2\pi}\int_{-1}^{1} w(\xi,\psi,\phi)\,d\xi\, d\psi\, d\phi = 1 \qquad \text{(A-3)}$$

where,

$$\xi = \cos\theta \tag{A-4}$$

We can expand $w(\xi,\psi,\varphi)$ into a series of spherical harmonics using the normalized associated Legendre polynomial $P_l^m$ if n = 0, or the generalization of the associated Legendre polynomial $Z_{lmn}(\xi)$. (Roe 1965)

$$w(\xi,\psi,\phi) = \sum_{l=0}^{\infty} \sum_{m=-l}^{l} \sum_{n=-l}^{l} W_{lmn} Z_{lmn}(\xi) e^{-im\psi} e^{-in\phi}. \tag{A-5}$$

The orientation distribution coefficients $W_{lmn}$ exhibit the qualities of Fourier amplitudes which can be seen when you solve for them: (Roe 1965)

$$W_{lmn} = \frac{1}{4\pi^2} \int_0^{2\pi} \int_0^{2\pi} \int_{-1}^{1} w(\xi,\psi,\phi) Z_{lmn}(\xi) e^{im\psi} e^{in\phi} d\xi d\psi d\phi. \tag{A-6}$$

The orientation distribution coefficients can now be used in the elastic stiffness calculation. The elastic constants of a polycrystalline sample can be found by transformation of the crystallite's reference frame, $C_{mnpq}$, to the sample's reference frame, $C_{ijkl}$, using the elastic constants from a single crystal (Li and Szpunar 1992; Nye 1972; Pursey and Cox 1954).

- For a cubic material, due to symmetry, the only elastic constants we will have are $c_{11}$, $c_{12}$, and $c_{44}$.
- For an orthorhombic material, we will have additional constants: $c_{11}, c_{22}, c_{33}, c_{44}, c_{55}, c_{66}, c_{12}, c_{13}, c_{23}$

$$C_{ijkl} = \sum_{m=1}^{3}\sum_{n=1}^{3}\sum_{p=1}^{3}\sum_{q=1}^{3} T_{ijklmnpq} C_{mnpq} \tag{A-7}$$

$$T_{ijklmnpq} = a_{im} a_{jn} a_{kp} a_{lq} \tag{A-8}$$

where, $T$ is the transformation matrix, and $a_{ij}$ are the direction cosines relating the sample's reference frame to the crystallite's reference frame. The direction cosines for the orientation system described above by Roe have been identified as follows:

$$a(\psi,\theta,\phi) = \begin{pmatrix} \cos\psi\cos\theta\cos\phi - \sin\psi\sin\phi & -\cos\psi\cos\theta\sin\phi - \sin\psi\cos\phi & \cos\psi\sin\theta \\ \sin\psi\cos\theta\cos\phi + \cos\psi\sin\phi & -\sin\psi\cos\theta\sin\phi + \cos\psi\cos\phi & \sin\psi\sin\theta \\ -\sin\theta\cos\phi & \sin\theta\sin\phi & \cos\theta \end{pmatrix} \tag{A-9}$$

These direction cosines are associated with the transformation matrix in the standard notations:

$$a(\psi,\theta,\phi) = \begin{pmatrix} a_{11} & a_{12} & a_{13} \\ a_{21} & a_{22} & a_{23} \\ a_{31} & a_{32} & a_{33} \end{pmatrix} = \begin{pmatrix} l_1 & l_2 & l_3 \\ m_1 & m_2 & m_3 \\ n_1 & n_2 & n_3 \end{pmatrix} \tag{A-10}$$

At this point, $T_{ijklmnpq}$ will only allow us to calculate the elastic constants for crystallites with a specific orientation. The ODF needs to be included in the transformation so that all crystallite orientations are accounted for. Taking an average of the transformation matrix over all possible orientations is required. (Li and Szpunar 1992)

$$\overline{T_{ijklmnpq}} = \int_0^{2\pi}\int_0^{2\pi}\int_0^{2\pi} T_{ijklmnpq} \times w(\xi,\psi,\phi)\,d\xi\,d\psi\,d\phi \tag{A-11}$$

Because we have solved the ODCs, the ODF solution can be inserted into the averaged transformation matrix so that our solution includes only constants.

$$\overline{T_{ijklmnpq}} = \int_0^{2\pi}\int_0^{2\pi}\int_0^{2\pi} T_{ijklmnpq} \times \sum_{l=0}^{\infty}\sum_{m=-l}^{l}\sum_{n=-l}^{l} W_{lmn} Z_{lmn}(\xi) e^{-im\psi} e^{-in\phi}\,d\xi\,d\psi\,d\phi \tag{A-12}$$

This average can be directly inserted into our elastic tensor transformation.

$$C_{ijkl} = \sum_{m=1}^{3}\sum_{n=1}^{3}\sum_{p=1}^{3}\sum_{q=1}^{3} \overline{T_{ijklmnpq}} C_{mnpq} \tag{A-13}$$

Now we can take the summation of the averaged transformation matrix and single crystal elastic constants to generate a solution for the material's elastic constant in that *ijkl.*

$$C_{ijkl} = \sum_{m=1}^{3}\sum_{n=1}^{3}\sum_{p=1}^{3}\sum_{q=1}^{3} \left( \int_0^{2\pi}\int_0^{2\pi}\int_0^{2\pi} T_{ijklmnpq} \times \sum_{l=0}^{\infty}\sum_{m=-l}^{l}\sum_{n=-l}^{l} W_{lmn} Z_{lmn}(\xi) e^{-im\psi} e^{-in\phi}\,d\xi\,d\psi\,d\phi \right) C_{mnpq} \tag{A-14}$$

In our case, we are only observing changes in the shear wave stiffness because our propagation and polarization for our longitudinal wave are parallel. $C_{66}$ is shown as an example to connect the method to the references where $i, j, k, l = 1,2,3$.

$$\rho p_i V^2 = c_{ijkl} p_l n_j n_k \tag{A-15}$$

Single crystal solution for $i = 1$:

$$\begin{aligned}\rho p_1 V^2 &= c_{1111} n_1^2 p_1 + c_{1212} n_2 n_1 p_2 + c_{1313} n_3 n_1 p_3 + c_{1221} n_2^2 p_1 + c_{1122} n_1 n_2 p_2 + c_{1331} n_3^2 p_1 + c_{1133} n_1 n_3 p_3 \\ &= (c_{11} n_1^2 + c_{44} n_2^2 + c_{44} n_3^2) p_1 + (c_{12} + c_{44}) n_1 n_3 p_3 + (c_{12} + c_{44}) n_1 n_2 p_2 \end{aligned} \tag{A-16}$$

Possible elastic constants for cubic and orthorhombic crystals:

$C_{1111}$, $C_{1212}$, $C_{1313}$, $C_{1221}$, $C_{1122}$, $C_{1331}$, $C_{1133}$, $C_{2211}$, $C_{2112}$, $C_{2121}$, $C_{2222}$,$C_{2323}$, $C_{2233}$, $C_{2332}$, $C_{3113}$, $C_{3223}$, $C_{3131}$, $C_{3232}$, $C_{3333}$, $C_{3311}$, $C_{3322}$

From Equation (A-16)

$$\begin{aligned}C_{1212} &= T_{12121111}C_{1111} + 2T_{12121122}C_{1122} + 4T_{12121212}C_{1212} + 4T_{12122323}C_{2323} + 4T_{12121313}C_{1313} \\ &\quad + 2T_{12121133}C_{1133} + T_{12122222}C_{2222} + 2T_{12122233}C_{2233} + T_{12123333}C_{3333}\end{aligned} \tag{A-17}$$

$$C_{66}^{s} = C_{44}^{c} + C[\tfrac{1}{5} + \tfrac{4}{35}\sqrt{2}\pi^2 (W_{400} - \sqrt{70}W_{440})] \tag{A-18}$$

where,

$$C = C_{11}^{c} - C_{12}^{c} - 2C_{44}^{c} \tag{A-19}$$

The orientation distribution coefficients are brought in by the ODF when we substituted the average transformation matrix for the transformation matrix in the elastic stiffness tensor calculation. In these equations $C^{s}$ refers to the sample's crystal system, and $C^{c}$ refers to the crystallite's system.

We can now insert this result into the velocity equation to solve for wave propagation in the $x_1$ or x direction and polarization in the $x_2$ or y direction.

$$\rho V_{xy}^{2} = C_{66}^{s} \tag{A-20}$$

These coefficients can also be solved by way of determinants.

## Appendix B: Transducer and interferometer operation

The work in this dissertation described results using contacting transducers or interferometers for the detection of ultrasound. This section will describe the properties of each detection method and explain their operation, giving reasons behind our decisions on when to use them in a given experiment. The conical transducer described in these experiments uses the stress-induced mechanical energy introduced by the laser to create the detected voltage and is based on a design originally fabricated at the National Institute of Standards and Technology (NIST) by Thomas Proctor (Figure 63b). This type of transducer uses a conical lead-zirconate-titanate active element with a silver electrode (grounded) attached to the truncated end of the active element cone with the back of the cone mounted to a larger brass cylinder (non-grounded). In order to detect ultrasonic waves, a gel couplant or other joining interface must bond the transducer to the material in question. The active areas on the original design and on the available commercial transducer both have a diameter of 1.5 mm that is meant to approximate a point source. The commercial transducer purchased from the Dunegan Engineering Company does have a ceramic wear plate surrounding the active element which increases the contact area to 20 mm.

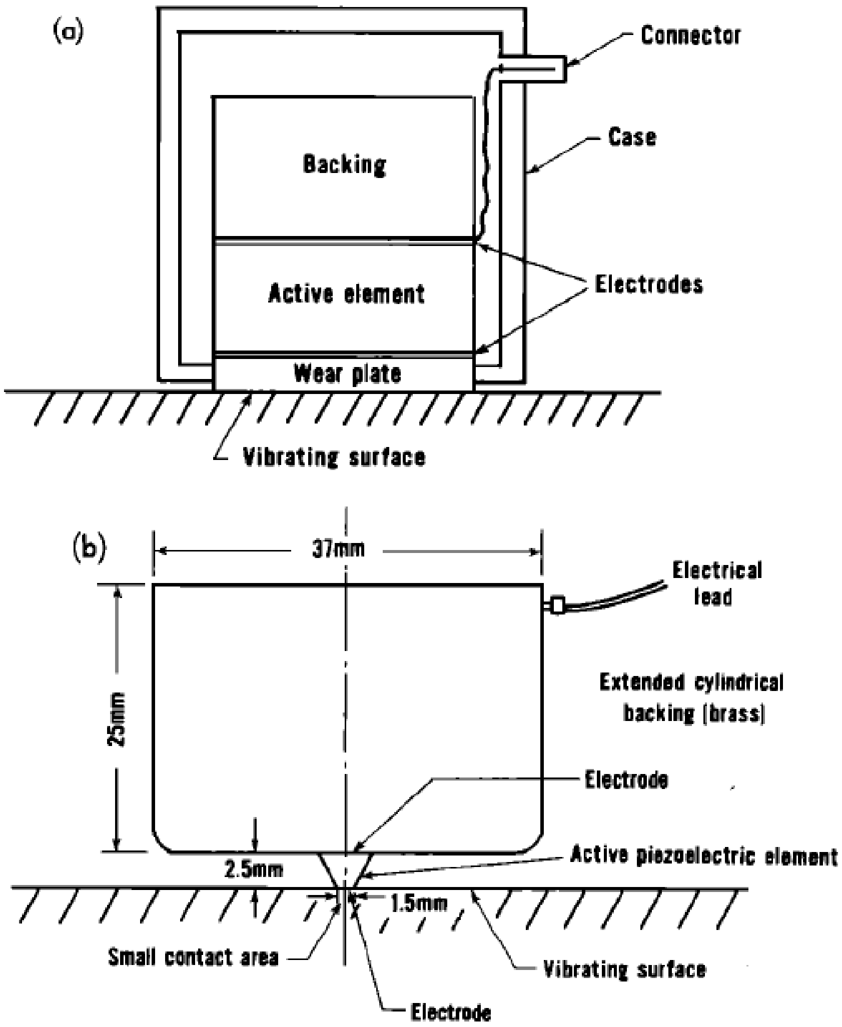

**Figure 63**: a. Conventional transducer b. Conical transducer (Proctor 1982)

Using a contacting transducer to detect ultrasonic waves is an inexpensive and easy-to-use method. There are many limitations, such as bonding to the sample surface, limited bandwidth, geometry and size of the transducer may be not be appropriate for some samples, delays in time-of-flight reading due to capacitance mismatch of sample material and transducer, and the inability to use it remotely and in extreme environments. The interferometer, however, eliminates all of these potential problems allowing the user more flexibility for testing conditions. The interferometer used in this thesis is closely related to the Michelson interferometer. A continuous wave laser is divided by a beam splitter with one path going to a reference mirror M1 and the other path going to the mirrored surface M2 whose measured displacement is of interest. The two beams are reflected from these mirrors and sent back through the beam splitter where they are re-combined and passed into a photodetector. When the two beams remain out-of-phase with one another there is destructive interference and no change in displacement is observed. When there is a slight disruption in the path of the beam directed at M2, the phase will shift and give constructive interference so that a displacement is recorded as a sinusoidal wave. There are several variations to the optical arrangement including the use of quarter waveplates which will change the polarization of the laser light so that collected light is maximized or so there is a guarantee of preventing feedback into the laser. These will require polarizing beam splitters. If beam reflection back into the laser cavity is not a concern, non-polarizing optics can be used. The interferometer configuration (Figure 21) uses a non-polarizing beam-splitting cube (NPBSC) to split a 532nm laser 50/50 going to a piezo-stabilized reference mirror and a sample polished to a mirror finish. The reflected beams return to the NPBSC and divide again into two photodetectors where the signals are combined in an amplifier and displayed on the oscilloscope. Ultrasonic data can be displayed in terms of displacement rather than signal voltage using the ultrasonic amplitudes recorded on the oscilloscope. Displacement is calculated in equation B-1using the distance between fringes that are dependent on the wavelength of the receiving laser and the ratio of data point voltage, $A_d$, to the average peak-to-peak signal voltage $A_o$ (McKie 1991; Garoi 2010).

$$u = 1/2\pi * 532e\text{-}9 * (A_d/A_o) \tag{B-1}$$

Laser interferometers do have their own drawbacks depending on the configuration of optics. The user could be limited by surface reflectivity and ease of operating the system. If possible, however, the interferometer will give a consistent, minimal uncertainty measurement for a material's elastic stiffness.

## Appendix C: Matlab and Mathematica codes

**C.1** The following Matlab code is for modeling a point source

Runmodel.m

```
thickness = 6.350               % thickness of sample in millimeters


t = (.001:1:4002).';
t2 = (.001:1:4001).';



   rl = 1/.0062;                % reciprocal of the longitudinal wavespeed mm/ns
   rs = 1/.0031;                % reciprocal of the shear wavespeed mm/ns
   tstepl = t > rl*thickness;
   tsteps = t > rs*thickness;
   zl = tstepl.*(sqrt(((t.*t)./(thickness*thickness))-(rl*rl)));
   zs = tsteps.*(sqrt(((t.*t)./(thickness^2))-(rs^2)));
   al = sqrt(rl.^(2) + zl.^(2));
   as = sqrt(rl.^(2) + zs.^(2));
   bl = sqrt(rs.^(2) + zl.^(2));
   bs = sqrt(rs.^(2) + zs.^(2));
   gl = (rs.^(2) + (2*zl.^(2)));
   gs = (rs.^(2) + (2*zs.^(2)));
   pl = 1./((gl.^2)-(4*(zl.^2).*al.*bl));
   ps = 1./((gs.^2) -(4*(zs.^2).*as.*bs));
   Fl = -(((zl.^2).*(al.^2).*bl.*gl.*(pl.^2)));
   Fs = (((zs.^2).*as.*(bs.^2).*gs.*(ps.^2)));
   derivFl = diff(Fl);
   derivFs = diff(Fs);
   vmodel = (derivFl + derivFs);

   plot(t2,vmodel)
```

**C.2** The following Matlab code is used plot the longitudinal and shear waves in a transversely isotropic medium:

Extrudedlinemodel.m

```
m33=5.7;                    %transverse isotropic: Stiffnesses forces longitudinal wave
                            earlier
m44=2.9;
m11=5.4;
m23=-(2*m44-m11);
m10=2.7;                    % Density

m1=m33/m44;                 %alpha
m2=m11/m44;                 %beta
m3=1.+m23/m44;              %kappa
m4=1+m1*m2-m3^2;            %xi Parameters in Calcs

c0= (.001:1:10002).';
c1=c0.*(m44/m10)^0.5;       %Time and Tau

c2=c1./4000.;               %Gamma3 = Tau/X3

c20=(m4*c2.^2-(1+m2)).^2-4*m2*(m1*c2.^4-(1.+m1)*c2.^2+1.);
                            %intermediate term
```

**Longitudinal Wave**

```
l1=((m4*c2.^2-(1.+m2)+sqrt(c20))/(2.*m2));
                            %Gamma2 +
c5=(2*(1+m1)*c2+2*m4*l1.*c2-4*m1*c2.^3)./(1+m2-m4*c2.^2+2*m2*l1);
                            %dGamma2/dgamma3 +
c17=sqrt(abs((1+m1+m4*l1).^2-4*m1*(m2*l1.^2+(1+m2)*l1+1)));
                            %phi with Gamma2 +

c25=sqrt(abs((1+m1+m4*l1+c17)./(2*m1)));
                            %gamma 3 1 with gamma 2 +
c26=sqrt(abs((1+m1+m4*l1-c17)./(2*m1)));
                            %gamma 3 3 with gamma 2 +

c7=(2*(1-m3)*l1.*(1+l1)-(m4*l1+m1).*(1+l1)-m1*c25.*c26);
                            %Rayleigh D +
c9=l1.*((1-m3).*(1+l1)-m1*c25.^2).*c26./(c25-c26)./c7;
                            %Long. Coeff. B2
c11=-c9.*c5./sqrt(l1);

for l1=0;
```

```
if c11>1000;

else
   l1=c11;
end
end
```

**Shear Wave**

```
s1=((m4*c2.^2-(1.+m2)-sqrt(c20))./(2.*m2));
                                %Gamma2 -
c6=(2*(1+m1)*c2+2*m4*s1.*c2-4*m1*c2.^3)./(1+m2-m4*c2.^2+2*m2*s1);
                                %dGamma2/dgamma3 -
c18=sqrt(abs((1+m1+m4*s1).^2-4*m1*(m2*s1.^2+(1+m2)*s1+1)));
                                %phi with gamma2 -

c15=sqrt(abs((1+m1+m4*s1+c18)./(2*m1)));
                                 % gamma 3 1 with gamma 2 -
c16=sqrt(abs((1+m1+m4*s1-c18)./(2*m1)));
                                %gamma 3 3 with gamma 2 -

c8=(2*(1-m3)*s1.*(1+s1)-(m4*s1+m1).*(1+s1)-m1*c15.*c16);
                                %Rayleigh D -
c10=s1.*((1-m3)*(1+s1)-m1*c16.^2).*c15./(c15-c16)./c8;
                                %Shear Coeff. B1
c12=c10.*c6./sqrt(s1);
for s1=0;
if c12>1000;
else s1=c12;
end
end

transverse = l1+s1;             %plot longitudinal and shear wave

m33=5.4;                        %Isotropic graphite: Stiffnesses
m44=2.5;
m11=5.4;
m23=-(2*m44-m11);
m10=2.7;                        % Density

m1=m33/m44;                     %alpha
m2=m11/m44;                     %beta
m3=1.+m23/m44;                  %kappa
m4=1+m1*m2-m3^2;                %xi Parameters in Calcs

c0= (.001:1:10002).';
c1=c0.*(m44/m10)^0.5;           %Time and Tau
```

```
c2=c1./4000.;                     %Gamma3 = Tau/X3

c20=(m4*c2.^2-(1+m2)).^2-4*m2*(m1*c2.^4-(1.+m1)*c2.^2+1.);
                                  %intermediate term
```

**Longitudinal Wave**

```
l2=((m4*c2.^2-(1.+m2)+sqrt(c20))/(2.*m2));
                                  %Gamma2 +
c5=(2*(1+m1)*c2+2*m4*l2.*c2-4*m1*c2.^3)./(1+m2-m4*c2.^2+2*m2*l2);
                                  %dGamma2/dgamma3 +
c17=sqrt(abs((1+m1+m4*l2).^2-4*m1*(m2*l2.^2+(1+m2)*l2+1)));
                                  %phi with Gamma2 +

c25=sqrt(abs((1+m1+m4*l2+c17)./(2*m1)));
                                  %gamma 3 1 with gamma 2 +
c26=sqrt(abs((1+m1+m4*l2-c17)./(2*m1)));
                                  %gamma 3 3 with gamma 2 +

c7=(2*(1-m3)*l2.*(1+l2)-(m4*l2+m1).*(1+l2)-m1*c25.*c26);
                                  %Rayleigh D +
c9=l2.*((1-m3).*(1+l2)-m1*c25.^2).*c26./(c25-c26)./c7;
                                  %Long. Coeff. B2
c11=-c9.*c5./sqrt(l2);

for l2=0;
if c11>1000;

else
  l2=c11;
end
end
```

**Shear Wave**

```
s2=((m4*c2.^2-(1.+m2)-sqrt(c20))./(2.*m2));
                                  %Gamma2 -
c6=(2*(1+m1)*c2+2*m4*s2.*c2-4*m1*c2.^3)./(1+m2-m4*c2.^2+2*m2*s2);
                                  %dGamma2/dgamma3 -
c18=sqrt(abs((1+m1+m4*s2).^2-4*m1*(m2*s2.^2+(1+m2)*s2+1)));
                                  %phi with gamma2 -

c15=sqrt(abs((1+m1+m4*s2+c18)./(2*m1)));
                                  % gamma 3 1 with gamma 2 -
c16=sqrt(abs((1+m1+m4*s2-c18)./(2*m1)));
                                  %gamma 3 3 with gamma 2 -
```

```
c8=(2*(1-m3)*s2.*(1+s2)-(m4*s2+m1).*(1+s2)-m1*c15.*c16);
                              %Rayleigh D -
c10=s2.*((1-m3)*(1+s2)-m1*c16.^2).*c15./(c15-c16)./c8;
                              %Shear Coeff. B1
c12=c10.*c6./sqrt(s2);
for s2=0;
if c12>1000;
else s2=c12;
end
end

isotropic=l2+s2;

m33=5.7;                      %perpendicular to line: Stiffnesses
m44=2.9;
m11=5.4;
m23=-(2*m44-m11);
m10=2.7;                      % Density

m1=m11/m44;                   %alpha
m2=m33/m44;                   %beta
m3=1.+m23/m44;                %kappa
m4=1+m1*m2-m3^2;              %xi Parameters in Calcs

c0= (.001:1:10002).';
c1=c0.*(m44/m10)^0.5;         %Time and Tau

c2=c1./4000.;                 %Gamma3 = Tau/X3

c20=(m4*c2.^2-(1+m2)).^2-4*m2*(m1*c2.^4-(1.+m1)*c2.^2+1.);
                              %intermediate term
```

**Longitudinal Wave**

```
l3=((m4*c2.^2-(1.+m2)+sqrt(c20))/(2.*m2));
                              %Gamma2 +
c5=(2*(1+m1)*c2+2*m4*l3.*c2-4*m1*c2.^3)./(1+m2-m4*c2.^2+2*m2*l3);
                              %dGamma2/dgamma3 +
c17=sqrt(abs((1+m1+m4*l3).^2-4*m1*(m2*l3.^2+(1+m2)*l3+1)));
                              %phi with Gamma2 +

c25=sqrt(abs((1+m1+m4*l3+c17)./(2*m1)));
                              %gamma 3 1 with gamma 2 +
c26=sqrt(abs((1+m1+m4*l3-c17)./(2*m1)));
                              %gamma 3 3 with gamma 2 +

c7=(2*(1-m3)*l3.*(1+l3)-(m4*l3+m1).*(1+l3)-m1*c25.*c26);
```

```
                          %Rayleigh D +
c9=l3.*((1-m3).*(1+l3)-m1*c25.^2).*c26./(c25-c26)./c7;
                          %Long. Coeff. B2
c11=-c9.*c5./sqrt(l3);

for l3=0;
if c11>1000;

else
   l3=c11;
end
end
```

**Shear Wave**

```
s3=((m4*c2.^2-(1.+m2)-sqrt(c20))./(2.*m2));
                          %Gamma2 -
c6=(2*(1+m1)*c2+2*m4*s3.*c2-4*m1*c2.^3)./(1+m2-m4*c2.^2+2*m2*s3);
                          %dGamma2/dgamma3 -
c18=sqrt(abs((1+m1+m4*s3).^2-4*m1*(m2*s3.^2+(1+m2)*s3+1)));
                          %phi with gamma2 -

c15=sqrt(abs((1+m1+m4*s3+c18)./(2*m1)));
                          % gamma 3 1 with gamma 2 -
c16=sqrt(abs((1+m1+m4*s3-c18)./(2*m1)));
                          %gamma 3 3 with gamma 2 -

c8=(2*(1-m3)*s3.*(1+s3)-(m4*s3+m1).*(1+s3)-m1*c15.*c16);
                          %Rayleigh D -
c10=s3.*((1-m3)*(1+s3)-m1*c16.^2).*c15./(c15-c16)./c8;
                          %Shear Coeff. B1
c12=c10.*c6./sqrt(s3);
for s3=0;
if c12>1000;
else s3=c12;
end
end

perpendicular=l3+s3;      %plot longitudinal and shear wave

plot(c0,transverse,c0,isotropic,c0,perpendicular)
```

**C-3** Mathematica code to determine the stiffness matrix from EBSD, originally created by Pedro Peralta, Arizona State University

```
Rot={{0,1,0},{−1,0,0},{0,0,1}};

r1[p1_,f_,p2_]={Cos[p1] Cos[p2]-Cos[f] Sin[p1] Sin[p2],
  Cos[p2] Sin[p1]+Cos[f] Cos[p1] Sin[p2] , Sin[f] Sin[p2]};

r2[p1_,f_,p2_]={-Cos[f] Cos[p2] Sin[p1]-Cos[p1] Sin[p2],
  Cos[f] Cos[p1] Cos[p2]-Sin[p1] Sin[p2] , Cos[p2]Sin[f]};

r3[p1_,f_,p2_]={Sin[p1]Sin[f],-Cos[p1]Sin[f] , Cos[f]};

g[p1_,f_,p2_]=Rot.Transpose[{r1[p1,f,p2],r2[p1,f,p2],r3[p1,f,p2]}];
```

Note: the argument for the matrix g are the three Euler angles in radians in the Bunge convention. The rows of g as defined above should be the unit vectors describing the crystallographic axes parallel to the external XYZ axes (X to the right, Y going up and Z coming out of the page).

```
FileNames[]

Pos={rotated};

Print[datafile.txt]

data1=Import["datafile.txt", "Table"];
n=Length[data1];
data=Take[data1,13-n];
Cms=Table[0,{k,n-13}, {i,6}, {j,6}];
C11:=1.47*10^11;
C44:=0.72*10^11;
C12:=1.11*10^11;
Ca=Table[0,{i,3},{j,3},{k,3},{l,3}];
Cn1=Ca;
Ca[[1,1,1,1]]=C11;
Ca[[2,2,2,2]]=C11;
Ca[[3,3,3,3]]=C11;
Ca[[1,1,2,2]]=C12;
Ca[[1,1,3,3]]=C12;
Ca[[2,2,3,3]]=C12;
Ca[[3,3,2,2]]=C12;
Ca[[1,2,1,2]]=C44;
Ca[[1,3,1,3]]=C44;
Ca[[2,3,2,3]]=C44;
Ca[[3,2,3,2]]=C44;
```

```
Do[Ca[[i,i,1,1]]=Ca[[1,1,i,i]],{i,2,3}];
Do[Ca[[i,1,i,1]]=Ca[[1,i,1,i]],{i,2,3}];
Do[Do[Ca[[j,i,i,j]]=Ca[[j,i,j,i]],{i,1,3}],{j,1,3}];

Do[R1=g[data[[i,5]],data[[i,6]],data[[i,7]]];Cn1=N[Table[Sum[Sum[Sum[Sum[R1[[i,a]]*
R1[[j,b]]*R1[[k,c]]*R1[[l,d]]*Ca[[a,b,c,d]],{d,1,3}],{c,1,3}],{b,1,3}],{a,1,3}],{i,3},{j,3}
,{k,3},{l,3}]];

Cms[[i]]={{Cn1[[1,1,1,1]],Cn1[[1,1,2,2]], Cn1[[1,1,3,3]], Cn1[[1,1,2,3]], Cn1[[1,1,1,3]],
Cn1[[1,1,1,2]]},{Cn1[[1,1,2,2]], Cn1[[2,2,2,2]], Cn1[[2,2,3,3]], Cn1[[2,2,2,3]],
Cn1[[2,2,1,3]], Cn1[[2,2,1,2]]},{Cn1[[1,1,3,3]], Cn1[[2,2,3,3]], Cn1[[3,3,3,3]],
Cn1[[3,3,2,3]],Cn1[[3,3,1,3]],Cn1[[3,3,1,2]]},{Cn1[[1,1,2,3]],Cn1[[2,2,2,3]],Cn1[[3,3,2,
3]],Cn1[[2,3,2,3]],Cn1[[1,3,2,3]],Cn1[[1,2,2,3]]},{Cn1[[1,1,1,3]],Cn1[[2,2,1,3]],Cn1[[3,3
,1,3]],Cn1[[2,3,1,3]],Cn1[[1,3,1,3]],Cn1[[1,2,1,3]]},{Cn1[[1,1,2,1]],Cn1[[2,2,2,1]],Cn1[[
3,3,2,1]],Cn1[[2,3,2,1]],Cn1[[1,3,2,1]],Cn1[[1,2,2,1]]}};, {i,n-13}];

Area=Sum[data[[i,15]], {i,n-13}];
Cmu=Sum[Cms[[i]]*(data[[i,15]])/Area, {i,n-13}];
Cml=Inverse[Sum[Inverse[Cms[[i]]]*(data[[i,15]])/Area, {i,n-13}]];
Cmh=(Cmu+Cml)/2;

datafile.txt>>>LTplane5.txt;

Do[Cmu[[i, j]]>>> LTplane5.txt, {i,6}, {j,6}];
                                %Upper limit
Do[Cml[[i, j]]>>> LTplane5.txt, {i,6}, {j,6}];
                                %Lower limit
Do[Cmh[[i, j]]>>> LTplane5.txt, {i,6}, {j,6}];
                                %Hill's Average
data1=Import["old top left rotated.txt","Table"]
Cmu
Cml
Cmh
```

# REFERENCES

Bunge, H.J. (1982). *Texture Analysis in Materials Science*. London: Butterworth & Co.

Garoi, F., Apostol, D., Damian, V., Schiopu, P. (2010). Traceable vibration amplitude measurement with a laser interferometer. *Romanian Journal of Physics*, 55(3-4), 369-375.

Li, D.Y. & Szpunar, J.A. (1992). Determination of single crystal elastic constants from the measurement of ultrasonic velocity in the polycrystalline material, *Acta Metallurgica et Materialia.* 40(12), 3277-3283.

McKie, A.D.W., Wagner, J.W., Spicer, J.B., Deaton, J.B. (1991). Dual-beam interferometer for the accurate determination of surface-wave velocity, *Applied Optics*, 30(28), 4034-4039.

Nye, J.F. (1972) *Physical Properties of Crystals*. London: Oxford University Press.

Proctor, T.M. (1982). An improved piezoelectric acoustic emission transducer, *Journal of the Acoustical Society of America*, 71(5), 1163-1168.

Pursey, H. & Cox, H.L. (1954). The correction of elasticity measurements on slightly anisotropic materials, *Philosophical Magazine*, 45(362), 295-305.

Roe, J.R. (1965). Description of crystallite orientation in polycrystalline materials. III. General solution to pole figure inversion, *Journal of Applied Physics*, 36(6), 2024-2031.

# CURRICULUM VITAE

Lindsey R. Lindamood (Channels)
206 Maryland Hall
3400 N. Charles St.
Baltimore, Maryland 21218
LRLindamood@gmail.com

*Education*
Johns Hopkins University, Baltimore, Maryland
Ph.D. Materials Science and Engineering, October 2013
Advisor: Professor Jim Spicer
Dissertation: Determining texture in materials using laser ultrasonic methods

Bowling Green State University, Bowling Green, Ohio
B.S. Physics with minor in Astronomy, December 2005

*Professional Experience*
Johns Hopkins University – Baltimore, MD, August 2006-October 2013
Graduate research assistant – Department of Materials Science and Engineering

> Measured shear birefringence in materials using a laser ultrasonics and determined texture in metal alloys using a laser line source technique. Monitored fatigue damage in aluminum alloys with laser ultrasound by recording apparent events of shear wave birefringence.

National High Magnetic Field Laboratory – Florida State University, Tallahassee, FL, Summer 2005
Research Experience for Undergraduates (REU) Intern

> Studied the mechanical, electrical, and physical properties of Spanish moss to evaluate it as a potential candidate for solar-cell use. Study published in a peer-reviewed journal.

*Professional Service and Outreach*
Mentor – Women in Science and Engineering (WISE) – JHU and Garrison Forest School, Spring 2012

> Encouraged high school students to explore future interests in science and engineering fields. Mentored a high school student on an independent project testing the mechanical properties of field hockey sticks using several testing methods, including high-speed photography, laser ultrasonics, acoustic emission, mechanical testing, and metallography.

Private Tutor K–12, 2006-2011
National Federation of the Blind Youth Slam – Summer camp course instructor, 2007, 2009

*Publications and Conference Proceedings*

Lindamood, L., Spicer, J., (2012) A Laser-Based Method for Ultrasonic Characterization of Nuclear Grade Graphites. *Transactions of the American Nuclear Society*, 106, 100-102.

Lindamood, L., Spicer, J., (2011) Ultrasonic birefringence measurements of elastic anisotropy in fatigue damaged brass, copper and aluminum alloys. *NDE for Safety/Defektoskopie*, 79-86.

Channels, L., Chakraborty, D., Butrym, B., Kovvali, N., Spicer, J., Papandreou-Suppappola, A., Afshari, M., Inman, D., Chattopadhyay, A., (2009) A comparative study of fatigue damage sensing in aluminum alloys using electrical impedance and laser ultrasonic methods. *Proceedings of SPIE - The International Society for Optical Engineering*, 7295.

Channels, L., Chakraborty, D., Simon, D., Kovvali, N., Spicer, J., Papandreou-Suppappola, A., Cochran, D., Peralta, P., Chattopadhyay, A., (2008) Ultrasonic sensing and time-frequency analysis for detecting plastic deformation in an aluminum plate, *Proceedings of SPIE - The International Society for Optical Engineering*, 6926.

Channels, L., Tokumoto, T., Jobiliong, E., Brooks, J., Nellutla, S., Dalal, N., (2006) Dielectric, electron paramagnetic resonance and transport properties of Spanish moss, *Journal of Low Temperature Physics*, 142(3-4), 663-668.